

Abstract

HAVERKAMP, JASON DIRK. Plasma Physics in Pulsed Laser Deposition of Hydrogen-free Diamond-like Carbon Films and Nanocomposites. (Under the direction of Dr. J. Narayan and Dr. M.A. Bourham)

This dissertation focuses on the analysis of the plasma plume created in pulsed laser ablation thin film deposition of diamond-like carbon and the correlation of the characteristics of the plume to thin film properties. Diamond-like carbon films were deposited on silicon substrates by pulsed laser deposition at different laser energy densities. Important plasma parameters, such as ion kinetic energy, ion density, and electron temperature are altered by changing the laser energy density. These plasma properties determine the coordination states of carbon atoms within the deposited film. The diamond-like and graphite-like coordination states of carbon, termed sp^3 and sp^2 , respectively, determine film properties such as hardness, optical properties, and electronic properties.

The sp^3 fraction of the diamond-like carbon was directly determined through electron energy loss spectroscopy. The microstructure of the sp^2 coordinated carbon was determined with visible Raman spectroscopy. Plasma properties were analyzed by quadrupole Langmuir probes and mass loss measurements. Langmuir probe measurements indicate that ion density, ion flow speed, and electron temperature increase with laser energy density. Mass loss measurements show that the plume has an ionization fraction between 5 and 10 percent. Therefore, neutral particles have a significant role in film growth. Current models for the growth of diamond-like carbon films are reviewed. A deposition model based on electronic excitation is proposed. The probability of surpassing the energy barrier between sp^2 and sp^3 coordination is increased via an effective reduction of the activation barrier due to electronic excitation. The energy for electronic excitation is supplied by electron and photon interactions with ions and neutrals in the plume, as well as recombination of ions at the surface.

To investigate the effect of magnetic fields on plasma properties and film growth, a strong magnetic field was placed perpendicular to the direction of plasma flow. Plasma flow speed, electron temperature, and ion density were studied with quadrupole Langmuir probes. Magnetic probes investigated the interaction between the flowing plasma and the external magnetic field. A correction for the influence of the magnetic field on the collection of electrons by the quadrupole Langmuir probe was derived. Plasma flow speed was reduced due to interaction with the magnetic field. The kinetic β was $\approx 1 \times 10^{-4}$, indicating that magnetic field energy density is significantly greater than the flow energy density. Magnetic probe data shows a field deflection of ≈ 10 Gauss, consistent with small kinetic β . Field line diffusion occurs on a faster time scale than predicted by electron-ion resistivity. The contribution of neutrals to the resistivity is necessary to explain the observed field diffusion rate. Electron temperature increased by a factor of 3 to 4 over the unmagnetized electron temperatures. Electron heating by field line diffusion is eliminated due to the weak field line deflection. Plume slowing is a mechanism by which the electron temperature may increase. This process requires an anomalously high electron-ion collision frequency. Ion density results show an instability at the ion

cyclotron frequency and higher frequency noise. A classical Rayleigh-Taylor instability can be eliminated due to unfavorable field geometry and slow growth time. The observed instability satisfies a transverse ion-cyclotron instability. Noise at higher frequencies may be a result of the Kelvin-Helmholtz instability.

A diamond-like carbon film was deposited in the presence of the external magnetic field. Its sp^3 fraction was analyzed with electron energy loss spectroscopy. The sp^3 fraction was less than the sp^3 fraction for a diamond-like carbon film deposited at the same laser energy. However, in the magnetized deposition case, the ions have a smaller flow speed than in the unmagnetized case. The observed sp^3 fraction in the deposition with the magnetic field is larger than expected for the ion kinetic energy. This is due to the presence of neutrals whose flow speeds are unaffected by the magnetic field. No evidence of significant plume deflection was observed.

Large compressive stresses within as-deposited diamond-like carbon films prevent the growth of thick films. Diamond-like carbon films were doped with carbide and non-carbide forming elements, titanium and copper, respectively, to reduce the internal stress. The films were analyzed with electron energy loss spectroscopy to determine the sp^3 fraction in the doped diamond-like carbon films. Visible Raman spectroscopy was used to quantify stress reduction. Nanohardness measurements were performed to investigate the change in hardness with dopant concentration. High resolution transmission electron microscopy and Z-contrast imaging were used to determine the ordering of the dopants within the diamond-like carbon.

High resolution transmission electron microscopy revealed the formation of nanocrystals of titanium and copper. Z-contrast imaging reveals that non-carbide forming elements form self assembled arrays of nanoparticles, whereas carbide forming elements form layers. At the dopant concentrations used, the dopants form nanocrystals, rather than occupying substitutional or interstitial sites within the diamond-like carbon film. Raman spectroscopy indicates that the addition of copper is more effective than titanium at reducing internal stresses. Hardness measurements indicate that the addition of dopants decreases the hardness of diamond-like carbon films. Electron energy loss spectroscopy showed an apparent reduction in sp^3 fraction with the addition of dopants. The use of electron energy loss spectroscopy to determine sp^3 fraction in doped diamond-like carbon may not be reliable.

Plasma Physics in Pulsed Laser Deposition of Hydrogen-free Diamond-like Carbon Films and Nanocomposites

by

Jason Dirk Haverkamp

A dissertation submitted to the Graduate Faculty of
North Carolina State University
in partial fulfillment of the
requirements for the Degree of
Doctor of Philosophy

Nuclear Engineering

Raleigh, North Carolina

May 7, 2004

Approved by:

Dr. Jagdish Narayan

Dr. Mohamed A. Bourham

Dr. John Gilligan

Dr. Gerd Duscher

Biography

Jason Dirk Haverkamp was born on July 24th, 1978 to Obbe and Daphne Haverkamp. He was born and raised in the city of Greensboro, North Carolina with his parents and younger sister, Sarah. Jason attended Guilford County Schools until his graduation from James B. Dudley Senior High School in 1996. In high school, Jason was a member of many academic, service, and honorary societies, and played varsity soccer and tennis. It was an interest in the sciences and math, that drew his interests to nuclear engineering. Jason enrolled in North Carolina State University in August 1996 and received his bachelor's degree in May 2000. He received his Master's degree in Nuclear Engineering under Dr. R.M. Mayo and Dr. J. Narayan in June of 2001. After completing his Master's degree, he continued his education as a doctoral student under Dr. J. Narayan and Dr. M.A. Bourham in Nuclear Engineering.

Acknowledgments

I would like to acknowledge the help and support of many people. First, I would like to thank my parents, Obbe and Daphne Haverkamp, and family for their support, encouragement and patience throughout my college career. Drs. Narayan, Bourham, Gilligan and Duscher deserve much credit for their enthusiasm and scientific expertise. Dr. Ashutosh Tiwari and Dr. Chuming Jin provided assistance in the laser laboratory. Dr. Chuming Jin provided hardness measurements performed in Dr. Roger Narayan's laboratory at Georgia Tech. Dirk Scholvin of Georgia Tech provided some of the doped diamond-like carbon samples for analysis. Alex Kvit assisted with Z-contrast imaging and with general operation of the transmission electron microscope. I wish to thank my fellow nuclear engineering graduate students, Brian Bures and Travis Gray, for their experimental and theoretical insight, and encouragement. Fellow materials science graduate students Honghui Zhou and Amit Chugh provided much assistance in the materials science laboratories. I also wish to thank the machine shop in the materials science department for their assistance in the construction of the magnet assembly. Finally, I wish to thank Dr. Nemanich for use of his visible Raman spectroscopy equipment.

Contents

List of Figures	vii
List of Tables	x
1 Introduction	1
2 Experimental	7
2.1 Pulsed Laser Deposition	7
2.2 Magnetically Assisted Pulsed Laser Deposition	8
2.3 Electron Microscopy	10
2.4 Hardness Testing	14
2.5 Visible Raman Spectroscopy	15
2.6 Langmuir Probes	16
2.6.1 Unmagnetized Plasmas	17
2.6.2 Magnetized Plasmas	21
2.7 Magnetic Probes	22
2.8 Mass Loss Measurements	25
3 Laser Ablation Plume Plasma Physics	26
3.1 Review of Models of Plume Behavior	26
3.1.1 Formation	26
3.1.2 Expansion	32
3.2 Langmuir Probes	34
3.2.1 Forces	34
3.2.2 Finite Probe Size	35
3.2.3 Collisions	37

3.2.4	Estimation of T_i assuming time of flight	39
3.3	Energy Balance	42
3.3.1	Neutral Atom Densities	42
3.3.2	Energy Balance	45
3.4	Plume-Substrate Interaction	49
4	Growth of Diamond-like Carbon Films	52
4.1	Current Diamond-like Carbon Models	52
4.1.1	Cuomo's Model	52
4.1.2	Molecular Dynamics	53
4.1.3	Subplantation	53
4.2	Energy Barrier Deposition Model	54
4.3	Results of Diamond-like Carbon Deposition at Varying Plasma Conditions	61
4.3.1	Raman Spectroscopy	61
4.3.2	Electron Energy Loss Spectroscopy	64
4.3.3	Discussion in Terms of Energy Barrier Model	66
5	Magnetically Assisted Pulsed Laser Deposition	70
5.1	Corrections to Langmuir Probe in Magnetic Field	70
5.2	Dynamics of Laser Produced Plasma in Magnetic Field	76
5.2.1	Flow Speed Calculation	76
5.2.2	Magnetic Field Calculations	79
5.2.3	Electron Temperature	82
5.2.4	Ion Dynamics	86
5.3	Effect on Film Quality	92
6	Doped Diamond-like Carbon	94
6.1	HRTEM and Z Contrast	94
6.2	Raman Spectroscopy	96
6.3	Hardness Measurements	100
6.4	Electron Energy Loss Spectroscopy	101
6.4.1	Low Loss Region	101
6.4.2	Carbon K Edge	103
6.4.3	Copper and Titanium Ionization Edges	104
7	Conclusions	107

8 Future Work	110
8.1 Undoped Diamond-like Carbon Films	110
8.2 Doped Diamond-like Carbon Films	110
8.3 Optical Spectroscopy	111
8.4 Self Assembly of Nanostructured Magnetic Materials	111
8.5 Different Magnetic Field Studies	111
 Bibliography	 112

List of Figures

2.1	Experimental setup showing optical bench.	8
2.2	Pulsed laser deposition chamber. Note that the Langmuir probe is off the plume centerline. A convectron gauge and an ionization gauge are not shown.	9
2.3	Target and substrate holder for the pulsed laser deposition experiments.	10
2.4	Diagram of magnet and substrate holder.	11
2.5	Plot of magnetic field strength within the magnet and substrate holder.	12
2.6	Geometry of the target, magnet holder, and Langmuir/ \dot{B} probes. The target and magnet holder are not to scale. The positions of the magnets and the probe positions are to scale.	13
2.7	Schematic of the quadruple Langmuir probe.	17
2.8	Block diagram for Langmuir probe experiment.	18
2.9	Langmuir probe circuit.	19
2.10	Wake effects on probe tip 4 in the quadruple Langmuir probe.	20
2.11	Circuit model for \dot{B} probe.	22
2.12	True magnetic field and magnetic field as detected by the \dot{B} coil.	23
2.13	Correction factors for the \dot{B} probe as a function of frequency.	24
3.1	Results of a simple zero dimensional, time dependant code for the formation of the plasma plume.	31
3.2	Geometry of Langmuir probe for time-of-flight analysis.	35
3.3	Electron-ion mean free path as a function of electron density at different electron temperatures. These mean free paths are identical to the ion-ion mean free path under the assumption that electron and ion temperatures are identical.	40
3.4	Values of $\ln(I/E^{5/2})$ versus ion energy E for estimation of initial ion temperature via kinetic theory.	41
3.5	Mass loss and total particle inventory as a function of laser energy.	43
3.6	Neutral atom density and ionization fraction as a function of laser energy.	44
4.1	Free energy diagram describing the processes involved in formation of sp^3 coordination.	55

4.2	Raman spectra of $t - \alpha C$ films deposited at different laser energy densities. These different laser energy densities correspond to the kinetic energies of the Carbon ions within the plume.	62
4.3	G peak position versus sp^3 fraction. Data is from Ferrari and Robertson, Phys. Rev. B 61 (2000) p. 14095 and from current work. A non-linear fit used for estimation of sp^3 fraction is shown.	63
4.4	Low-loss spectra of $t - \alpha C$ films deposited at different laser energy densities. These different laser energy densities correspond to the kinetic energies of the carbon ions within the plume.	64
4.5	Plasmon energy and estimated film density as a function of laser energy density.	65
4.6	High-loss spectra of $t - \alpha C$ films deposited at different laser energy densities.	66
4.7	sp^3 fractions as a function of laser energy density as calculated by electron energy loss spectroscopy and by Raman spectroscopy.	67
5.1	Electron temperature at the 3 cm. Langmuir probe position, with and without magnetic field correction. Laser Energy 550 mJ. Lens position 12 cm.	75
5.2	Geometry of the target, magnet holder, and Langmuir/ \dot{B} probes. The target and magnet holder are not to scale. The positions of the magnets and the probe positions are to scale.	76
5.3	Normalized V_{12} data as a function of Langmuir probe position for different laser energies.	77
5.4	Langmuir probe position versus V_{12} signal arrival time for 350 mJ, 440 mJ, and 550 mJ.	78
5.5	Change in magnetic field at a laser energy of 350 mJ, 440 mJ, and 550 mJ at different positions. The first plot contains the change in the field without the external magnetic field present.	80
5.6	Change in magnetic field at a laser energy of 350 mJ, 440 mJ, and 550 mJ at different positions.	81
5.7	Electron temperatures corrected for the presence of a magnetic field as a function of time at 550, 440 and 350 mJ Lens position 12 cm.	83
5.8	Peak electron temperatures corrected for the presence of a magnetic field as a function of position. Laser energy 350 mJ. Lens position 12 cm.	84
5.9	Raw V_{i3} signal from Langmuir probe in magnetized plume. Langmuir probe position 3 cm. Laser Energy 550 mJ. Spot size $0.22cm^2$.	86
5.10	Ion densities at 1 cm and 2 cm at different laser energies. Spot size $0.22cm^2$.	87
5.11	Ion densities at 3 cm, 4 cm, and 5 cm at different laser energies. Spot size $0.22cm^2$.	88
5.12	EELS spectrum of DLC film deposited with magnetic field.	92
5.13	Effect of magnetic field on the sp^3 fraction of DLC films.	93
6.1	High resolution image of copper nanoparticles in diamond-like carbon.	95
6.2	High resolution image of titanium nanoparticles in diamond-like carbon.	96
6.3	High resolution image of silver nanoparticles in diamond-like carbon.	97
6.4	Visible Raman spectra of titanium and copper doped diamond-like carbon at different dopant concentrations.	98

6.5	Sample hardness measurement of 2.0 atom percent titanium doped diamond-like carbon. . .	100
6.6	Low loss region from EELS spectra of titanium and copper doped diamond-like carbon at different dopant concentrations.	102
6.7	Carbon K shell ionization region from EELS spectra of titanium doped diamond-like carbon at different titanium concentrations.	103
6.8	L shell ionization region from EELS spectra of copper and titanium doped diamond-like carbon at different titanium concentrations.	105

List of Tables

2.1	Important Langmuir probe geometry parameters.	21
3.1	Adiabatic expansion coefficients and estimated electron temperatures as a function of laser energy density.	34
3.2	Applicability of time-of-flight assumption at different Langmuir probe positions.	36
3.3	Electron-electron mean free path as a function of laser energy at the 1 <i>cm</i> Langmuir probe position.	38
3.4	Applicability of time-of-flight assumption at different Langmuir probe positions accounting for a finite plume thickness.	39
3.5	Kinetic energy partition of the energy balance.	46
3.6	Thermal energy partition of the energy balance.	47
3.7	Conducted energy partition of the energy balance.	47
3.8	Energy balance of the pulsed laser deposition plasma.	48
3.9	Sheath potentials at a substrate 4 <i>cm</i> from the target as a function of laser energy.	49
3.10	Sputtering yield and sputtered flux as a function of laser energy. Note that the density indicated is at 4 <i>cm</i> from the target.	51
4.1	Atomic range in diamond-like carbon for the ion kinetic energies used in the experiment.	58
4.2	Fit parameters determined from Raman spectra for different laser energy densities.	61
5.1	Flow speeds and kinetic β	79
6.1	Fit parameters determined from Raman spectra for different copper and titanium concentrations.	99
6.2	Hardness of copper and titanium doped diamond-like carbon as a function of concentration. Dopant concentration is calculated from experimental conditions	101
6.3	sp^3 fraction of copper and titanium doped diamond-like carbon as a function of concentration. Concentrations are calculated from EELS and from the experimental conditions.	104

Chapter 1

Introduction

Carbon is a very common element which possesses several allotropes, graphite, diamond, fullerenes, and nanotubes. In this dissertation, the properties of graphite and diamond are of the most interest. The physical properties of these two allotropes are dramatically different. Graphite is soft due to the weak Van der Waals bonding perpendicular to the planes of carbon atoms, conducts electricity, and is opaque. Diamond, however, is the hardest known material, a poor conductor of electricity, and is optically transparent. The differences in properties between allotropes are due to bonding and crystal structure. The ground state electronic structure of a carbon atom is $1s^2 2s^2 2p^2$. This might indicate that carbon is only able to form two bonds via sharing of its $2p$ electrons. However, excitation and bond hybridization allow the formation of more than two bonds. In the electron excitation process, one of the $2s$ electrons is promoted to an empty $2p$ orbital to form $1s^2 2s 2p_x 2p_y 2p_z$. Hybridization of the valence electrons $2s 2p_x 2p_y 2p_z$ permits the formation of more than two bonds. If all the valence electron orbitals are hybridized, four bonds may be formed. This is the case of diamond. Since one $2s$ orbital and three $2p$ orbitals have been hybridized, this is termed sp^3 bonding. In the case of graphite only three of the four valence orbitals are hybridized, one $2s$ and two $2p$ orbitals. Thus, the type of coordination found in graphite is termed sp^2 . Carbon atoms in sp^3 coordination may form up to four σ bonds, which are bonds directed along the orbital direction. Carbon atoms in sp^2 coordination may form up to three σ bonds, and a single π bond from the unhybridized $2p_z$ orbital. Bonds which are perpendicular to the direction of the electron orbital are termed π bonds.

Crystalline and amorphous forms of carbon are present naturally and may be prepared in the laboratory as well. Amorphous carbons prepared experimentally have been given a number of different names: amorphous carbon, diamond-like carbon, tetrahedrally bonded amorphous carbon, hydrogenated amorphous carbon, and others. In the literature, these names are often used interchangeably, and without rigorous definition. For instance, the term “amorphous diamond” is only appropriate if all carbon atoms in the film are sp^3 coordinated. However, this term is sometimes used in literature for amorphous carbon films which possess some fraction of sp^2 coordination. For this dissertation, “diamond-like carbon films” (DLC) will be defined to mean those films which are hydrogen free, tetrahedrally bonded amorphous carbon. Here, hydrogen free

means that hydrogen is not necessary to preserve the structure of the films. These films possess a large fraction of sp^3 bonded carbon atoms, although there may be some sp^2 bonding present. The sp^3 coordinated carbon atoms form a rigid three dimensional network in which sp^2 coordinated carbon atoms may exist.[1, 2, 3] The sp^2 coordinated carbon atoms may be organized in to hexagonal rings or in to chains.[2] However, the carbon atoms in the film possess no long range order.[4, 1]

Diamond-like carbon films possess properties similar to the properties of diamond. Such properties include: chemical inertness, high thermal conductivity, high hardness and wear resistance,[4, 1, 5, 6, 7] transparency in the optical and infrared spectra,[1, 8, 9] and interesting electrical properties.[4, 8, 9, 10, 11] Thus, DLC films have found use in coatings for replacement hip joints, [12] electron injection layers,[13], magnetic disk drives,[14], antireflection layers,[1] and other applications.[4, 1]

Typical values of DLC film hardness are between 30 and 180 GPa.[4] The hardness of diamond-like carbon films increases with increasing sp^3 fraction of the film. The ordering of the sp^2 phase, whether in rings or chains, does not greatly affect the hardness of the DLC film.[4, 1, 15] Film hardness is a result of the strong, highly directional σ bonds.[1] These bonds create a strong three dimensional network, in which sp^2 sites may be located.[1] The creation of these bonds forms large internal compressive stresses, which cause film delamination after a certain critical thickness. An excellent example of this is shown in Fig. 4 of reference [6]. Two means of stress reduction have been suggested: annealing[16] and dopant addition.[6, 7] Ferrari, et al, found that internal stresses could be removed by annealing at an appropriate temperature.[16] They found that large sp^3 fractions could be maintained even when the stress is relieved, indicating that large internal stresses are not necessary to stabilize the sp^3 structure once it is formed.[16] Stress reduction by annealing occurs via conversion of a small number of sp^3 sites to sp^2 sites.[16] Above 1100 Celsius, the large sp^3 fractions cannot be maintained. Wei, et al, investigated the stress reduction in diamond-like carbon films via doping.[6, 7] They used pulsed laser deposition to deposit DLC with different dopants, such as silicon, copper, and titanium. They found that titanium was more effective than copper or silicon at stress reduction.[6] The compressive stress is reduced due to the distortion of the bonding of outer shell electrons of titanium.[6]

Optical properties of DLC films are functions of both sp^3 fraction and the ordering of the sp^2 phase.[9, 3] A typical means by which the optical properties of DLC films are quantified is the Tauc gap. The Tauc gap is a measure of the minimum photon energy which may be transmitted through the material. It is typically determined from the complex portion of the dielectric function of the material.[17] The optical properties of DLC films are controlled by the π states which reduce the optical gap.[9] Thus, altering the fraction of the sp^2 coordinated sites will decrease the Tauc gap.[9] Chowalla, et al, showed that the Tauc optical gap of DLC films can decrease even if the sp^3 fraction is constant by changing the ordering of the sp^2 phase from chains to aromatic rings.[3] Films with large sp^3 fractions and with sp^2 coordinated carbon ordered in to chains will be optically transparent in the visible region. Transparency in the infrared region is controlled by the presence of hydrogen.[1] The presence of stretching modes between hydrogen and carbon causes

absorption of infrared light.[1] With undoped, hydrogen-free diamond-like carbon films Wei, et al., showed approximately 50 percent transmittance and a reflectivity of 20 percent in the infrared spectrum.[8, 4] Thus, hard, anti-reflective coatings for infrared optics may be created from diamond-like carbon films.

Electrical properties of DLC films are most dependent on the sp^2 phase.[4, 9] The results of Ferrari, et al., and of Chowalla, et al., indicate that the resistivity of DLC films is dependent on the ordering of the sp^2 phase.[3, 16] They found that resistivity of the film can change even if the sp^3 fraction of the film does not change. If the sp^2 chains or rings increase in size and begin to link together, the electrical conductivity will increase, as indicated by Marks, et al., and by McCulloch, et al.[18, 19] The typical electronic conduction mechanism in DLC films is hopping between localized states.[1, 4, 8] Undoped diamond-like carbon is a p-type semiconductor.[4, 1] The addition of certain dopants can create n-type diamond-like carbon. Titanium and silicon doped DLC films have been shown to be n-type conductors.[8] Doping with nitrogen and phosphorus also creates n-type diamond-like carbon.[1] Thus, with the use of appropriate dopants, diamond-like carbon may be used as an electronic material.

As discussed above, the sp^3 fraction and the ordering of the sp^2 phase affect the optical, electronic, and mechanical properties of diamond-like carbon films.[3, 2, 15, 20, 16] It is therefore important to understand how the sp^3 fraction and sp^2 microstructure are affected by growth techniques. A variety of different growth techniques are used:

- I Aisenberg and Chabot produced the first diamond-like carbon films were grown by ion beam deposition.[21] They used a Kaufmann ion source with methane as their source gas. Vacuum arc deposition and mass selected ion beam deposition are also used. The ion beam deposition techniques produce ions with a narrow energy distribution, especially mass-selected ion beam(MSIB).[4] If the distribution of ion energies is narrow, then control of the properties of the film may be more direct.[1]
- II Sputtering techniques are also used to produce DLC films. A simple ion beam sputtering device uses argon ions accelerated to large voltages, $\approx 1 \text{ kV}$, to sputter material from a graphite target. Magnetic sputtering involves the use of a plasma with an applied magnetic field to sputter atoms from a carbon target. The substrate is typically placed at a potential near 100 V.[1] This permits acceleration of ions across the sheath to drive the formation of DLC. It can allow for large throughput, however deposition rates are low at optimal conditions for the creation of high sp^3 fraction DLC films.[4]
- III Chemical vapor deposition(CVD) techniques are often used to produce both crystalline diamond films, and diamond-like carbon films.[22] The CVD techniques are sometimes enhanced via the presence of a plasma, such as a microwave or DC glow discharge.[23] Diamond-like carbon films produced by CVD typically have a large hydrogen concentration less strong than those formed through other techniques. Hydrogen is necessary to stabilize the film structure in this case.[4]

IV Pulsed laser deposition(PLD) is also used to produce hydrogen-free diamond-like carbon films.[24, 4, 1] It has advantages over other techniques, including preservation of target stoichiometry in film, better film quality at lower temperatures, a reduced thermal budget, and deposition rates comparable to molecular beam epitaxy. In PLD, a laser is used to ablate a target, which creates a plasma at the laser target interface. This plasma propogates outwards, and deposits on a substrate. Thus, to understand film growth and properties, an analysis of the plasma properties is needed.

A number of authors have attempted to simulate the expansion of the laser ablation plume. Analytic simulations have been made with the assumption of adiabatic expansion. Zel'dovich and Razeir discuss the adiabatic expansion of a spherical gas cloud in to vacuum.[25] They show the conversion of thermal energy initially within the spherical cloud to the kinetic energy of flow. This is similar to the processes involved in laser ablation and deposition, although the expansion is not spherically symmetric. Singh and Narayan developed an adiabatic expansion model specifically for laser ablation.[26] The initial plume formation during the laser pulse proceeds isothermally, while the expansion after the laser pulse is adaibatic. Saenger extended this model to multiple species targets for the purposes of investigating deviations from stoichiometry in deposition of multicomponent films.[27] Atoms of different masses will have differing distributions within the film.

Since these articles have been published, authors have attempted numerical simulations of the expansion process.[28, 29, 30, 31] The simulations were performed on the fluid equations of motion for gases expanding in to a vacuum and in to gases at various pressures.[28, 29, 30, 31] Leboeuf, et al, accounted for ionization, although this was only considered in the energy balance, not the equations of motion.[28, 29] Their key result was to show flow velocities in excess of those predicted by Zel'dovich and Razier, and more agreeable with experimentally determined values. They also showed plume spilliting which occurs in the laser ablation of targets at pressures great enough to consider interactions of the plasma with background gases.[32] Itina, et al.,[31] and Garrelie, et al.,[30] use Monte Carlo techniques to model plume expansion. Their Monte Carlo based simulations also show the conversion of thermal energy to kinetic energy during the expansion process. Their models show excellent agreement with spectroscopic time-of-flight studies on laser ablation plumes.[30, 31]

Recently, authors have considered the behavior of a fully ionized plasma during expansion in terms of the fluid approximation and kinetic theory.[33, 34, 35, 36] Their key results are to show the presence of an electric field due to charge separation during expansion. Electrons, with their smaller mass, attempt to leave the plume before the ions. Ions are then accelerated in the presence of this electric field. It has been seen experimentally that ions travel faster than neutral particles, and that more highly charged ions travel faster than ions in lower ionization states.[37, 38] They also predict that the distribution of ion velocities expanding in to space to not be Maxwellian, as would be expected from a source of non-interaction, isothermal, particles.

One disadvantage of the PLD technique is the possibility that macroscopic particulates may be removed

from the target material. Clearly, this is not advantageous for the creation of high quality films. One solution which has been suggested is to apply a magnetic field perpendicular to the flow direction to deflect the plume. [39, 40, 41] In order for plume deflection to be effective, the ions would have to follow a curved path through the magnetic field. However, it is unknown to what degree the plume will be deflected. There is indication that the plume is not deflected at all. [39, 42, 43, 44, 45]

The interaction of flowing plasmas with magnetic field is not entirely understood. A number of early investigations suggest that instabilities play a dominant role in the physics. [46, 43, 42, 45, 44] The presence of instabilities and turbulence permits enhanced transport. [46, 44] For instance, the Rayleigh-Taylor (RT) instability may grow as the plasma expands against the magnetic field where the magnetic field geometry is favorable. [47] Ripin, et al, observe a large Larmor radius RT instability which has a larger growth rate than the classical RT instability. However, their laser energies ($E_L = 30 J$) and powers ($P_L = 10^{13} J$) are significantly larger than those in this experiment. [43] Neogi and Thareja also observe, using a charge coupled diode, a Rayleigh-Taylor instability. [48] Peyser, et. al, and Mostovych, et. al., show evidence of an electron-ion hybrid instability. [42, 45] This instability is a Kelvin-Helmholtz type instability in which the ion Larmor radius is greater than the velocity shear length. [42] Their instabilities are observed at the plasma-vacuum boundary, not in the bulk of the plasma.

Increases in electron temperature have also been observed via optical spectroscopy and Langmuir probe techniques. Koopman found a significant increase in electron temperature, from 1 eV to 40 eV in copper plasma expanding across a magnetic field using a Langmuir probe. [46] Given his large field displacements, this is likely due to both plume slowing and to field line diffusion. Harilal, et al, observed a similar increase in electron temperature using optical spectroscopy, although not to the same magnitude. [49] It should be noted, however, that their measurements are time integrated and based on spectroscopy, and thus represent a temporally and spatially averaged average electron temperature. Neogi, et al, have observed similar small increases (1 – 2 eV) in electron temperature via optical spectroscopy. [50] In one article, they assume that the plasma emits like a black body, which was not verified for their experiment. [50] In the other articles, they assume local thermodynamic equilibrium, although they do not verify this and do not show Boltzmann plots. [40, 51] Without validation of these assumptions, the temperature data may be inaccurate.

Several authors have studied the effect of an external magnetic field on the deposition of diamond-like carbon. Diaz, et al, used an external magnetic field to deflect a carbon plasma plume created in pulsed laser ablation. [52] For a magnetic field of 0.8 T they observe complete deflection of the plume via Faraday cup measurements. [52] They found, using visible Raman spectroscopy, that the sp^3 fraction of the deposited diamond-like carbon film decreased when the plume was fully deflected. [52] Minami, et al, used a quarter-torus to guide the charged component of the laser ablation plume for deposition. [53] They found that the sp^3 fraction was increased when using solely the charged component of the plume. [53] Qingrun and Gao found no apparent plume deflection in a 0.04 T magnetic field. They also found that the hardness of diamond-like carbon films was increased and that the film thickness was more uniform in the presence of an external

magnetic field.[39] The results of these authors indicate that the ions and neutral atoms within the plume may play different roles in film growth.

In this dissertation, the processes involved in the growth of diamond-like carbon films are investigated. Plasma properties are studied and related to film growth and properties. The dissertation is organized in the following manner. First, the experimental setup is described in Chapter 2. Detailed discussions of theory and corrections to the Langmuir probe under magnetized conditions are discussed in Chapter 5. Second, plasma plume physics as determined by Langmuir probes and mass loss measurements, applicability of Langmuir probes to time-of-flight analysis, and plume substrate interactions are discussed in Chapter 3. The relationship between laser energy density, plume parameters, and film sp^3 fraction is described in Chapter 4. Chapter 5 investigates the plasma physics of the plume under magnetized conditions. The structure and properties of doped diamond-like carbon films are discussed in Chapter 6. Conclusions are presented in chapter 7. Finally, ideas for future reasearch are presented in Chapter 8.

Chapter 2

Experimental

2.1 Pulsed Laser Deposition

The pulsed laser deposition system used in this dissertation research consists of an excimer laser, optical bench, vacuum chamber, and target/substrate assembly. The laser is a Lambda Physik KrF excimer laser LPX 210, with a maximum energy of 700 *mJ* and a full pulse length of 45 *ns*. Its operating wavelength is 248 *nm*. The optical bench is a set of mirrors and lenses which directs and focuses the laser beam to the target inside the vacuum chamber. The final lens on the optical bench can be moved to adjust the spot size on the target. The laser beam is directed such that the laser strikes the target at a 45⁰ angle. A simple drawing of the setup is shown in Fig. 2.1.

The vacuum chamber is a six-inch, six-way cross constructed from stainless steel. A diagram of the chamber is shown in Fig. 2.2. Attached one port is a turbomolecular pump backed by an oil-free mechanical pump. The maximum vacuum after bake-out is $\approx 1 \times 10^{-9}$ *Torr*. One of the smaller ports is used to insert the Langmuir and magnetic probes which are used in the analysis of the plasma produced in pulsed laser deposition. A Wilson seal vacuum flange permits the probes to be moved within the chamber while keeping the pressure constant. It is important to note that the probe is off the centerline of the plume by 5 *mm*. This will affect the analysis of the Langmuir and magnetic probe results.

A diagram of the target and substrate holder are shown in Fig. 2.3. The target and substrate holder form the top of the vacuum chamber. It may hold up to four targets, although only two are shown in Fig. 2.3. The target holder rotates the target at six revolutions per minute to prevent pitting of the target material. Two substrate holders are used for the experiments. For the unmagnetized depositions, a standard ceramic substrate holder with heater is used. A special substrate holder was used for the magnetized depositions, and for the analysis of the plume under magnetized conditions. All depositions took place at room temperature.

To investigate the effect of laser energy density, and thus varying plasma properties, on film growth and properties, a series of depositions were performed. The laser energy densities chosen were 1.6, 2.0, 2.5, and 3.2 *J/cm*². The last focusing lens on the optical bench was at 12 cm, yielding a laser spot size on target for

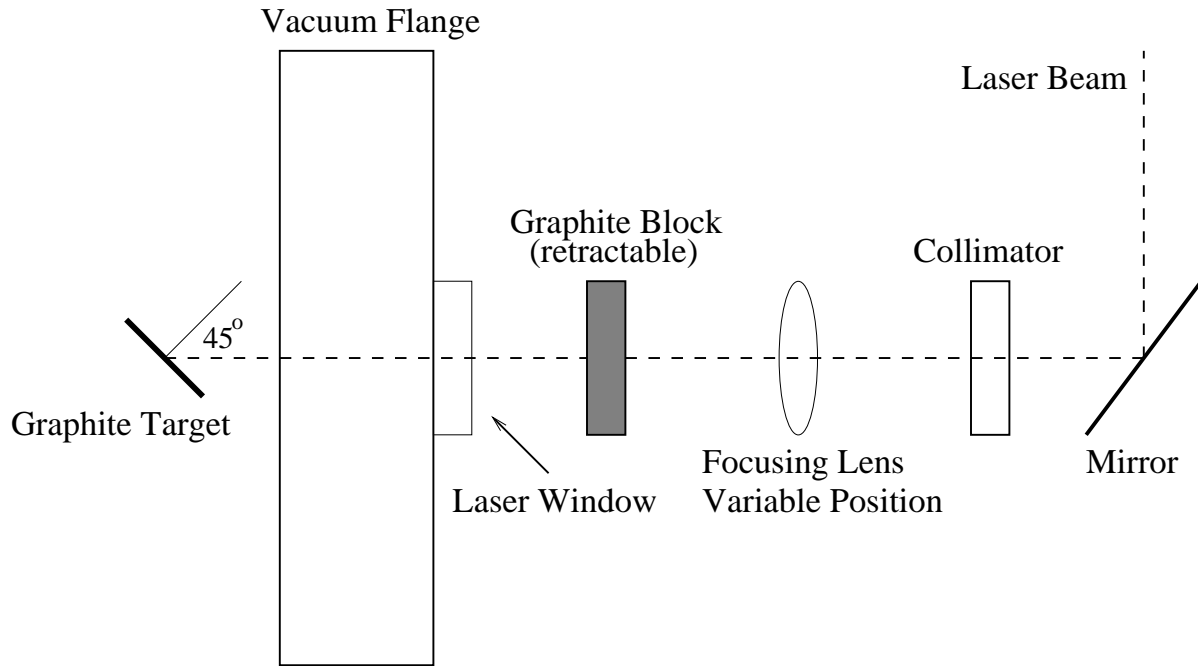


Figure 2.1: Experimental setup showing optical bench.

each deposition of 0.22 cm^2 . The target was struck by the laser at a repetition rate of 10 Hz for 55 s . This produces thin DLC films with a thickness of $\approx 100 \text{ \AA}$.

To investigate the effect of dopants on film properties, small strips of copper and titanium film were placed on to the carbon target. They are held in place with small clips on the target holder. To change the concentration of dopant in the film, 1, 2, or 4 strips of copper or titanium were placed on the carbon target. As the target rotated, the laser alternately ablated carbon and dopant material. In this case, the laser energy density was held constant at 2.5 J/cm^2 and the spot size was constant as well at 0.22 cm^2 . For these depositions, the laser repetition rate was 10 Hz and the deposition time was $16 \text{ min. } 40 \text{ s.}$, or 10000 pulses. Film thickness is $\approx 2000 \text{ \AA}$. For nanohardness measurements, the films were deposited for a time of 33 min. , producing films of 4000 \AA .

All films were deposited on silicon (100) substrates. Substrates were prepared for depositions by cleaning in an ultrasonic cleaner. The substrates are placed in acetone for five minutes, in methanol for five minutes, and in hydrofluoric acid (HF) for two minutes. Cleaning in HF is necessary to create a hydrogen terminated surface on the silicon. This will prohibit the formation of SiO_2 and allow for good film adhesion.

2.2 Magnetically Assisted Pulsed Laser Deposition

In order to perform depositions under magnetized conditions and investigate the effect of the magnetic field on the plasma, a special magnet and substrate holder was created. A diagram of the magnet and substrate holder is shown in Fig. 2.4. It houses two NdFeB rare earth magnets with a surface field

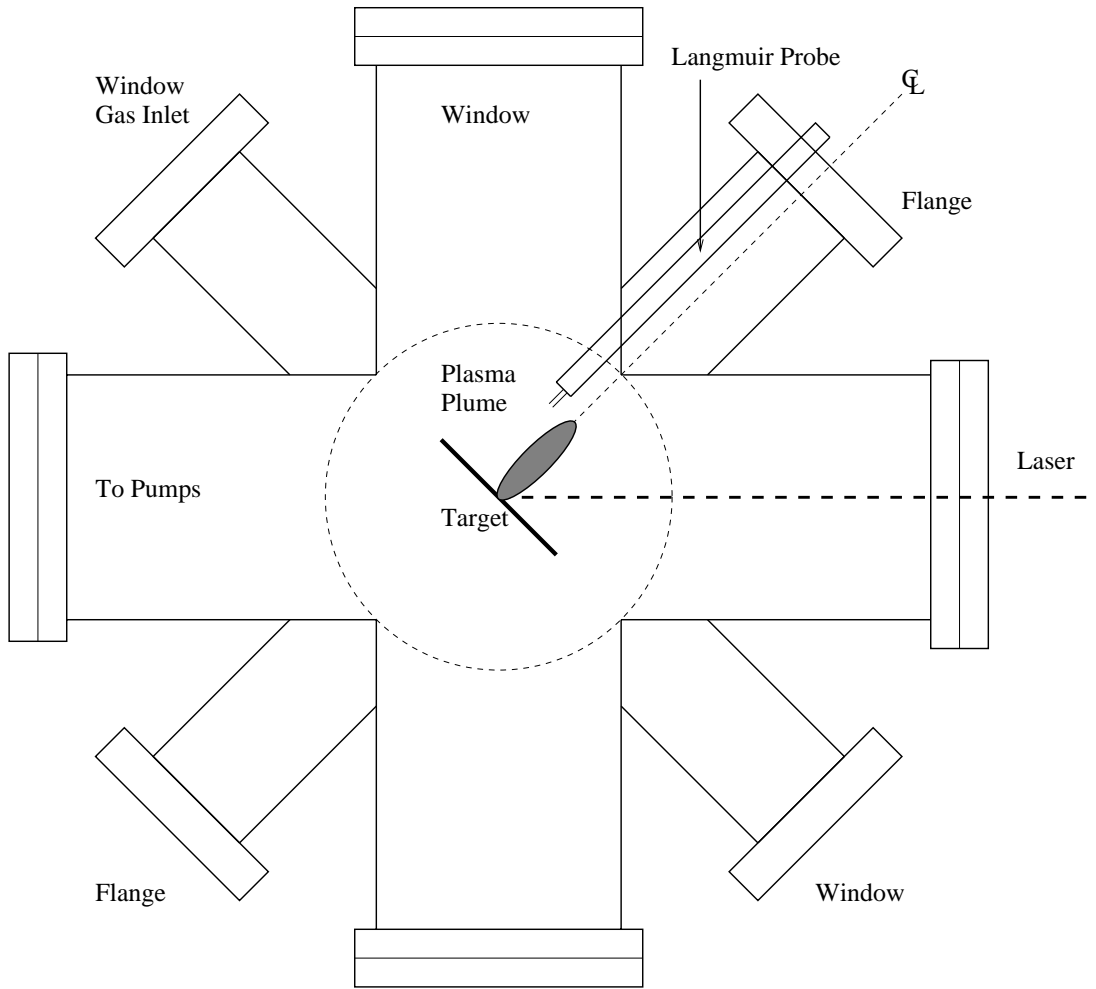


Figure 2.2: Pulsed laser deposition chamber. Note that the Langmuir probe is off the plume centerline. A convectron gauge and an ionization gauge are not shown.

strength of $1.26 T$ purchased from National Imports. These magnets are rectangular and have dimensions of $1 \text{ in.} \times 1 \text{ in.} \times 0.25 \text{ in.}$ The magnets are placed in recesses within the aluminum blocks that form the top and bottom of the substrate and magnet holder. These two aluminum blocks are separated by 3.5 cm by an aluminum substrate holder. For the Langmuir probe experiments, the substrate holder cannot be present as it would block the path of the probe. Instead, the magnets are kept separated at 3.5 cm by nylon screws.

Field strength within the magnet and substrate holder was mapped by using a Hall probe. The Hall probe used is an Applied Magnetics Laboratory Inc. model GM1A Gaussmeter. A plot of the field strength as functions of y and z at $x = 1.25 \text{ cm}$ in the magnet holder is shown in Fig. 2.5. Typical field strength between the magnets and along the centerline, $z \approx 2.25 \text{ cm}$, is between $0.3 T$ and $0.4 T$, close to the magnet surfaces, the field is near $0.9 T$.

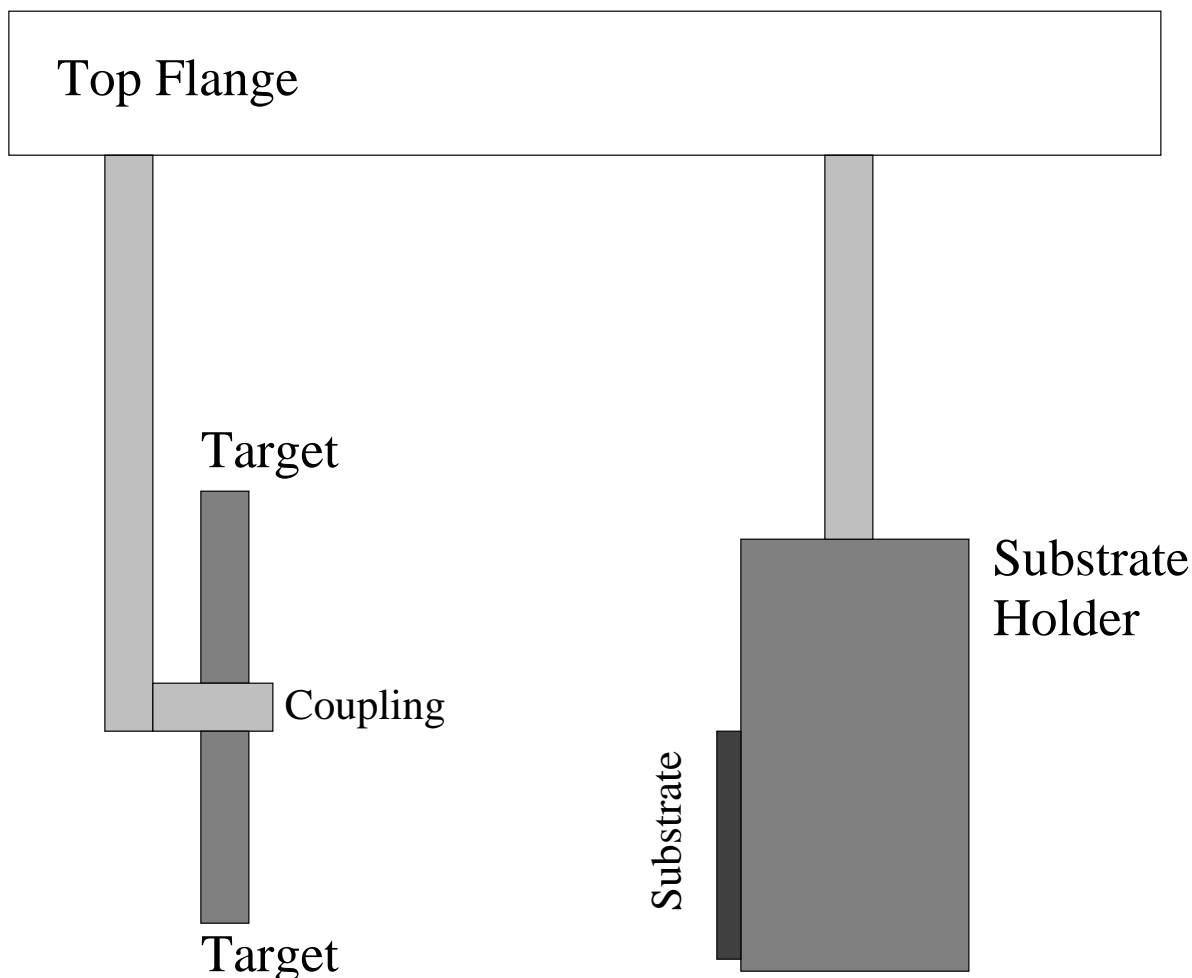


Figure 2.3: Target and substrate holder for the pulsed laser deposition experiments.

2.3 Electron Microscopy

A JEOL 2010F transmission electron microscope(TEM) with a Schottky emitter operating at an acceleration voltage of 200 kV was used for all transmission electron microscopy experiments. A GATAN image filter is used to acquire electron energy-loss spectra and high resolution TEM images. The effects of multiple scattering on the electron energy-loss spectrum are removed by Fourier-log deconvolution.[54]

All TEM samples are plan view and are prepared for electron energy loss spectroscopy via chemical polishing. This is done to avoid the damage caused by ion milling.[55] Discs are cut from the silicon substrate with an ultrasonic cutter. A dimple is then created on the silicon side with an ultrasonic dimple grinder. Acid resistant wax is placed on the film side. A solution consisting of 25 mL hydrofluoric acid, 75 mL nitric acid, and 30 mL of an acetic acid/iodine solution is used to etch the silicon. The acetic acid/iodine solution is prepared by dissolving 2.5 grams of iodine in 500 mL of acetic acid. Once a small hole is created in the dimple, the disc is removed from the acid solution. The acid resistant wax is removed with trichloroethylene,

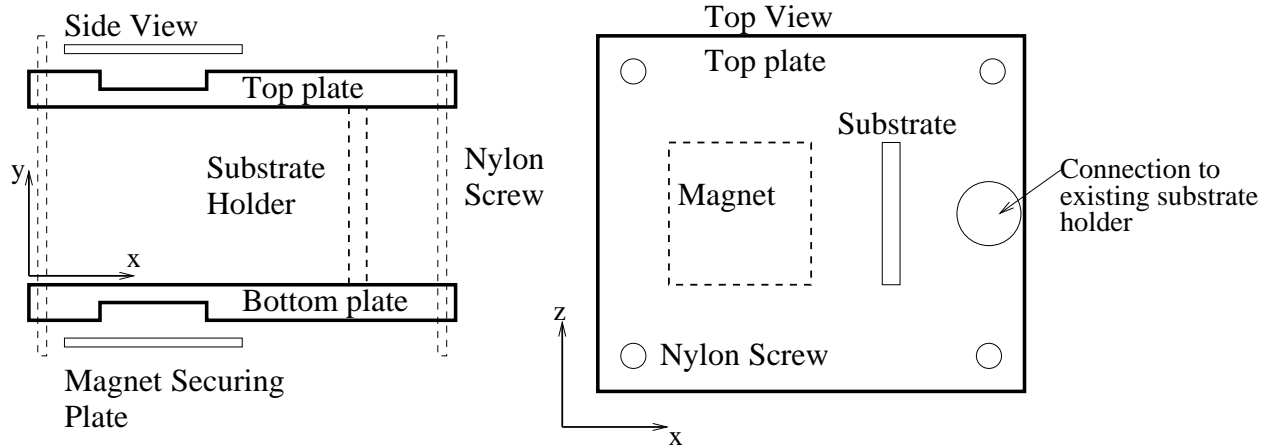


Figure 2.4: Diagram of magnet and substrate holder.

acetone, and methanol. The plan view samples are then fully prepared for analysis in the TEM.

In electron energy-loss spectroscopy, a spectrum of inelastically scattered electrons is recorded. A complete spectrum is recorded by taking spectra over multiple energy windows. A drift tube on the EELS spectrometer permits different energy ranges to be selected. For the undoped specimens, the drift tube was biased to voltages of 0, 100, 200 or 250, and 300 Volts. For doped specimens, further spectra were taken at larger drift tube potentials to observe dopant ionization edges which occur at larger energy losses. For Ti, the drift tube voltage was increased to 400 V to observe the Ti $L_{2,3}$ edge. For Cu, the drift tube voltage was increased to 900 V to observe the Cu $L_{2,3}$ edge. The complete spectrum is created by splicing the individual spectra together with appropriate scale factors. The spectrum provides information on the structure of the material examined. Using different energy windows is necessary as the ionization-edge features are typically several orders of magnitude smaller than plasmon or zero-loss features.

It is typically assumed that the sample is sufficiently thin such that the electron only undergoes a single inelastic scattering event. However, there is a probability that the incident electron will scatter inelastically multiple times within the sample. This effect may be removed from the spectrum via Fourier-log deconvolution. Fourier-log deconvolution will produce a spectrum that is the result of single inelastic scattering events within the specimen. The complete, raw, spectrum $J(E)$ and the spectrum containing only the zero loss peak $Z(E)$ are necessary. If $j(k)$ and $z(k)$ are the Fourier transforms of the complete spectrum and the zero loss spectrum, respectively, then the Fourier transform of the single scattering spectrum $j^1(k)$ is:[54]

$$j^1(k) = z(k) \ln \left(\frac{j(k)}{z(k)} \right) \quad (2.1)$$

The inverse Fourier transform of Eq. 2.1 is the single scattering distribution $J^1(E)$. To reduce noise within the deconvolved spectrum, the complete, raw, spectrum is extended with power-law functions on right and left ends of the spectrum. Deconvolution of the spectrum is performed before any analysis is attempted.

An electron may lose energy through a number of different interactions with the material. First, an

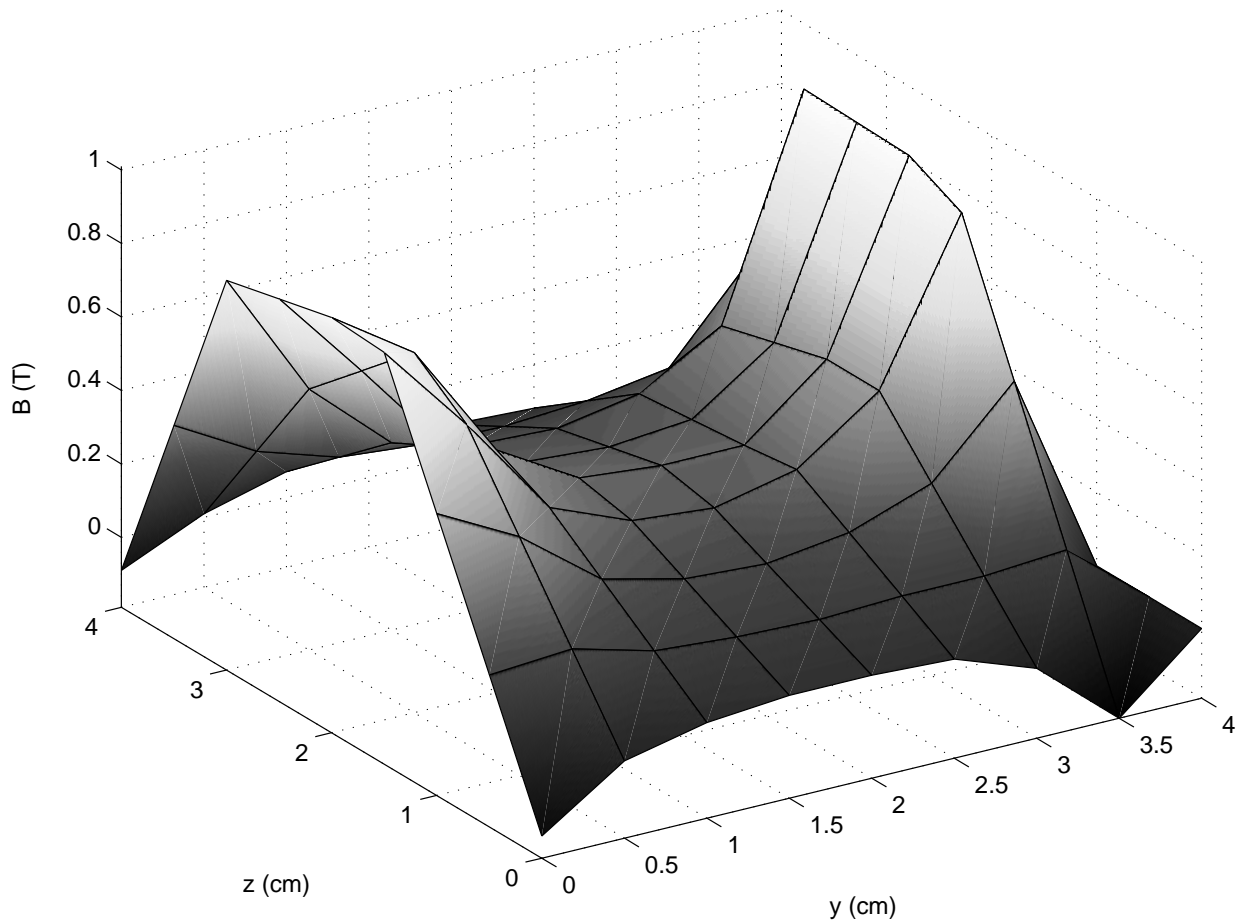


Figure 2.5: Plot of magnetic field strength within the magnet and substrate holder.

incident electron may cause sample electrons to undergo interband transitions. The energy loss from these interactions can be used to study the electronic structure of the material.[54] Second, an incident electron may excite a collective oscillation of sample valence electrons. Due to its similarity with an electron plasma oscillation, this is known as a plasmon. In a plasma, the electron plasma frequency is proportional to the electron density within the plasma. The location of the plasmon in the EELS spectrum permits an estimation of the valence electron density, and thus the atomic density of the sample. For a metal, the Drude free electron model gives the shape of the plasmon region as a function of electron energy loss, E , as:

$$f(E) = \frac{I_0 E_P^2 E \Gamma}{(E^2 - E_P^2)^2 + E^2 \Gamma^2} \quad (2.2)$$

where I_0 is the peak intensity, Γ is the full width at half maximum of the peak, and E_P is the location of the plasmon peak. The Drude model is derived by considering a perturbation of the valence electrons from their equilibrium position, with damping. This model is excellent for metals, however, it is not completely

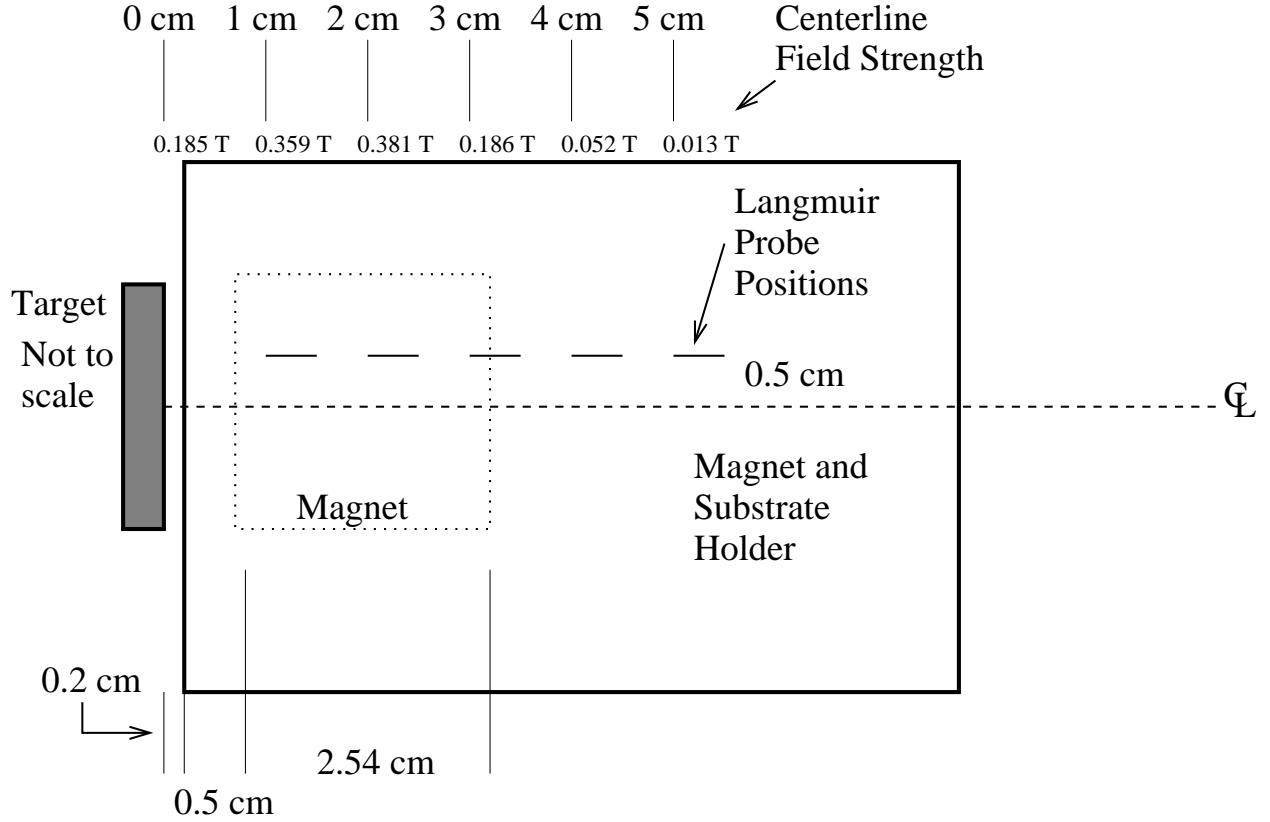


Figure 2.6: Geometry of the target, magnet holder, and Langmuir/ \dot{B} probes. The target and magnet holder are not to scale. The positions of the magnets and the probe positions are to scale.

accurate for semiconductors. Band gap effects in semiconductors alter the dynamics of the electrons as they respond to the perturbation in the local electric field caused by the incident electron. The result of band gap effects is that the electrons in the material behave as if they have a different mass than a free electron. Thus, in the formula for the energy of the plasmon, the free electron mass is replaced with an effective mass.

$$E_P = \hbar \left(\frac{e^2 n_{val}}{\epsilon_0 m_e^*} \right)^{1/2} \quad (2.3)$$

In Eq. 2.3, \hbar is Plank's constant divided by 2π , n_{val} is the valence electron density and m_e^* is the effective electron mass. Ferrari, et al.,[56] calculated the effective electron mass in diamond-like carbon by using two different, independent methods of calculating electron density within the film, EELS plasmon analysis and X-ray reflectivity. They estimate an effective electron mass of $0.87m_e$. This mass is used in all future calculations.

Mass densities in the DLC films were estimated by fitting the plasmon region to Eq. 2.2. This is performed using a non-linear least squares package. The fit returns the full width at half maximum, Γ , and the location of the plasmon peak, E_P . From the plasmon peak location, the film mass density is calculated using Eq. 2.3.

Another means by which the incident electrons lose energy to the sample is by ionization. The incident

electron may excite an inner shell electron to an antibonding state. Those carbon atoms which are bonded in sp^3 coordination have formed four σ bonds. Carbon atoms bonded in sp^2 coordination have formed three σ bonds and one π bond. The incident electron can excite a $1s$ electron to a π^* or σ^* antibonding state. The π^* and σ^* antibonding states differ by ≈ 5 eV, with the π^* peak located at approximately 285 eV. Typically, the π^* peak is seen as a small shoulder on the larger σ^* peak. A direct means of calculating the sp^3 fraction within a carbon film has been suggested by several authors.[56, 57, 58] The method relies on the types of bonds that sp^3 and sp^2 coordinated carbon forms. If I_π is the integral intensity of the π^* peak in the specimen, and $I_{\Delta E}$ is the integral intensity of the π^* and σ^* peak, the ratio $I_\pi/I_{\Delta E}$ is the fraction of π bound electrons within the sample. Performing the identical comparison on an entirely sp^2 bonded sample, in this case microcrystalline graphite on amorphous carbon yields the fraction of π bound electrons in an sp^2 only sample. The fraction of sp^3 coordinated carbon atoms in the sample assuming that there are only sp^2 and sp^3 coordinated carbon atoms present is:

$$f = 1 - \frac{I_\pi/I_{\Delta E}}{I_\pi^{ref}/I_{\Delta E}^{ref}} \quad (2.4)$$

In the doped specimens, ionization edges from copper or titanium will be present. The fraction of titanium or copper is estimated from the magnitude of their ionization edges. From Egerton, the ratio of the concentration of two elements may be calculated from the intensity of certain edges and the partial ionization cross sections:

$$\frac{N_a}{N_b} = \frac{I_j^a \sigma_j^b}{I_j^b \sigma_j^a} \quad (2.5)$$

In Eq. 2.5, the ratio of the concentration between elements a and b , is $\frac{N_a}{N_b}$. The intensity of the ionization edge from element a of type j is I_j^a , and the ionization edge from element b of type j is I_j^b . The partial ionization cross section for element a of edge type j is σ_j^a . Similarly, σ_j^b is the partial ionization cross section of type j for element b . It is important to note that the intensities and ionization cross sections are defined for a specific choice of the collection angle, β . For all experiments, the collection semiangle was 13 mrad. The intensities of the ionization edges are taken over a range Δ . Thus, the cross sections required are partial cross sections, integrated from the differential cross sections over an energy range Δ and a solid angle of acceptance for the detector β . It should be noted that this is a very localized means of determining the concentration of dopants. The fraction of titanium or copper is determine from Eq. 2.5 assuming only carbon and the dopant is present:

$$f_i = \frac{1}{1 + N_C/N_i} \quad (2.6)$$

where N_C/N_i is the ratio of carbon to the dopant material i .

2.4 Hardness Testing

For the hardness testing experiment, a MTS nanoindenter was used. Small samples were cut from the DLC films doped with copper and DLC films doped with titanium. For all samples, two sets of nine

nanindentations in a 3 by 3 array were performed. The direct contact module head was used with the standard hardness continuous stiffness measurement method. Depth of indentation was 500 *nm*. The unloading cycle was started when the maximum load was reached. Another set of nanindentations was performed with a indentation depth of 75 nm so that more accurate data on nanohardness and modulus could be obtained. In both sets of nanindentations, the harmonic contact stiffness was adjusted after each set of indents.

2.5 Visible Raman Spectroscopy

Visible Raman spectroscopy is another commonly used technique for the analysis of DLC films. It has advantages over electron energy-loss spectroscopy in that it is nondestructive and requires no specialized sample preparation procedures. The principle of Raman spectroscopy is that when incident photons scatter from the surface of a material, they may interact with lattice vibrations (phonons) present in the material. Incident photons may gain energy from, or lose energy to, phonons within the material. The spectrum of scattered radiation yields information on the structure of the material. In depth discussions of the theoretical nature of the Raman effect may be found in the literature.[59, 60] A detailed discussion of Raman analysis of DLC films is given by Ferrari and Robertson.[2]

In the visible Raman spectrum of DLC films, there are two important features. These features are known as the G and D peaks. The G peak results from the stretching motion between any two carbon atoms. It is typically located between 1580 and 1600 cm^{-1} in DLC films. The exact location of the G peak is related to the atomic separation and bond strength. These factors may be altered by local stress and bond type. An isolated sp^2 dimer has a G peak wavenumber of 1650 cm^{-1} , while an sp^2 dimer created by the implantation of *Xe* ions within diamond has a G peak wavenumber of 1634 cm^{-1} . [61] Thus, the location of the G peak can give information on the structure of the film. The Raman D peak results from the breathing motion of hexagonal rings of carbon. This peak is typically located at 1330 cm^{-1} in DLC films. In perfect graphite crystals, this vibrational mode is not allowed. The presence of this peak in Raman spectra of DLC films is an indication that the film contains carbon atoms organized in to hexagonal rings.

It should be noted that visible Raman spectroscopy does not provide direct information on the sp^3 component of DLC films. Rather, visible Raman spectroscopy is most sensitivtive to sp^2 sites. [2, 62] Visible photons have a smaller cross section for the excitation of σ bonded sites than for excitation of π bonded sites. Thus, it provides direct information on the sp^2 microstructure, and indirect information on the sp^3 fraction under certian conditions.[2] Ultraviolet Raman spectroscopy may provide a means for direct calculation of the sp^3 fraction. [20, 63]

There are a number of suggested means for analyzing the Raman spectra. Typically, the G and D peaks are fit with Gaussian lineshapes,[64, 7, 6] Lorentzian lineshapes,[15] Breit-Wigner-Fano lineshapes,[62, 20] or some combination thereof. The Breit-Wigner-Fano(BWF) lineshape is an asymmetric, or "skewed",

Lorentzian. For comparison with existing data, the BWF lineshape with a linear background is used.

$$I(\omega) = \frac{I_0 \left(1 + \frac{2(\omega - \omega_0)}{Q\Gamma}\right)^2}{1 + \left(\frac{2(\omega - \omega_0)}{\Gamma}\right)^2} + a\omega + b \quad (2.7)$$

In Eq. 2.7, $I(\omega)$ is the intensity of the G peak at wavenumber ω , I_0 is the peak intensity, ω_0 is the peak location, Γ is the full width at half maximum of the peak, Q is the skewness factor, and a and b are the linear fit parameters. The wavenumber ω is typically given in units of cm^{-1} . Raman spectra are fit to the BWF lineshape for the G peak with a non-linear least squares fitting algorithm. In the further analysis, the location of the G peak is given as the location of the G peak maximum, rather than ω_0 as determined by the non-linear least squares fit. The G peak maximum is found as:

$$\omega_{max} = \omega_0 + \frac{\Gamma}{2Q} \quad (2.8)$$

In the past, the sp^3 fraction has been estimated from the ration of the intensity of the visible Raman D and G peaks. This, however, is incorrect as visible Raman spectroscopy only measures the sp^2 component of the DLC films. However, this ratio indicates the ordering of the sp^2 phase. If $I(D)/I(G) \approx 0$, then the sp^2 carbon atoms are ordered in chains, rather than hexagonal rings. In nanocrystalline graphite, the $I(D)/I(G)$ ratio is a measure of the nanocrystallite size.[2] Another indication of the ordering of the sp^2 phase is Γ , the full width at half maximum of the G peak. The width of the G peak is related to the distribution of sp^2 chain sizes.[2] As the distribution of sp^2 chain sizes becomes increasingly narrow, the full width at half maximum of the G peak decreases.

Currently, sp^3 fraction is estimated from visible Raman data via the location of the G peak. This is possible due to the fact that the sp^3 and sp^2 phases grow together.[2] Any external influence, such as annealing or ion implantation, will alter the relationship between the two phases.[2] When fit with the BWF function, the G peak position ω_{max} is found to increase with increasing sp^3 fraction. The theory of Ferrari and Roberston suggests that this is due to the sp^2 phase changing its ordering from rings to chains, which then become increasingly shorter with increasing sp^3 fraction.[2] The estimation of sp^3 fraction from G peak position is discussed in further detail in Chapter 4.

The peak skewness Q is also taken as an indication of the sp^3 fraction.[62, 20] Large negative values of Q are an indication that the sp^3 fraction of the DLC film is high. Typically, if $Q \approx -10$, the DLC film has an sp^3 fraction of $\approx 80\%$. [57] The physical basis for this change in peak skewness with sp^3 fraction is unclear.

To acquire the Raman spectra, a 514 nm laser was used. The laser illuminated a small section of the DLC sample. Scattered light from the sample was analyzed with a spectrometer.

2.6 Langmuir Probes

A quadruple Langmuir probe is used to acquire data on the ion density and electron temperature within the plasma. The probe is constructed from a one foot long single bore Aluminum Oxide tube with an outer

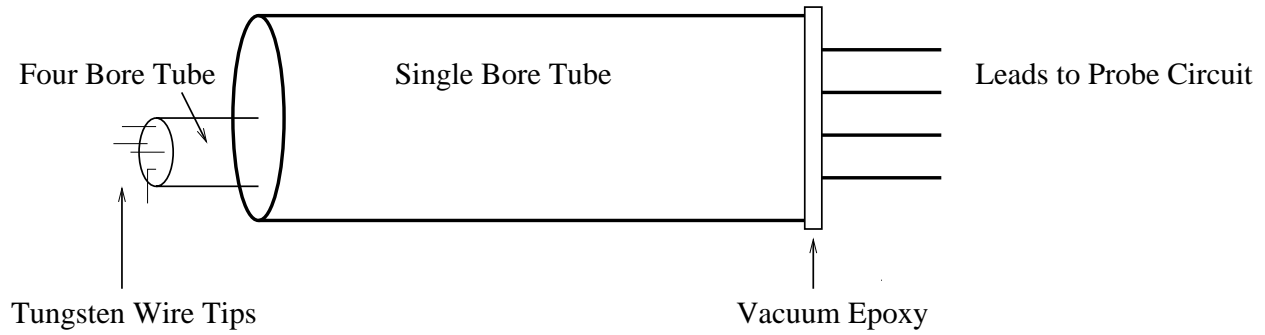


Figure 2.7: Schematic of the quadruple Langmuir probe.

diameter of 0.953 cm and an inner diameter of 0.653 cm . Four tungsten wires with a diameter of 0.025 cm are placed in the single bore alumina tube. A four bore alumina tube is used to keep the tungsten wire separate. The tungsten wires extend 0.5 cm past the end of the four bore tube, which is placed inside the single bore alumina tube. The four bore alumina tube is one inch long with four 0.08 cm diameter bores in a 0.4 cm diameter cylinder. At the other end of the single bore alumina tube a vacuum seal is created with vacuum epoxy. Copper wire leads extend from the vacuum epoxy and are connected on the interior of the single bore tube to the tungsten wires. These copper wire leads are connected to a probe circuit designed to facilitate the acquisition of data on plasma parameters. A diagram of the Langmuir probe is shown in Fig. 2.7

A Hewlett Packard Infinium Oscilloscope with a data acquisition rate of 1 Gigasample per second was used to acquire signals from an Agilent differential probe connected to a special Langmuir probe circuit. Both the laser and the oscilloscope are triggered at the same time with a Stanford Research Systems pulse generator. A Kepco power supply is used to bias the probe circuit. A block diagram of the experimental setup for the Langmuir probe experiments is shown in Fig. 2.8.

In the Langmuir probe experiments, the probe is placed at varying positions from the target surface. The probe distance is measured by touching the probe tips to the target surface, and marking off distances on the single bore ceramic tube. For all Langmuir probe experiments, data were taken at 1, 2, 3, 4 and 5 cm from the target surface.

2.6.1 Unmagnetized Plasmas

The probe equations for charged particle collection in unmagnetized, flowing, plasmas follows from standard probe theory.[65, 66] A probe circuit facilitates the acquisition of temperature and density data without having to sweep the probe voltage. The Langmuir probe circuit used in this experiment is shown in Fig. 2.9. It must be noted that the probe tips are not aligned along the centerline of the plasma plume. The Langmuir probe is offset by 5 mm from the laser spot. This must be taken into account when attempting to calculate plasma parameters by making corrections for the probe offset.

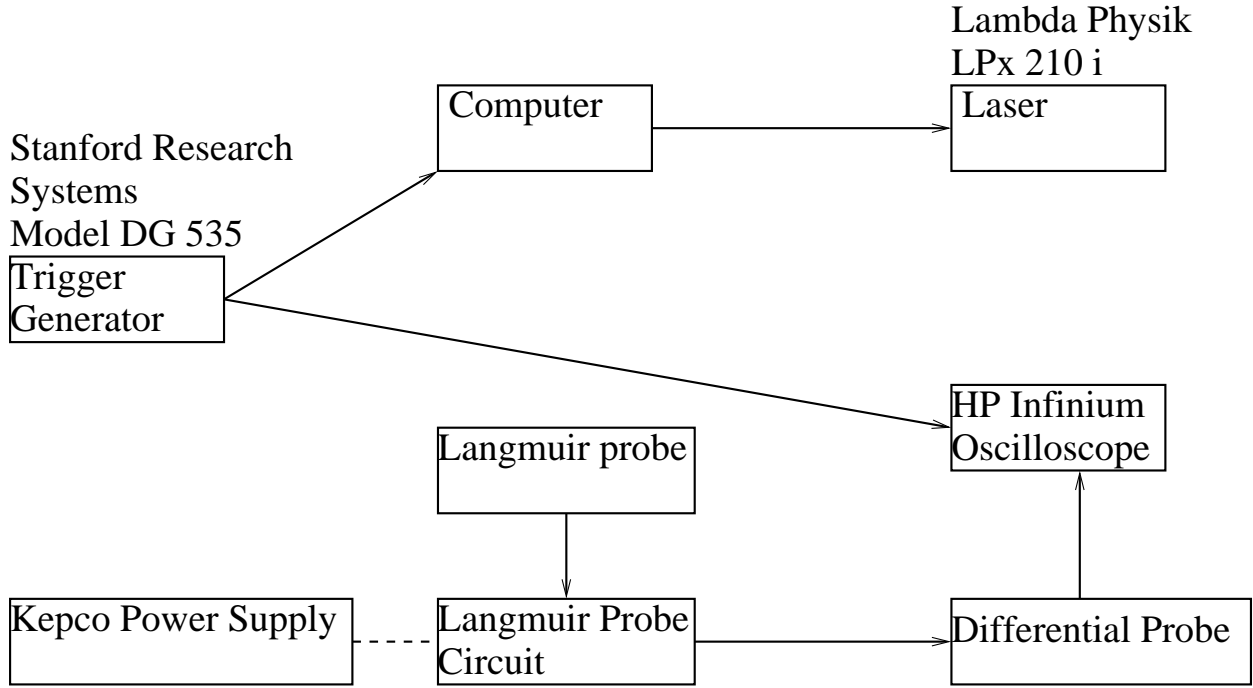


Figure 2.8: Block diagram for Langmuir probe experiment.

The Langmuir probe circuit shown in Fig. 2.9 is completed when the probe is immersed in the laser ablation plasma. Probe 1 is biased at a positive potential, while probes 3 and 4 are biased at a negative potential. For this analysis, it is assumed that probe tip 3 operates in ion saturation. Probe tip 2 is floating, it thus collects no net current. Kirchoff's current law on probe tips 1, 3, and 4 gives an equation for the current flow within the probe.

$$J_e A_{1e} e^{-\chi_1} - J_i A_{1i} = -J_e A_{3e} e^{-\chi_3} + J_i A_{3i} - J_e A_{4e} e^{-\chi_4} + J_i A_{4i} \quad (2.9)$$

In Eq. 2.9, J_e is the bulk electron current density, χ_j is the dimensionless potential of probe tip j , A_{ij} is the area over which probe tip i collects the j th type particle, and J_i is the ion current density. The dimensionless potential is defined as:

$$\chi_i = \frac{e(V_P - V_i)}{kT_e} \quad (2.10)$$

where V_P is the plasma potential, V_i is the potential on probe i and kT_e is the electron temperature. If the Debye length within the plasma is smaller than the probe radius, then the collection areas for each probe are simply the area of each probe tip. Furthermore, it is assumed that the collection area for electrons is identical to the collection area for ions. Thus, $A_{ij} = A = 8.05 \times 10^{-6} \text{ m}^2$ for $i = 1, 2, 3$. However, the geometry of probe 4 necessitates a correction for supersonic flow. In this case, the collection area for electrons is different than that of ions. It is assumed that wake effects prevent the collection of ions and electrons over more than half of the probe area. A visualization of the wake effects on probe tip 4 is shown in Fig. 2.10.

The potential on the probe is not significant enough to deflect the path of the ions, thus ions within the

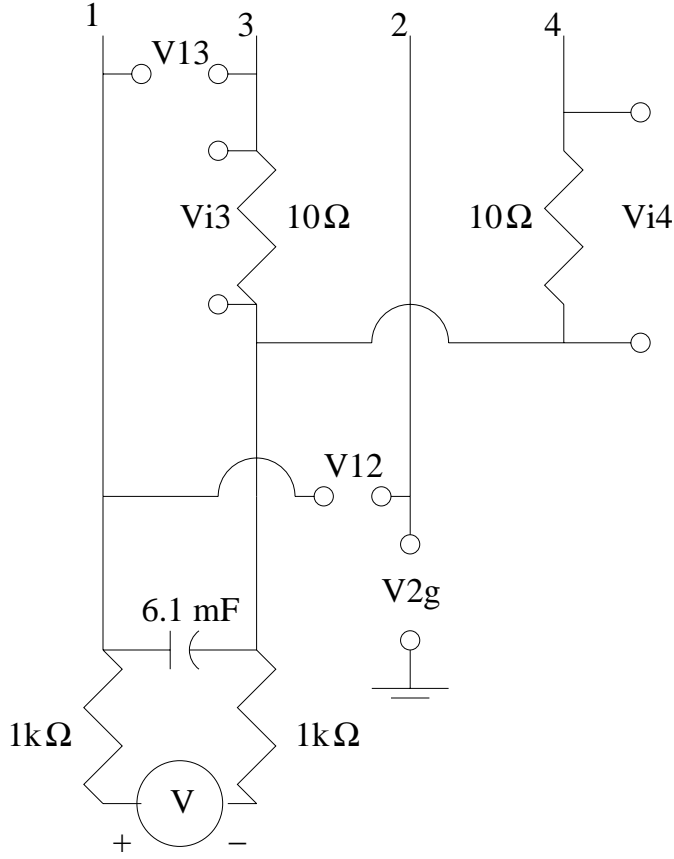


Figure 2.9: Langmuir probe circuit.

flowing plasma only see the projected area of the probe. Electrons however, may be deflected, and thus see half the area of the probe tip. Thus, $A_{4i} = \frac{A}{\pi}$ and $A_{4e} = \frac{A}{2}$. Substitution of the areas A_{ij} in to Eq. 2.9 yields:

$$J_e (e^{-\chi_1} + e^{-\chi_3} + e^{-\chi_4}) = J_i \left(2 + \frac{1}{\pi} \right) \quad (2.11)$$

Under the assumption of ion saturation, $e^{-\chi_3} = e^{-\chi_4} \approx 0$, and Eq. 2.11 is simplified:

$$J_e e^{-\chi_1} = J_i \left(2 + \frac{1}{\pi} \right) \quad (2.12)$$

A second expression for the ion current density in terms of the electron current density is derived from Kirchoff's current law applied to probe 2. Probe two is floating, and thus draws no net current.

$$0 = A_{2e} J_e e^{-\chi_2} - A_{2i} J_i \quad (2.13)$$

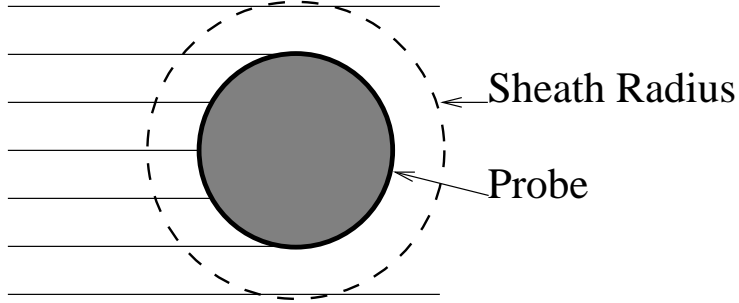
If Eq. 2.13 is solved for the ion current density, and noting $A_{2e} = A_{2i}$, the result is:

$$J_i = J_e e^{-\chi_2} \quad (2.14)$$

Substitution of Eq. 2.14 in to Eq. 2.12 yields:

$$J_e e^{-\chi_1} = J_e e^{-\chi_2} \left(2 + \frac{1}{\pi} \right) \quad (2.15)$$

Ion paths in flow



Electron paths in flow

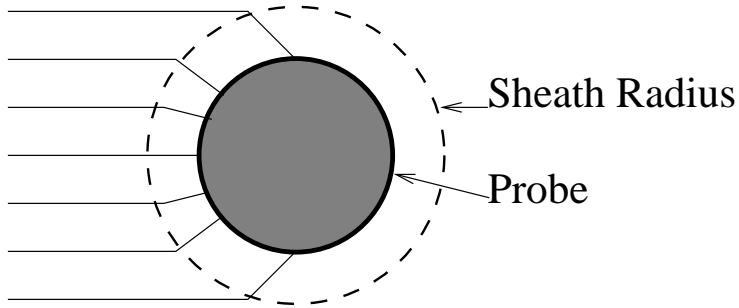


Figure 2.10: Wake effects on probe tip 4 in the quadruple Langmuir probe.

Simplification of Eq. 2.15 gives:

$$1 = e^{\chi_1 - \chi_2} \left(2 + \frac{1}{\pi} \right) \quad (2.16)$$

The expression $\chi_1 - \chi_2$ simplifies to:

$$\chi_1 - \chi_2 = e \frac{V_P - V_1}{kT_e} - e \frac{V_P - V_2}{kT_e} = -\frac{e}{kT_e} (V_1 - V_2) = -\frac{eV_{12}}{kT_e} \quad (2.17)$$

In Eq. 2.17, V_{12} is the potential measured between probe tips 1 and 2 as seen in the circuit drawing of Fig. 2.9. Substitution of Eq. 2.17 in to Eq. 2.16 and taking the natural logarithm of both sides of the result yields:

$$\frac{kT_e}{e} = \frac{V_{12}}{\ln \left(2 + \frac{1}{\pi} \right)} \approx 1.19V_{12} \quad (2.18)$$

The electron temperature in the unmagnetized laser ablation plasma is estimated with Eq. 2.18.

An explicit value of the ion current density, and thus ion current, is found by assuming that the ion collection by a probe tip in ion saturation is the sum of the thermal current which enters the sheath satisfying the Bohm criteria and the current collected due to supersonic flow past the probe tip.[65, 66, 24, 32, 67] Thus, given a plume flow speed u and an area perpendicular to the flow A_{\perp} , the ion current collected by a

Table 2.1: Important Langmuir probe geometry parameters.

d (cm)	θ (degree)	A_{\perp} (m ²)
1	26.565	1.953×10^{-6}
2	14.036	1.149×10^{-6}
3	9.462	0.842×10^{-6}
4	7.125	0.683×10^{-6}
5	5.711	0.587×10^{-6}

probe tip operating in ion saturation is:

$$i_{sat} = 0.61en_i \left(\frac{kT_e}{m_i} \right)^{1/2} + en_i u A_{\perp} \quad (2.19)$$

Solving Eq. 2.19 for the ion density gives:

$$n_i = \frac{V_{i3}/10 \Omega}{e0.61 \left(\frac{kT_e}{m_i} \right)^{1/2} + euA_{\perp}} \quad (2.20)$$

The area of the probe tip perpendicular to the flow is given approximately by:

$$A_{\perp} = \pi r_p^2 + \pi r_p h \sin(\theta) \quad (2.21)$$

In Eq. 2.21, r_p is the probe radius, h is the probe length, and θ is the angle that the probe tip is offset from the plume centerline. With a probe radius of 0.25 mm and a probe length of 5 mm, the values for the area perpendicular to plume from A_{\perp} and the offset angle θ are shown in Table 2.1.

2.6.2 Magnetized Plasmas

Complications arise in the analysis of probe signals when a magnetic field is applied to a plasma. The effect of the magnetic field on the motion of the ions and electrons must be considered. Ordering of probe radius, ion Larmor radius, and electron Larmor radius gives an indication of the effect of the field on Langmuir probe. First, in the weak field case, the Larmor radii of the ions and electrons are much greater than the probe dimensions. It is acceptable to use ordinary, unmagnetized, Langmuir probe theory in this case. The second case is that of the ion and electron Larmor radii much less than the probe dimensions. In this case, ions and electrons must diffuse to the probe to be collected. Hutchinson and Chen both discuss preliminary treatments of this case.[68, 66]

The third possible ordering is with the Larmor radius of the electrons much less than the probe diameter, which in turn is much less than the ion Larmor radius, $r_{Le} < L < r_{Li}$. In this case, the collection of ions by the probe is unaffected by the magnetic field. The equation derived earlier for the ion density in terms of V_{i3} is still correct. However, the collection of electrons is affected by the magnetic field. The electron current is reduced by the magnetic field from its field-free value, the equations used to estimate temperature from V_{12} must be reexamined.[66, 68, 69, 70] This correction will be developed in Chapter 5.

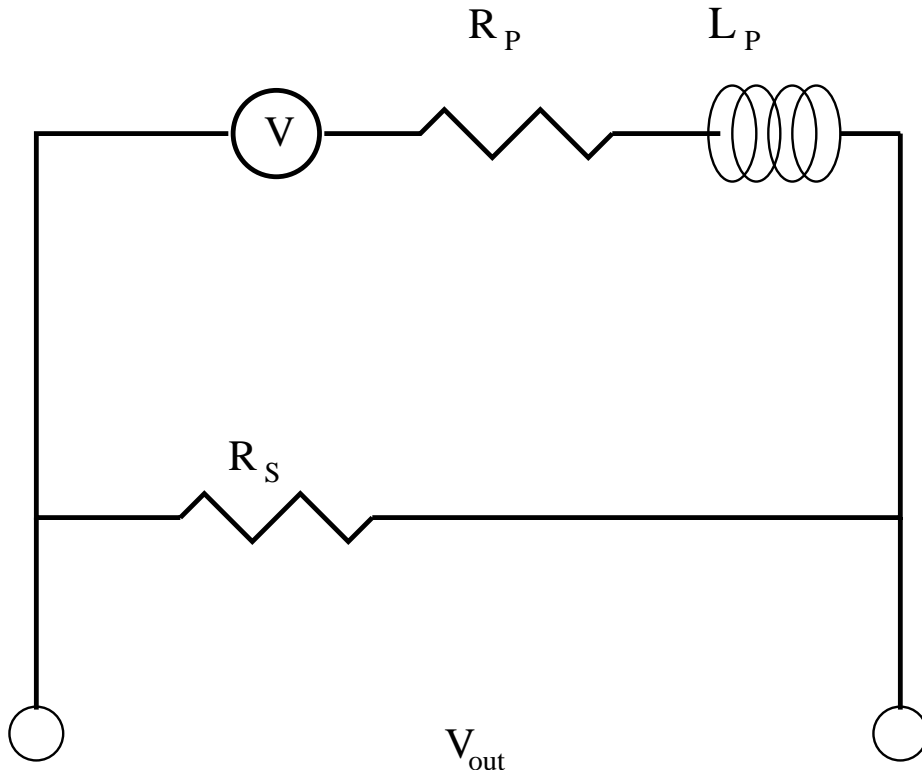


Figure 2.11: Circuit model for \dot{B} probe.

2.7 Magnetic Probes

Magnetic field data for the magnetized plume experiments are taken with a \dot{B} probe. This permits a quantitative description of the magnetic field as the laser ablation plasma expands and interacts with the strong field region under the magnets shown in Fig. 2.4. The probe is constructed from 100 turns of 36 AWG 8058 magnet wire manufactured by Belden Corporation. To form the probe, the magnet wire is wrapped around a 0.25 *in.* diameter plastic cylinder. The wire is held in place with vacuum epoxy cement. The probe is attached to the end of a small fiberglass rod with vacuum epoxy cement. This rod is secured in a foot long single bore alumina rod of the same type used to construct the Langmuir probe. At the opposite end of the alumina rod, the wire leads are attached to thick copper wire leads and vacuum sealed with vacuum epoxy cement. From the copper wire lead, the probe is connected to an RC integrator and then to the Hewlett Packard Infinium oscilloscope. The RC integrator has a time constant of 10^{-2} *s.* This RC value ensures correct and complete integration of the \dot{B} signal. It was found that the RC integrator reduced signal strength significantly. Thus, the probe was connected directly to the oscilloscope.

Figure 2.11 shows the circuit model of the \dot{B} probe system. Coil inductance, coil resistance, and scope impedance must be considered.[66, 71] Application of Kirchoff's current law permits the derivation of \dot{B} in terms of circuit parameters.

$$\dot{B} = \frac{1}{NA} \left(\frac{L_s}{R_s} \dot{V}_s + \left(1 + \frac{R_p}{R_s} \right) V_s \right) \quad (2.22)$$

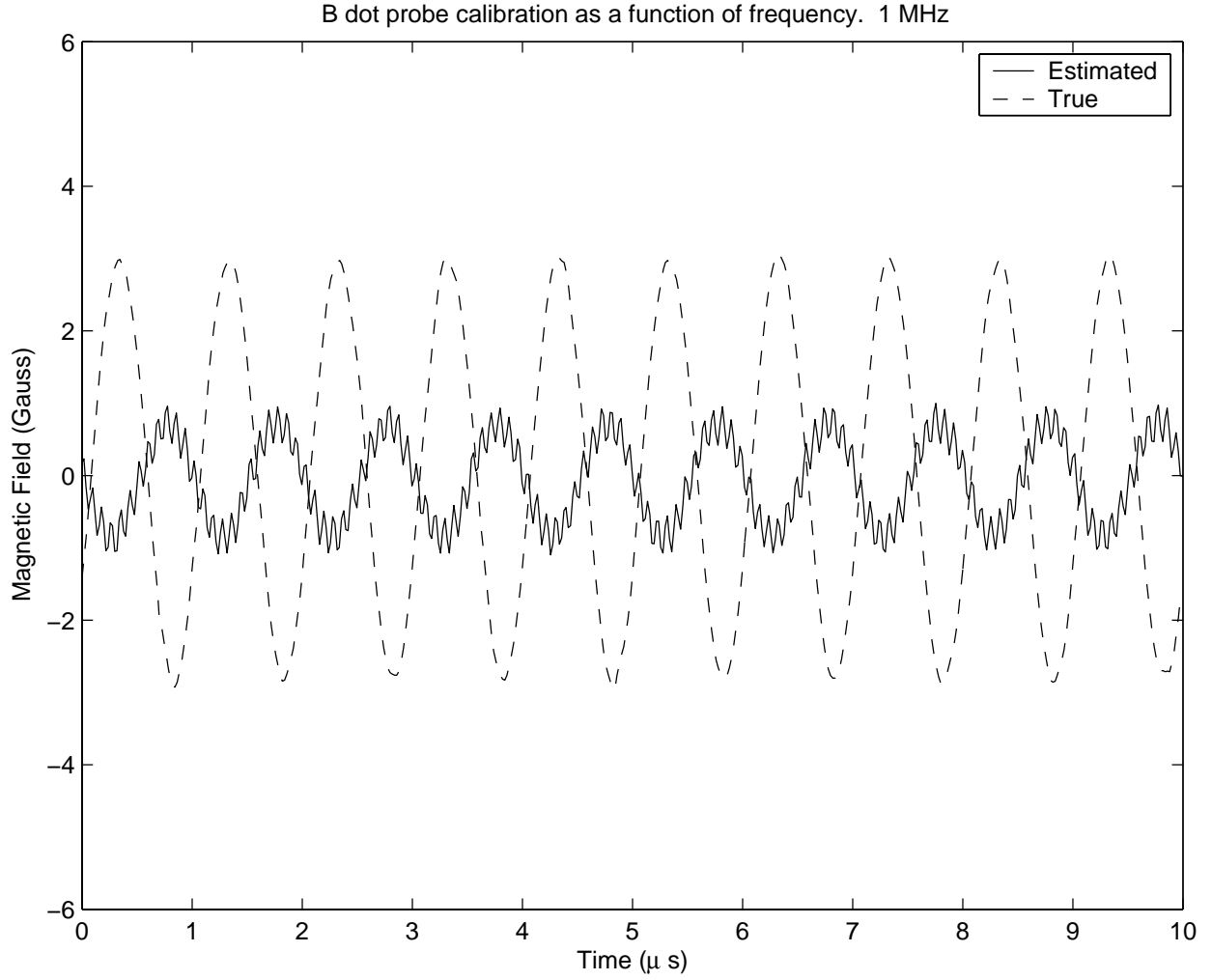


Figure 2.12: True magnetic field and magnetic field as detected by the \dot{B} coil.

In Eq. 2.22, N is the number of turns in the \dot{B} coil, A is the coil area, L_s is the \dot{B} coil inductance, R_p is the \dot{B} coil resistance, and R_s is the oscilloscope resistance. The probe resistance is 4.3Ω and the probe inductance is $66.7 \mu H$. The probe parameters was measured with a BK Precision 878 LCR meter.

Proper probe calibration is necessary to accurately determine the magnetic field. The magnetic field calculated by the \dot{B} probe may be different than the true field due to the effects of probe construction, such as multiple layers and loops not exactly perfectly looped around the former of the \dot{B} probe. To this, a simple coil is created by wrapping 25 turns of 36 AWG 8058 Belden magnet wire around a 6 *in.* diameter PVC tube. A small hole is drilled in the PVC tube to permit access for the \dot{B} probe. The \dot{B} probe is placed 1.4 *cm* from the center of the coil along the PVC tube centerline.

The magnetic field along the centerline of a dipole is:

$$B_{dip} = \frac{\mu_0 i R^2}{2(R^2 + z^2)} \quad (2.23)$$

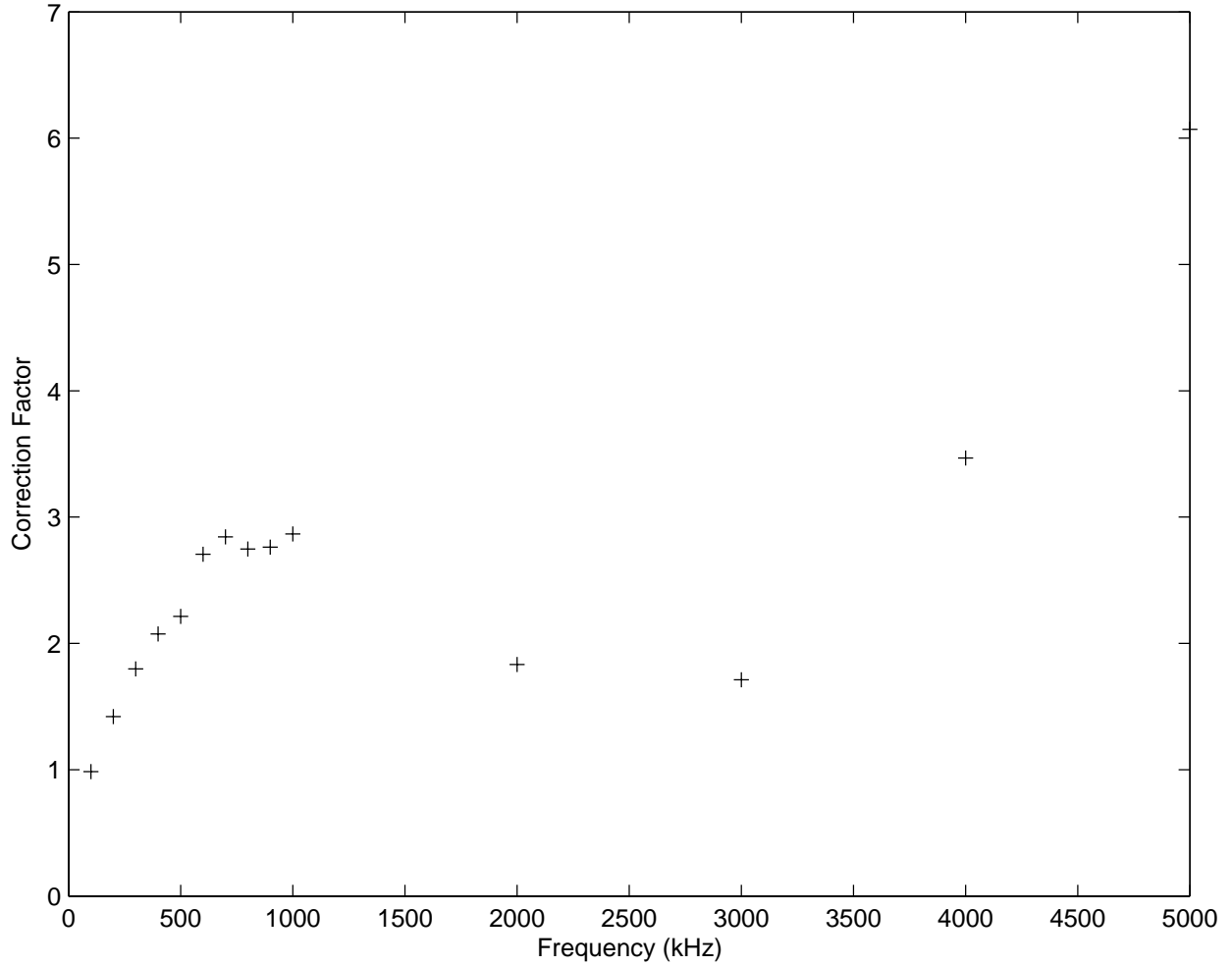


Figure 2.13: Correction factors for the \dot{B} probe as a function of frequency.

where μ_0 is the permeability of free space, R is the coil radius, z is the distance from the coil along the coil centerline, and i is the current in the coil. To account for the finite thickness of the coil by summing the contribution of the magnetic field from each loop of the coil. The coil thickness is 0.7 cm , and its center is 1.4 cm from the location of the \dot{B} probe. Thus, each loop of the coil is located at:

$$z_j = 1.4\text{ cm} - \frac{0.7\text{ cm}}{2} + j \times \frac{0.7\text{ cm}}{25} = 1.05\text{ cm} + j \times \frac{0.7\text{ cm}}{25} \quad (2.24)$$

The magnetic field due to all the current loops is the sum of the magnetic field from each individual loop. Thus, with Eqs. 2.23 and 2.24, the magnetic field is:

$$B = \frac{\mu_0 i R^2}{2} \sum_{j=0}^{24} \frac{1}{(R^2 + z_j^2)^{3/2}} \quad (2.25)$$

The magnetic field given by Eq. 2.25 is slightly different than multiplying Eq. 2.23 by the number of turns in the coil, 25.

A function generator is attached to the 25 turn coil and a 5.7Ω resistor to provide a known magnetic field. The current in the 25 coil is determined by the voltage drop across the 5.7Ω resistor. From the known field created by the 25 turn coil, and the magnetic field calculated from the \dot{B} coil, a correction factor for the construction of the probe is determined. Essentially, the correction factor is an effective NA value for the \dot{B} probe. The correction factor is found by dividing the true field, Eq. 2.25, by the observed field 2.22. In general, this factor may a function of the frequency. To determine the frequency response, the correction factor is determined over a frequency range between 100 kHz to 5 MHz . This correction factor is shown in Fig. 2.13.

In general, the correction factor is small, approximately only a factor of two over this frequency range. Thus, the raw magnetic fields from the \dot{B} probe will be multiplied by a factor of two to arrive at the true magnetic field. It should be noted that the function generator is not stable beyond a $1 - 2 \text{ MHz}$.

Data are taken using a setup similar to that shown in Fig. 2.8, although there is none of the circuitry used for the Langmuir probe experiments present. Magnetic field data are taken at positions of 1 cm , 2 cm , 3 cm , 4 cm , 5 cm . Three laser energies, 350 mJ , 440 mJ , and 550 mJ are used for comparison with the Langmuir probe and optical spectroscopy data. The Hewlett Packard Infinium Oscilloscope and the laser are both triggered by a Stanford Research Systems DG 535 trigger generator.

2.8 Mass Loss Measurements

In order to determine an ionization fraction and to investigate the energy balance within the plume, mass loss measurements are taken. A carbon target is initially weighed with a Mettler AE 240 microbalance. The target is ablated for a large number of pulses and then weighed again. This is repeated for 500 mJ , 450 mJ , 400 mJ , and 350 mJ . Unfortunately, the laser was not capable of pulses greater than 500 mJ due to the poor quality of the laser gas. From the mass loss measurements, the total number of atoms ablated is calculated. The pressure used was $1.0 \times 10^{-5} \text{ Torr}$. The pressure is sufficiently low such that there is no backscatter from the surrounding gas atoms.

Chapter 3

Laser Ablation Plume Plasma Physics

The properties of the plume created in pulsed laser ablation and deposition determine the characteristics of the deposited film. It is therefore vital that the properties of the plasma be well understood. Previous research performed with the experimental arrangement described in the Experimental chapter has characterized plasma plume parameters created from the laser ablation of carbon.[24] Electron temperature, ion density, the distribution of ion density in three dimensions, and ion kinetic energy were determined using a quadruple Langmuir probe. The key result from this work is the verification of adiabatic expansion.[24]

First, models of plume formation and expansion are reviewed. These models are then discussed in terms of empirically determined plasma data.[24] Second, the applicability of the quadruple Langmuir probe as a technique to determine plasma parameters is discussed. In the derivation of the Langmuir probe equations in the previous chapter, it has been assumed that the sheath surrounding the probe is collisionless. This will be verified using mass loss data from the current work and plasma parameter data determined from the previous work.[24] Third, an energy balance is conducted to determine the partition of the incident laser energy to the various plasma species. The energy balance is created using the mass-loss data conducted in the current work, with the plasma parameter data determined in the previous work.[24] Finally, the effects of sputtering and the potential for sheath formation at the substrate are considered.

3.1 Review of Models of Plume Behavior

3.1.1 Formation

A very simple view of the pulsed laser ablation process is as follows: 1) The incident laser rapidly heats the target. 2) A dense, warm plasma is created near the target surface 3) The plume expands adiabatically 4) The plume deposits onto a substrate, with the high particle kinetic energy permitting the creation of non-equilibrium structures(eg diamond-like carbon).

Before proceeding any farther, it is necessary to invoke an assumption. In this dissertation, the laser pulse duration is of the order of nanoseconds. Shorter pulse durations(ps and fs) permit different laser-target

interactions than those which occur in nanosecond pulses. In the nanosecond case, the dominant interaction is with the phonons in the material. This is because the laser time scale is greater than the time scale for transfer of energy from the electrons to the phonons. At shorter time scales, energy cannot be transferred from the electrons to the phonons. Discussion of laser-solid interaction for ps and shorter time scales may be found in literature.[72, 73]

At the beginning of the laser pulse the target material is heated rapidly and starts to evaporate. The neutral gas temperature is approximately equal to the temperature at which evaporation occurs. Using the Saha equation to estimate ion population underpredicts the ion population found experimentally.[26] An additional source of electrons is from thermoelectric emission.[26] The thermoelectric current density is found from Richardson's equation

$$J_e = AT^2 \exp\left(\frac{-\phi}{kT}\right) \quad (3.1)$$

where J_e is the current density, T is the target temperature, $A = 120 \frac{A}{cm^2 K^2}$ is Richardson's constant, and ϕ is the work function. For a carbon target, $\phi = 5eV$ and $T = 4073K$, $J_e \approx 1244 A/cm^2$. The temperature chosen is the evaporation temperature of diamond. Typical spot sizes are of the order of $0.2 cm^2$. In one nanosecond, approximately $1.16 * 10^{12}$ electrons are emitted. This represents a population of seed electrons which then gain energy via inverse bremsstrahlung, lose energy by ionizing surrounding atoms, which creates more electrons that may absorb photon energy. Inverse bremsstrahlung may also occur in the presence of neutral atoms. This process creates a plume with a higher ionization fraction than that which is predicted from the Saha theory.

In the process of inverse bremsstrahlung, an electron absorbs a photon in the presence of an ion. The laser absorption coefficient α is calculated by:[25]

$$\alpha = 3.69 \times 10^8 \frac{Z^3 n_i^2}{T^{1/2} \omega^3} \left(1 - e^{-h\omega/kT}\right) cm^{-1} \quad (3.2)$$

where Z is the charge state of the ions, n_i is the ion density in cm^{-3} , T is the electron temperature in eV and $\omega = 1.21 \times 10^{15} s^{-1}$ is the frequency of the laser radiation. For simplicity, $Z = 1$, although experimental results indicate the presence of multiply ionized species in most laser ablated plasmas. A detailed study of ion populations during the pulse would be helpful in determining an effective Z for certain elements. For a dense ($10^{23} m^{-3}$) warm ($\approx 100eV$) isothermal plasma, irradiated by a 248 nm laser, the mean free path for inverse bremsstrahlung is of the order of 4 millimeters. This is larger than the typical plume dimension in the direction normal to the target surface. Assuming a plume length of $100\mu m$ and pulse energy of $500 mJ$, the amount of energy absorbed via inverse bremsstrahlung is $12.3 mJ$, or about 2.5 percent of the incident laser energy. However, there is little experimental verification of the densities and temperatures found during plume formation.

A model for the electron population and temperature during the laser pulse may be derived by considering the source of electron production and loss, as well as electron heating and cooling. In terms of the electron population, production of electrons by thermoelectric and electron impact ionization are considered. For

simplicity, the only loss term considered is recombination. Electrons are heated by inverse bremsstrahlung and cooled by collisions with ions and neutral atoms. Adiabatic expansion is ignored for the short time scales. Dielectronic recombination is ignored.

The rate of thermoelectric production of electrons is found by modifying Richardson's equation, Eq.3.1:

$$\frac{dn_e}{dt}|_{therm} = \frac{120T^2 A e^{(\phi/kT)}}{1.6 * 10^{-19}} \frac{1}{A \Delta z} \quad (3.3)$$

Production of neutral atoms is derived from thermodynamics. The total number of neutral atoms emitted per laser pulse is:

$$N_n = \frac{E_l \rho N a}{M_w (\rho C_p \Delta T + \Delta H)} \quad (3.4)$$

To arrive at neutral atom density per second, Eq. 3.4 is divided by the product of the plume volume and the pulse duration.

$$\frac{dn_n}{dt}|_{evap} (cm^{-3} s^{-1}) = \frac{N_n}{A \Delta z \tau_{laser}} \quad (3.5)$$

The thickness, Δz is calculated via:

$$\Delta z = N_n A_s \frac{\rho N_A}{M_W} \quad (3.6)$$

Electron impact ionization from the ground state of neutral atoms and ions in the plume is assumed to have a rate constant S equal to:

$$S(Z) = 10^{-5} \frac{(T_e/E_i^z)^{1/2}}{(E_i^z)^{3/2} (6.0 + T_e/E_i^z)} \exp\left(-\frac{E_i^z}{T_e}\right) \quad (3.7)$$

The units of S are $cm^3 s^{-1}$

Radiative recombination from charge state z to charge state $z - 1$ occurs at a rate α equal to:

$$\alpha(Z) = 5.2 * 10^{-14} Z \left(\frac{E_i^z}{T_e}\right)^{(1/2)} \left(0.43 + 0.5 \ln\left(\frac{E_i^z}{T_e}\right) + 0.469 \left(\frac{E_i^z}{T_e}\right)^{-1/3}\right) \quad (3.8)$$

The units of α are also $cm^3 s^{-1}$.

With Eqs. 3.3 through 3.8 are used to describe the temporal behavior of the plume constituents. For this model ionization is not considered past C^{5+} . The population of the different constituents are given by the following rate equations:

Electrons:

$$\frac{dn_e}{dt} = \frac{dn_e}{dt}|_{therm} + \sum_{z=0}^4 S(z) n_e n_z - \sum_{z=1}^5 \alpha(z) n_e n_z \quad (3.9)$$

Neutral atoms:

$$\frac{dn_n}{dt} = \frac{dn_n}{dt}|_{evap} - S(z=0) n_e n_n + \alpha(z=1) n_e n_1 \quad (3.10)$$

Ions with $z=1$ to $z=4$:

$$\frac{dn_z}{dt} = S(z-1) n_e n_{z-1} + \alpha(z+1) n_e n_{z+1} - S(z) n_e n_z - \alpha(z) n_e n_z \quad (3.11)$$

Ions with charge state $z=5$:

$$\frac{dn_z}{dt} = S(4) n_e n_4 - \alpha(5) n_e n_5 \quad (3.12)$$

This set of equations can be solved using available first order differential equation solvers, such as those present in MATLAB. However, this does not completely describe the behavior of the plume. It is necessary to know the plume temperature, especially the electron temperature as a function of time. Assuming an isotropic pressure distribution, neglecting conduction to the target from the plasma volume, and an isothermal plume, the energy equation is:

$$\frac{3}{2}n \frac{dT}{dt} = \sum Q \quad (3.13)$$

for each species present in the plume.

In this model, energy is added directly to the electrons by inverse bremsstrahlung. In the presence of an electric field, either from ions or neutral atoms, electrons gain energy from the incident photons. Inverse bremsstrahlung in the presence of ions is typically dominant over inverse bremsstrahlung (IB) mediated by neutral atoms. Thus, only ion IB is considered. The electric field of the electromagnetic wave incident upon the plasma causes ordered electron motion. Electron-electron collisions then distribute this ordered motion in thermal energy. The rate of energy input to electrons is approximately proportional to the electron-ion collision frequency (since IB is an electron - ion process) multiplied by the energy of the ordered motion. The rate at which directed energy is converted into thermal energy is proportional to the electron-electron collision frequency and the thermal speed.

$$E_{IB} \approx \frac{m_e v_{os}^2 \nu_{ei}}{2} \quad (3.14)$$

with

$$v_{os} = \frac{eE}{m_e \omega_0} \quad (3.15)$$

and

$$E_{therm} \approx \frac{m_e v_{th,e}^2 \nu_{ee}}{2} \quad (3.16)$$

If the rate of energy input from inverse bremsstrahlung is much less than the rate at which ordered energy is converted into thermal energy, then the electron distribution function may be assumed to be Maxwellian.

$$\frac{v_{os}^2 \nu_{ei}}{v_{th,e}^2 \nu_{ee}} \ll 1 \quad (3.17)$$

Given the laser intensities and particle densities common in these laser produced plasmas, the condition in Eq. 3.17 is easily met.

For simplicity, it is assumed that the rate at which energy is transferred to the plume via inverse bremsstrahlung is:

$$Q_{IB} = \frac{P_0}{V} (1 - \exp(-\alpha z)) \quad (3.18)$$

with α defined in Eq. 3.2, V is the plume volume, and z is the plume dimension. Q_{IB} is summed over all ions, since α is dependent on ion density and Z .

The plasma is assumed to be in local thermodynamic equilibrium during the initial stages of formation.[26] Thus, it should radiate as a black body. The rate of energy loss is given by $A\sigma T^4$. Although a black body

only radiates from its surface, the rate of loss per unit volume is:

$$Q_B \approx \frac{A\sigma T^4}{V} \quad (3.19)$$

where T is in units of *Kelvin*, σ is the Stefan-Boltzmann constant, A is the spot area, ignoring the small plume thickness, and V is the plume volume. This assumes that heat conduction is rapid so that any losses of energy at the surface are conducted throughout the volume on a time scale much less than the laser pulse time. Furthermore, Eq. 3.19 assumes that the plasma emits as a perfect black body. This is not necessarily true for plasmas. The Stefan-Boltzmann constant in Eq. 3.19 is multiplied by the emissivity ϵ which is less than one. The value of the emissivity for the plasma in the initial stages of plume development is unknown, and for simplicity the perfect black-body assumption, $\epsilon = 1$, is made.

Ionization by electron impact is another process by which the electron population loses energy. The rate of energy loss by ionization is calculated from the ionization rate S defined in Eq. 3.7.

$$Q_{ion} = n_i n_e S E_i \quad (3.20)$$

where E_i is the ionization energy. Equation 3.20 is summed over all ionization states present.

Elastic collisions between all types of particles act to bring the different plume constituents into thermodynamic equilibrium. Energy exchange between two arbitrary, unlike particles in the plume is given by:

$$Q_{ab} = n_a \sum_b \nu_{ab} (T_b - T_a) \quad (3.21)$$

In Eq. 3.21, the collision frequency for energy transfer (the inverse of the energy equipartition time) is given by:

$$\nu_{ab} = \frac{(m_a m_b)^{1/2} Z_a^2 Z_b^2 n_b \ln \Lambda}{(m_a T_b + m_b T_a)^{3/2}} \quad (3.22)$$

Thus, the energy equations for electrons and heavy particles are, respectively:

$$\frac{3}{2} n_e \frac{dT_e}{dt} = Q_{eb} + \sum_{z=1}^5 \frac{P_0}{V} (1 - \exp(-\alpha_z \delta)) - \sum_{z=0}^4 n(z) n_e S E_i(z) - \frac{A\sigma T^4}{V} \quad (3.23)$$

where $n(z)$ is the number density of charge state z , α_z is the inverse bremsstrahlung coefficient calculated for charge state z , δ is the plume extent, and P_0 is the initial power.

$$\frac{3}{2} n(z) \frac{dT_z}{dt} = Q_{zb} \quad (3.24)$$

where $n(z)$ is the number density of charge state z , and T_z is the temperature of charge state z .

A code is written to solve the equations for density and temperature. It is iterated until convergence on the maximum electron temperature. Results are shown for a laser energy of 550 *mJ* in Fig. 3.1. The code determines an electron temperature of about 1 *eV*, with neutral atoms the dominant constituent. Ion density is $\approx 10^{20} m^{-3}$. The neutral atom density was $\approx 10^{23} cm^3$, two orders of magnitude larger than the

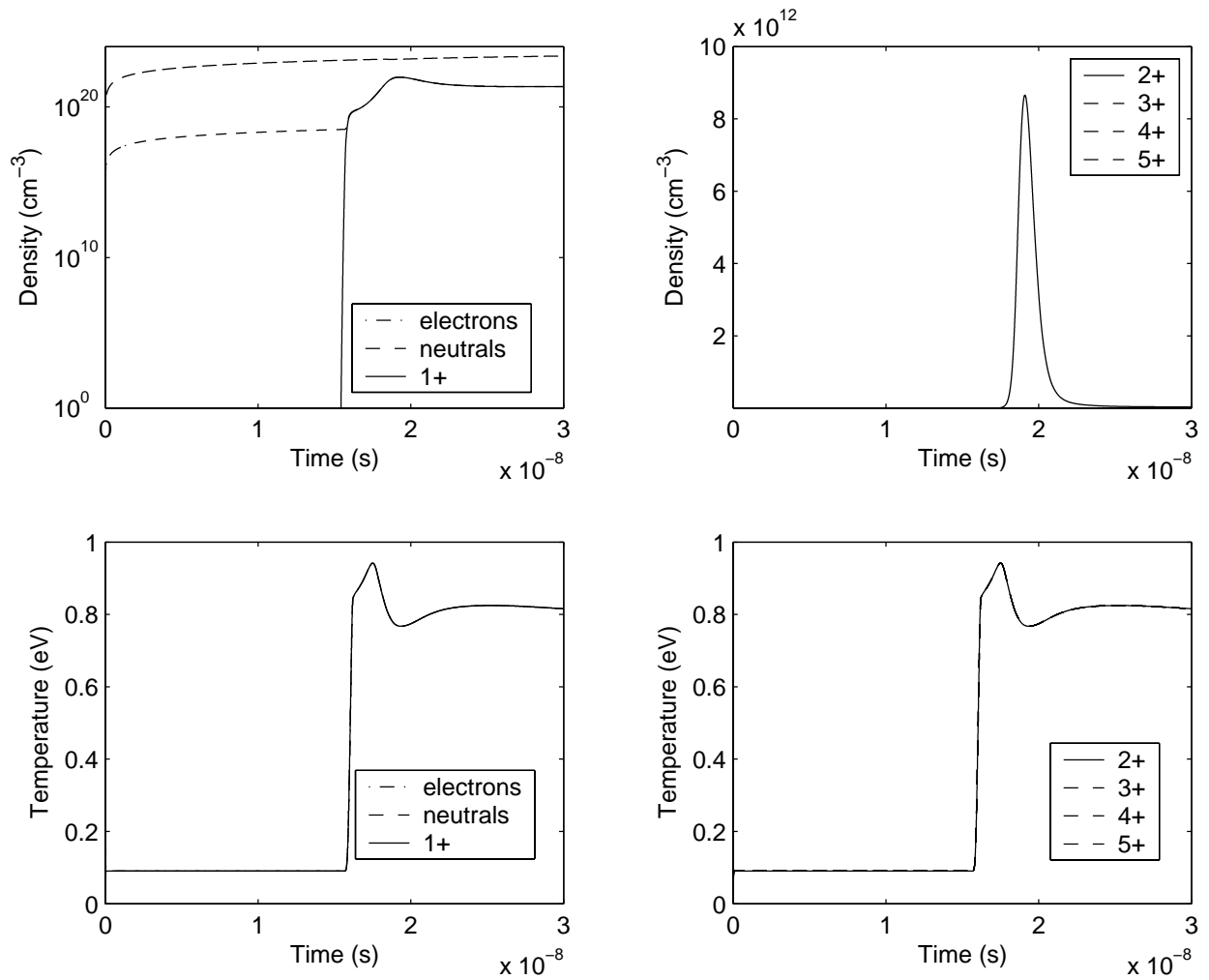


Figure 3.1: Results of a simple zero dimensional, time dependant code for the formation of the plasma plume.

typical values.[26] This is due to the fact that the plume thickness was taken to be the thickness of ablated materials. Given that the material should expand from phase transformation (*solid* \rightarrow *vapor* \rightarrow *plasma*), the actual plume thickness should be larger. Singh and Narayan indicate that the expected plume thickness is 10 – 100 μm at the end of a 30 ns laser pulse.[26] If the plume thickness were increased, in this model, the density would decrease. A decrease in density would reduce the energy transfer rate between electrons and other species. This would enable electrons to reach larger temperatures, permitting larger quantities of ions.

The results of the zero dimensional model also show that the plume is in local thermodynamic equilibrium. Collision frequencies are sufficiently large between species that energy is transferred and equilibrated rapidly between species. Another interesting result is that the increase of electron temperature is delayed. This is due to the fact that the electron density must reach a certain density before energy gain by inverse bremsstrahlung overcomes losses to other species. The electron temperatures calculated are too low, as

experiments have shown the presence of C^{2+} and higher ionization states, whereas in this model C^{2+} is produced only briefly.[74, 38, 75] Furthermore, experimental results show that the electron temperature at 1 cm from the target surface are ≈ 10 eV. The model ignores the effects of inverse bremsstrahlung in the presence of neutral atoms, which will heat the electrons. If the emissivity of the plasma is less than one, then the energy loss by black-body radiation is too large. Thus, if the plasma does not emit as a perfect black-body, then the temperature of the plasma during formation will be larger than that determined by the code.

Experimental results on plume properties during the laser pulse are lacking. The plume is generally considered to be isothermal, due to the high densities present. For this to be strictly valid, the longest equipartition time for energy transfer between unlike constituents must be much less than the laser pulse time. This is shown in the results of the model. Gated optical spectroscopy is probably the most useful experimental technique for determining species density and temperature during the laser pulse. Langmuir probe techniques are difficult, if not impossible, due to the small plume dimensions, high densities and temperatures, and possibility of being destroyed by the laser.

3.1.2 Expansion

Several authors have investigated the expansion of the plasma plume once it has been created. The first of these models are adiabatic expansion models. Next, a number of authors used the fluid equations for a neutral fluid to determine the behavior of expanding plumes. However, these neglect the effects of electrons and ions. Recently, authors have used the fluid equations for plasmas to describe expansion, as well as kinetic theory, in the form of the Vlasov equation. These models confirm the basic physics of the expansion of plasma plumes, in that the expansion proceeds adiabatically.[36] They contain new physics not found in standard adiabatic expansion models which do not consider the interaction of electrons and ions within the plume. Ion acceleration is dependent on the electron distribution function, as electrons with their small mass will attempt to escape the plume first, accelerating the ions due to space charge effects.[33] The ion velocity can then be larger than that due to purely hydrodynamic acceleration alone. However, most of the basic physics is found in the standard adiabatic expansion models and they are discussed below.

A simple model for the unrestricted expansion of a spherical gas cloud in to vacuum is given by Zeldovich.[25] In this model, adiabatic expansion is implicitly assumed. The initial thermal energy of the plasma is converted in to the kinetic energy of motion. The leading edge flow speed of the plume is determined by the ratio of specific heats, γ , and the root mean square speed of the particles within the plume, u_∞ .

$$u_{edge} = \left(\frac{2\gamma}{\gamma - 1} \right)^{1/2} u_\infty \quad (3.25)$$

u_∞ is the root mean square flow speed given by:

$$u_\infty = \left(\frac{2E_0}{M_i} \right)^{1/2} \quad (3.26)$$

where E_0 is the initial temperature of the plume, and M_i is the ion mass in the plume.

Singh and Narayan derive a more specific adiabatic expansion model for the specific case of laser ablation.[26] The fundamental process of adiabatic expansion, the conversion of thermal energy to the kinetic energy of flow is evident in the computational results of their model. This process was confirmed experimentally.[76, 24]

With the adiabatic expansion models, the initial plume temperature may be estimated. For a laser energy density of $2.0 J/cm^2$, the flow speed is $u = 4.9 \times 10^{-4} m/s$. Taking this speed to be the leading edge flow speed, given by Eqs. 3.25 and 3.26, an estimate of the initial temperature is expressed as:

$$E_0 = u_{edge}^2 \frac{\gamma - 1}{2\gamma} \frac{M_i}{2} \quad (3.27)$$

With $u_{edge} = 4.9 \times 10^{-4} m/s$, $M_i = 12 \cdot 1.66 \times 10^{-27}$, and the ratio of specific heats, $\gamma \approx 1.2$, [26] the initial plume temperature is $E_0 \approx 12.45 eV$. Unfortunately, there is little experimental work on calculation of plume parameters during the plume formation stage. Recent work by Harilal, et al, based on time integrated data, assuming local thermodynamic equilibrium(LTE), estimates electron temperatures three mm from the target of $2 eV$. [77] While LTE may be valid during the initial stage of plume formation, there is no a priori reason to suggest that it is valid at later times. Furthermore, the fact that the spectra are time integrated over the plume lifetime means that the estimated electron temperatures are a time average. They observed the presence of C^{2+} and C^{3+} ions. [77] This suggests an electron temperature between $10 eV$ and $30 eV$ or higher, as the ionization potential of C^{2+} is $24.381 eV$ and the ionization potential of C^{3+} is $47.881 eV$.

The electron temperature estimated in Eq. 3.27 is within the error of of the electron temperature $1 cm$ from the target at the same laser energy density and spot size and greater than that suggested by the simple plume formation model. This would suggest that electrons are expanding isothermally, $\gamma = 1$, and that their density only changes due to the increased volume of the plasma. However, the previous work indicates that there is electron cooling between the 1, 3, and 5 cm Langmuir probe positions. [78] The adiabatic expansion coefficient is given as $\gamma = 1.2$ in Singh and Narayan's model. [26] The adiabatic expansion coefficient can be calculated from density and temperature data from the previous research. The adiabatic expansion law is:

$$\frac{d}{dt} \left(\frac{P}{\rho^\gamma} \right) = 0 \quad (3.28)$$

Thus:

$$\frac{P}{\rho^\gamma} = C \quad (3.29)$$

where C is an arbitrary constant. Since $\rho = Mn$, where M is the ion mass and n is the density, the ion mass M can be combined with the arbitrary constant C . The pressure is related to the temperature and density by $P = nkT$, therefore:

$$kT = Cn^{\gamma-1} \quad (3.30)$$

Taking the natural log of Eq. 3.30 results in:

$$\ln(kT) = \ln(C) + (\gamma - 1) \ln(n) \quad (3.31)$$

Table 3.1: Adiabatic expansion coefficients and estimated electron temperatures as a function of laser energy density.

E_l (J/cm^2)	u (m/s)	γ	T_0 (eV)
1.6	41705	1.5049	18.16
2.0	49011	1.5309	25.93
2.5	56192	1.5617	35.35
3.2	67295	1.6149	53.67

As temperature and density are known at three different positions, 1 *cm*, 3 *cm* and 5 *cm* from the target, pairs of $\ln(n)$, $\ln(kT)$ can be graphed and the slope of the line connecting these points is equal to $\gamma-1$. Table 3.1 shows the results of this analysis. The adiabatic expansion coefficients derived from Eq. 3.31 are larger than those suggested by Singh and Narayan, and are close to the expected adiabatic expansion coefficient for an ideal gas, $\gamma = 5/3$. With the calculated adiabatic expansion coefficients, initial temperatures are estimated from Eq. 3.27 and shown in Table 3.1. These electron temperatures are reasonable given the presence of C^{2+} and C^{3+} ions which have been observed in the plumes arising from the laser ablation of carbon.[74, 77] Another means of estimating initial plume temperature can be derived from kinetic theory. This requires a true time-of-flight signal. However, the treatment of the Langmuir probe signal as a true time of flight signal must be investigated.

3.2 Langmuir Probes

The applicability of the Langmuir probe as a means of acquiring both time-of-flight(TOF) signals and direct electron temperature and ion density data is investigated in this section. Time of flight signals have the following defining characteristic: there exists a one-to-one correspondence between the arrival time of a signal and ion speed. Probe size, collisions, and external forces may destroy this correspondence. The effects of these factors on the TOF assumption are investigated. Mean free paths are calculated to investigate the implicit assumption of a collisionless sheath surrounding the Langmuir probe in the Langmuir probe equations derived in the Experimental chapter. The mean free path for collisions must be much greater than the Debye length for the collisionless sheath assumption to be accurate.

3.2.1 Forces

A further condition on the applicability of the time-of-flight assumption is that there are no net forces. If the plasma experiences an acceleration, it cannot be guaranteed that the distribution of ion velocities that the detector records is identical to the velocity distribution of ions at the source. Once the plasma has expanded to the point at which collisions are negligible, external forces are the only means of altering the distribution function. The analytic work of Mora,[35] and of Kovalev and Bychenkov,[33] predicts the

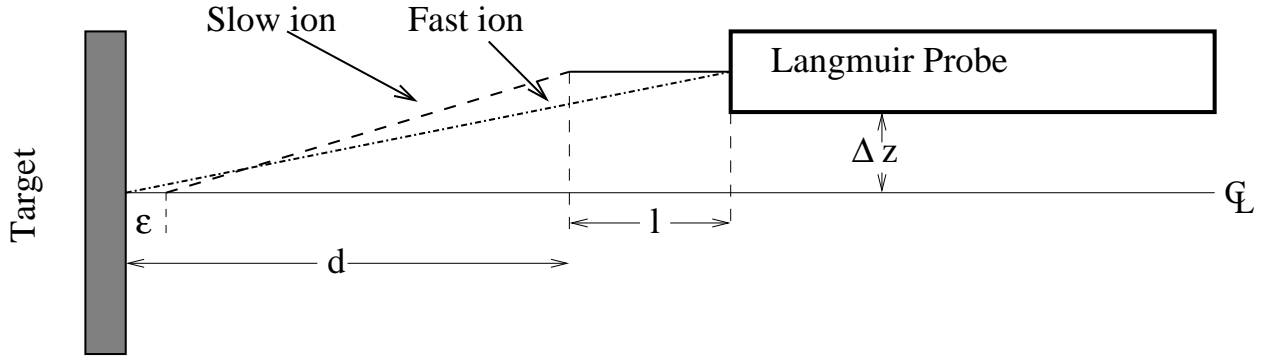


Figure 3.2: Geometry of Langmuir probe for time-of-flight analysis.

presence of an electric field which accelerates the ions. The predicted electric field decreases rapidly in time. This electric field acts to alter the differential ion energy distribution, $\frac{dN}{dE}$ from that predicted from a Maxwellian distribution alone. Mora shows that the electric field is only present at the edge of the expanding plasma and that the field at the front decreases as $\omega_{pi}^{-2}t^{-2}$, where ω_{pi} is the initial ion-plasma frequency. Given the large initial densities, the ion plasma frequency will be very large, $\approx 10^{12} \text{ Hz}$. Thus, the electric field is negligible even after a few nanoseconds and cannot perform any velocity space mixing to invalidate a time-of-flight measurement.

3.2.2 Finite Probe Size

It may not be possible to neglect the size of the probe. For this discussion, the probe is considered to be that region over which charges are collected. As discussed in the Experimental chapter, the Langmuir probe used in these experiments has a tungsten wire tip 5 mm long. Consider a Langmuir probe with the geometry shown in Fig. 3.2. The probe has length l , distance from tip to target d , and offset from centerline Δz .

A fast ion may arrive at the far end of the probe at the same time as a slow ion reaches the tip of the probe. Let this be time τ . The speed of the fast and slow ions are, respectively:

$$v_1 = \frac{\alpha_1}{\tau} \quad (3.32)$$

$$v_2 = \frac{\alpha_2}{\tau} \quad (3.33)$$

The total distance of ion travel to the tip, α_1 , and the total distance of ion travel to the far end of the probe, α_2 are determined by simple geometry:

$$\alpha_1 = (d^2 + \Delta z^2)^{1/2} \quad (3.34)$$

$$\alpha_2 = \left((d+l)^2 + \Delta z^2 \right)^{1/2} \quad (3.35)$$

Table 3.2: Applicability of time-of-flight assumption at different Langmuir probe positions.

<i>Posn. (cm)</i>	δ	K_1 (eV)	K_2 (eV)
1	1	100	200
2	0.529	100	152.9
3	0.351	100	135.1
4	0.262	100	126.2
5	0.208	100	120.8

With Eqs. 3.32, 3.33, 3.34, and α_2 , the kinetic energies of the ions which arrive at the tip and the far end of the Langmuir probe at the same time, τ , are:

$$K_1 = \frac{m_i}{2\tau^2} (d^2 + \Delta z^2) \quad (3.36)$$

$$K_2 = \frac{m_i}{2\tau^2} \left((d+l)^2 + \Delta z^2 \right) \quad (3.37)$$

Therefore, the range of ion kinetic energies that are detected by the Langmuir probe at time τ is:

$$\Delta K = K_2 - K_1 = \frac{m_i}{2\tau^2} (l^2 + 2dl) \quad (3.38)$$

If the time-of-flight assumption is valid, then the energy range which the probe detects at a single time must be small. A dimensionless measure of the applicability of the time of flight assumption is derived by dividing the energy range ΔK by the slowest ion speed K_1 .

$$\delta = \frac{(l^2 + 2dl)}{d^2 + \Delta z^2} \quad (3.39)$$

If δ is small, then the energy spread detected by the Langmuir probe is smaller than a representative ion kinetic energy. The use of the slow ion kinetic energy K_1 yields the most conservative measure of the applicability of the TOF assumption. As the probe is placed farther from the target, or the probe length becomes smaller, the validity of the TOF assumption improves. However, near the target, the assumption is poor. Consider the 1 cm probe position ($d = 1$ cm). The Langmuir probe is has an offset $\Delta z = 0.5$ cm and a probe length $l = 0.5$ cm.

$$\delta = \frac{(0.5 \text{ cm})^2 + 2 \times 1 \text{ cm} \times 0.5 \text{ cm}}{(1 \text{ cm})^2 + (0.5 \text{ cm})^2} = 1 \quad (3.40)$$

Under these conditions, an ion with a kinetic energy of 100 eV reaches the probe tip at the same time as an ion with a kinetic energy of 200 eV reaches the far end of the probe. Table 3.2 shows values of δ for typical Langmuir probe positions as well as values of K_2 for a representative K_1 of 100eV. At the 1 cm Langmuir probe position, the time of flight assumption is not applicable.

It is therefore advantageous to use a small probe far from the target to collect time-of-flight information. However, this must be balanced against reductions in the signal-to-noise ratio. Given the dimensions of the probe in the current experimental setup, interpretation of Langmuir probe results as time-of-flight is inaccurate.

3.2.3 Collisions

For the time-of-flight assumption to be valid, the plume must expand at the end of the laser pulse as an effusive source. That is, there are not events, such as collisions, that will alter the one-to-one correspondence between arrival time and ion kinetic energy. Essentially, collisions may not occur after expansion.

The point at which collisions may be neglected occurs when the collision mean free path for a particular particle is greater than the plume dimensions. For ions and neutral atoms, collisions with electrons are neglected as these collisions are inefficient at changing the speed of the colliding ion or neutral atom. Ion-ion, ion-neutral, and neutral-neutral collisions are considered for the heavy particles. Electron-electron, electron-ion, and electron-neutral collisions are considered for electrons. The ion-neutral and neutral-neutral, and electron-neutral mean free paths are taken to be identical:

$$\lambda_{in} = \lambda_{en} = \lambda_{nn} = \frac{1}{n_n \sigma_n} \approx \frac{1}{2/3\pi R^2 n_n} \approx 8.05 \times 10^{19} \frac{1}{n_n} m \quad (3.41)$$

In Eq. 3.41, λ_{in} is the ion-neutral collision mean free path, λ_{en} is the electron-neutral collision mean free path, λ_{nn} is the neutral-neutral collision mean free path, n_n is the neutral atom density, σ_n is the neutral atom collision cross section, and R is the atomic radius of carbon, 0.77 \AA . For charged particle collisions, the mean free path is approximated by:[79, 47]

$$\lambda_{kl} = \frac{v_{th,k}}{\nu_{kl}} \quad (3.42)$$

In Eq. 3.42, λ_{kl} the the mean free path for collisions of particles of type k with particles of type l , $v_{th,k}$ is the thermal speed of particle of type k , and ν_{kl} is the frequency for collisions of particles of type k with those of type l . The collision frequencies are given by the following formulae:

$$\nu_{ei} = \frac{2^{1/2} n_i Z^2 e^4 \ln \Lambda}{12\pi^{3/2} \epsilon_0^2 m_e^{1/2} T_e^{3/2}} \quad (3.43)$$

$$\nu_{ee} = \frac{n_i Z^2 e^4 \ln \Lambda}{\epsilon_0^2 m_e^{1/2} T_e^{3/2}} \quad (3.44)$$

$$\nu_{ii} = \frac{n_i Z^4 e^4 \ln \Lambda}{12\pi^{3/2} \epsilon_0^2 m_i^{1/2} T_i^{3/2}} \quad (3.45)$$

With the appropriate thermal speeds, and Eqs. 3.43, 3.44, 3.45 and constants, the mean free paths become:

$$\lambda_{ei} = \left(\frac{kT_e}{m_e} \right)^{1/2} \frac{12\pi^{3/2} \epsilon_0^2 m_e^{1/2} T_e^{3/2}}{2^{1/2} n_i Z^2 e^4 \ln \Lambda} \approx 1.45 \times 10^{17} \frac{T_{e,eV}^2}{n_i Z^2 \ln(\Lambda)} m \quad (3.46)$$

Table 3.3: Electron-electron mean free path as a function of laser energy at the 1 *cm* Langmuir probe position.

<i>Laser Energy</i> (mJ)	n_e (m^3)	Λ	λ_D (μm)	λ_{ee} (μm)
350	5.933×10^{19}	11.08	3.071	403.6
440	7.231×10^{19}	11.06	2.856	397.8
550	8.529×10^{19}	11.05	2.696	386.7
700	1.048×10^{20}	11.05	2.520	365.6

$$\lambda_{ee} = \left(\frac{kT_e}{m_e} \right)^{1/2} \frac{\epsilon_0^2 m_e^{1/2} T_e^{3/2}}{n_e Z^2 e^4 l n \Lambda} \approx 3.06 \times 10^{15} \frac{T_{e,eV}^2}{n_e Z^2 l n(\Lambda)} m \quad (3.47)$$

$$\lambda_{ii} = \left(\frac{kT_i}{m_i} \right)^{1/2} \frac{12\pi^{3/2} \epsilon_0^2 m_i^{1/2} T_i^{3/2}}{n_i Z^4 e^4 l n \Lambda} \approx 1.45 \times 10^{17} \frac{T_{i,eV}^2}{n_i Z^2 l n(\Lambda)} m \quad (3.48)$$

First, consider the electrons. As stated previously, if electrons undergo collisions, then any one-to-one correspondence between arrival time and electron speed is destroyed. The electron-electron mean free path is quite small, as shown in Table 3.3. The debye length, λ_D is included for comparison. as shown in Table 3.3, the electron-electron collision mean free path is much greater than the Langmuir probe position, 1 *cm*, for this case. Any electron in the plasma which at some point is collected by the probe must undergo several collisions before it reaches the probe. This means that any one-to-one correspondence between velocity and time of arrival for electrons is destroyed. Electron signals from Langmuir probes cannot be considered a true time-of-flight signal.

The electron-electron mean free path is much greater than the Debye length. From Eqs. 3.48 and 3.46, the mean free path for electron-ion and ion-ion collisions are greater than the electron-electron collisions mean free path. For collisions with neutral atoms, the mean free paths are larger than those for charged particle collisions, given the neutral atom density. The neutral atom density will be discussed with the mass loss results. The assumption of the collisionless sheath is therefore valid for these experimental conditions.

The electron-ion and ion-ion mean free paths at the conditions described in the electron-electron collision mean free path analysis are in the range 1.7 *cm* to 1.9 *cm*. The mean free path for collisions with neutral atoms are in the range 4.4 *cm* to 12 *cm*. Under these conditions, one could consider ion and neutral atom signals to be a true time-of-flight signal. It is important to know the position at which the transition between collisional interactions and free flight begins. This will give the plume a finite thickness that must be accounted for in the same manner as finite Langmuir probe length effects. There does not exist detailed information in this experiment on plasma densities or electron temperatures at positions closer to the target than 1 *cm*. Figure 3.3 shows values of the electron-ion mean free path as a function of density for a range of temperatures. The electron-ion mean free path is identical to the ion-ion mean free path under the assumption that electron temperature and ion temperature are identical.

Table 3.4: Applicability of time-of-flight assumption at different Langmuir probe positions accounting for a finite plume thickness.

<i>Posn. (cm)</i>	δ	K_1 (eV)	K_2 (eV)
1	1.358	100	235.8
2	0.684	100	168.4
3	0.443	100	144.3
4	0.326	100	132.6
5	0.257	100	125.7

The density at a particular position may be estimated by assuming an inverse-square relationship. For instance, the density at the position r is equal to $n_0 r_0^2 / r^2$ where n_0 is the density at reference position r_0 . The density at $r = 1$ mm at a laser energy of 700 mJ is therefore $\approx 1.048 \times 10^{22} m^{-3}$. The ion-ion mean free path for an electron temperature of 10 eV at that density is ≈ 0.16 mm. If the electron temperature is somewhat higher, 20 eV, then the mean free path increases to ≈ 0.5 mm. At lower laser energies, the ion-ion mean free path will be larger than in the 700 mJ case, due to their reduced densities. This will make the ion-ion mean free path equal or exceed the assumed 1 mm plume extent assumed in this example. Although the exact values of density and temperature are not known here, Fig. 3.3 with an inverse square assumption for the density variation shows that the plume extent where ion-ion collisions may be neglected is no greater than 1 mm. At 0.1 mm, the density for a laser energy of 700 mJ is $1.048 \times 10^{24} m^{-3}$. For an electron temperature of 30 eV, reasonable, since this position and density represents an earlier time frame in the evolution of the plume, the mean free path is 0.016 mm. Thus, ion-ion collisions are still likely to occur at these small plume extents. As the plume expands, ion-ion collisions may be neglected once the plume has reached ≈ 1 mm in extent. If a finite plume extent, ϵ , is accounted for, then Eq. 3.39

$$\delta = \frac{(l^2 + 2dl + 2d\epsilon - \epsilon^2)}{(d - \epsilon)^2 + \Delta z^2} \quad (3.49)$$

This will alter the results of Table 3.2. Table 3.4 below shows the applicability of the time of flight assumption to different Langmuir probe position. The effects of finite plume thickness act to decrease the accuracy of a time-of-flight measurement, even if the thickness is only 1 mm.

3.2.4 Estimation of T_i assuming time of flight

It is possible to estimate the initial temperature using an approach from kinetic theory.[80] Assume that the velocities are given by

$$v_i(t) = \frac{l}{t - \tau_0} \quad (3.50)$$

where v_i is the ion velocity, and τ_0 is the laser time that the laser pulse occurs. The laser pulse time is determine with a laser energy meter connected to a Hewlett Packard Infinium oscilloscope. Thus, the ion

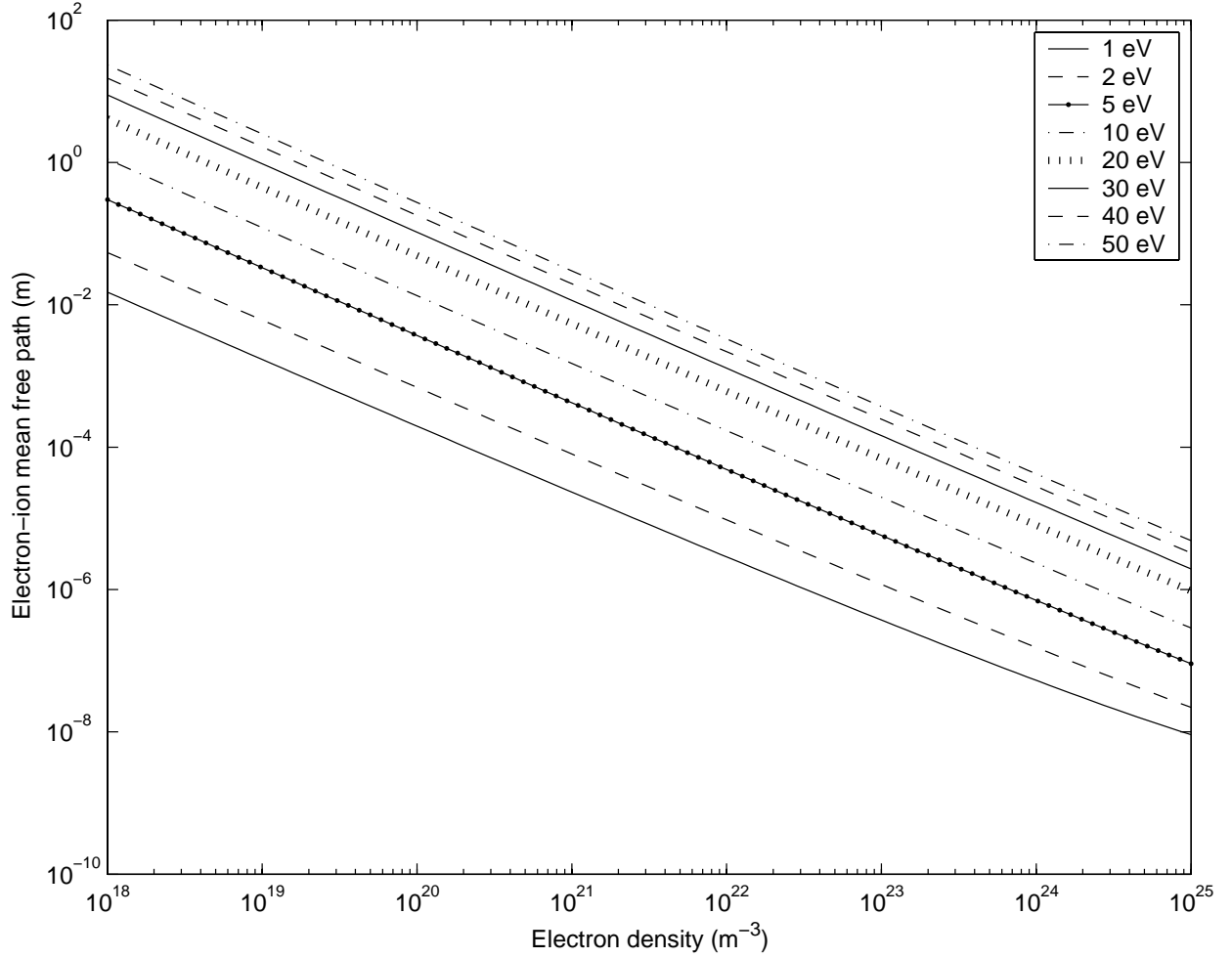


Figure 3.3: Electron-ion mean free path as a function of electron density at different electron temperatures. These mean free paths are identical to the ion-ion mean free path under the assumption that electron and ion temperatures are identical.

energy is calculated using Eq. 3.50:

$$E_i(t) = \frac{m_i l^2}{2(t - \tau_0)^2} \quad (3.51)$$

Mayo in Ref. [80] expresses conservation of number of particles as:

$$\left(\frac{dN}{d\Omega dE} \right) \delta\Omega dE = \frac{I}{e} dt \quad (3.52)$$

In Eq. 3.52, $d\Omega$ is the differential solid angle, dE is the differential ion kinetic energy, dN is the differential number of particles, I is the ion current, e is the electron charge, and $\delta\Omega$ is the differential solid angle swept by the detector. Physically, $\frac{dN}{d\Omega dE}$ is the differential number of ions per energy per solid angle. For simplicity, the angular dependence is ignored. Equation 3.52 becomes

$$\frac{dN}{dE} = \frac{I}{e} \frac{dt}{dE} \quad (3.53)$$

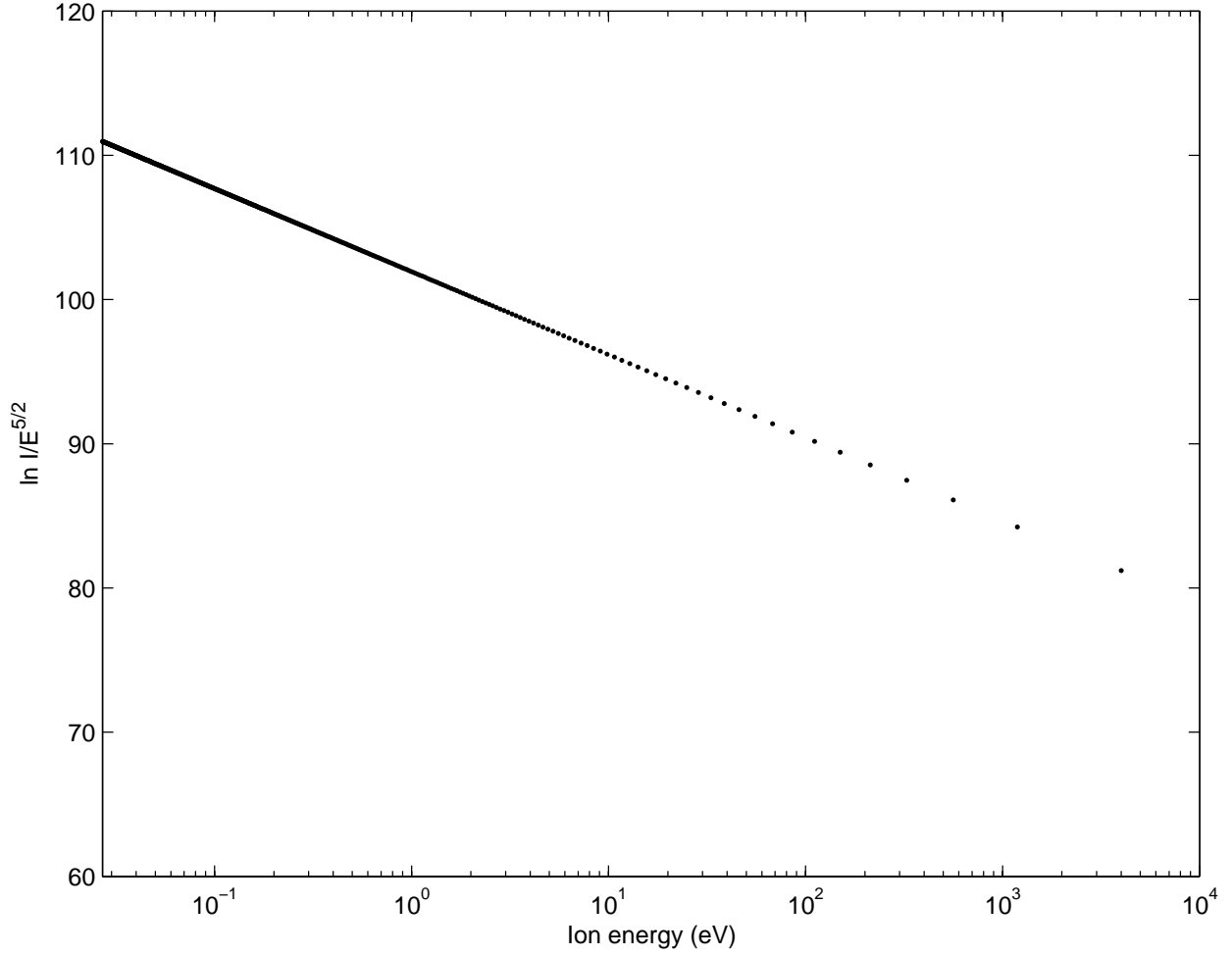


Figure 3.4: Values of $\ln(I/E^{5/2})$ versus ion energy E for estimation of initial ion temperature via kinetic theory.

The inverse of the derivative of Eq. 3.51 is equal to $\frac{dt}{dE}$:

$$\frac{dt}{dE} = \frac{lm_i^{1/2}}{2\sqrt{2}E^{3/2}} \quad (3.54)$$

With Eq. 3.54, Eq. 3.53 becomes:

$$\frac{dN}{dE} = \frac{I}{e} \frac{lm_i^{1/2}}{2\sqrt{2}E^{3/2}} \quad (3.55)$$

It can be shown that if $g(E)$ is the energy distribution function, the $\frac{dN}{dE} = g(E)$. [80] If the initial distribution of ion energies is Maxwellian, then

$$g(E) = N_0 \frac{2}{\sqrt{\pi}} E^{1/2} \frac{1}{kT_i} \exp(-E/kT_i) \quad (3.56)$$

where N_0 is the total number of ions, E is the ion energy, and T_i is the ion temperature. Multiplying Eq.

3.56 by $E^{1/2}$ due to the assumption of an effusive source,[80], then Eq. 3.55 becomes:

$$N_0 \frac{2}{\sqrt{(\pi)}} E \frac{1}{kT_i} = \frac{I}{e} \frac{lm_i^{1/2}}{2\sqrt{2}E^{3/2}} \quad (3.57)$$

Rearranging Eq. 3.57 yields an equation that yields the ion temperature via linear regression:

$$\ln \left(\frac{2\sqrt{8}N_0}{lm_i^{1/2}kT_i^{1/2}\sqrt{\pi}} \right) - \frac{E}{kT_i} = \ln \left(IE^{-5/2} \right) \quad (3.58)$$

where I is the detected current as a function of time. By plotting values of $\ln \left(IE^{-5/2} \right)$ versus the energy E , a line with slope $-1/kT_i$ should be created. This will be true if the initial distribution function was Maxwellian, and the uncertainty in the energy detected at time t is small. This analysis was performed on the data from this experiment. However, as shown in Fig. 3.4, there are no linear regions of the graph. The graph was plotted as a semi-log plot, with the logarithmic scale on the x-axis, to illustrate this point. If the value of $\ln \left(IE^{-5/2} \right)$ were linear with energy on a standard plot, it would not be so on a semi-log x-axis plot. Thus, the effects of a possible non-Maxwellian initial distribution function and the errors in the collection of ions due to finite probe size effects make the use of Langmuir probe ion saturation currents as time of flight signals erroneous.

3.3 Energy Balance

3.3.1 Neutral Atom Densities

In the previous work, reliable measures of neutral atom density were not available. To determine the neutral atom density, mass loss data are taken as described in the Experimental chapter. Figure 3.5 shows the mass loss data as a function of laser energy density. The mass loss, and thus total number of particles, increases with increasing laser energy. Total particle inventory is calculated by:

$$N = \frac{\Delta M}{12} \cdot 6.022 \times 10^{23} \quad (3.59)$$

The total particle inventory is between $\approx 6 \times 10^{15}$ to $\approx 10 \times 10^{15}$ over the range of laser energies used for the mass loss experiment. It should be noted that there is no a priori reason for the mass loss to increase linearly with the laser energy. It is necessary to consider possible loss mechanisms for the incident laser energy that may not behave linearly with increasing laser energy. For instance, changes in reflectivity, thermal conduction of heat, and the absorption of the laser light by the plasma will alter the amount of material ablated. A logarithmic model provides a better fit to the data.

From the neutral atom inventory, the neutral atom density may be calculated with an appropriate model. Mayo, et al, propose a model with a $1/r^2$ dependance radially away from the laser spot and a $\cos^m\theta$ angular dependance.[32, 67] The $\cos^m\theta$ dependance is from results of thickness profiles of deposited films. Values of the forward peaking factor, m , have been determined in the previous work.[24] The inverse square dependance

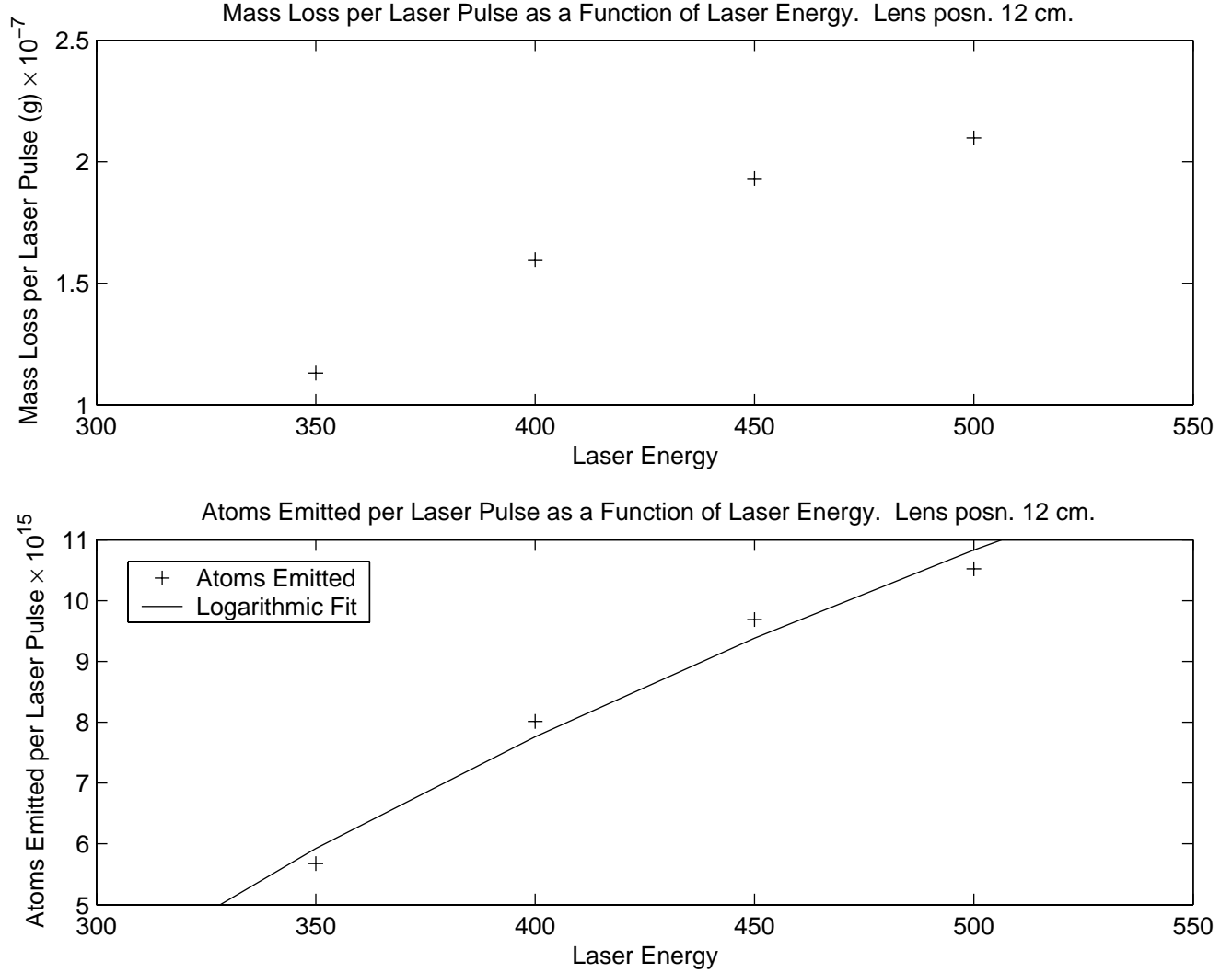


Figure 3.5: Mass loss and total particle inventory as a function of laser energy.

is a result of expansion in to a half space, 2π radians. If the expansion was isotropic in all space, 4π radians, then the density dependance would be $1/r^3$. [25] The density model is thus:

$$n(r, \theta) = \frac{n_0 r_0^2}{r^2} \cos^m \theta \quad (3.60)$$

where $n(r, \theta)$ is the density and angular dependant density, n_0 is an initial density at some point r_0 , r is the radial distance from the target, θ is the angle from the centerline of the plume, and m is the forward peaking factor.

By integrating Eq. 3.60 over r, θ , an expression for the quantity $n_0 r^2$ is derived:

$$n_0 r_0^2 = \frac{m+1}{4\pi\Delta} N \quad (3.61)$$

where N is the total number of particles, and Δ is the azimuthal plume thickness. Mayo, et al, give $\Delta = 5 \text{ cm}$. [32, 67] With Eqs. 3.60 and 3.61, the total heavy particle density, including neutral atoms and

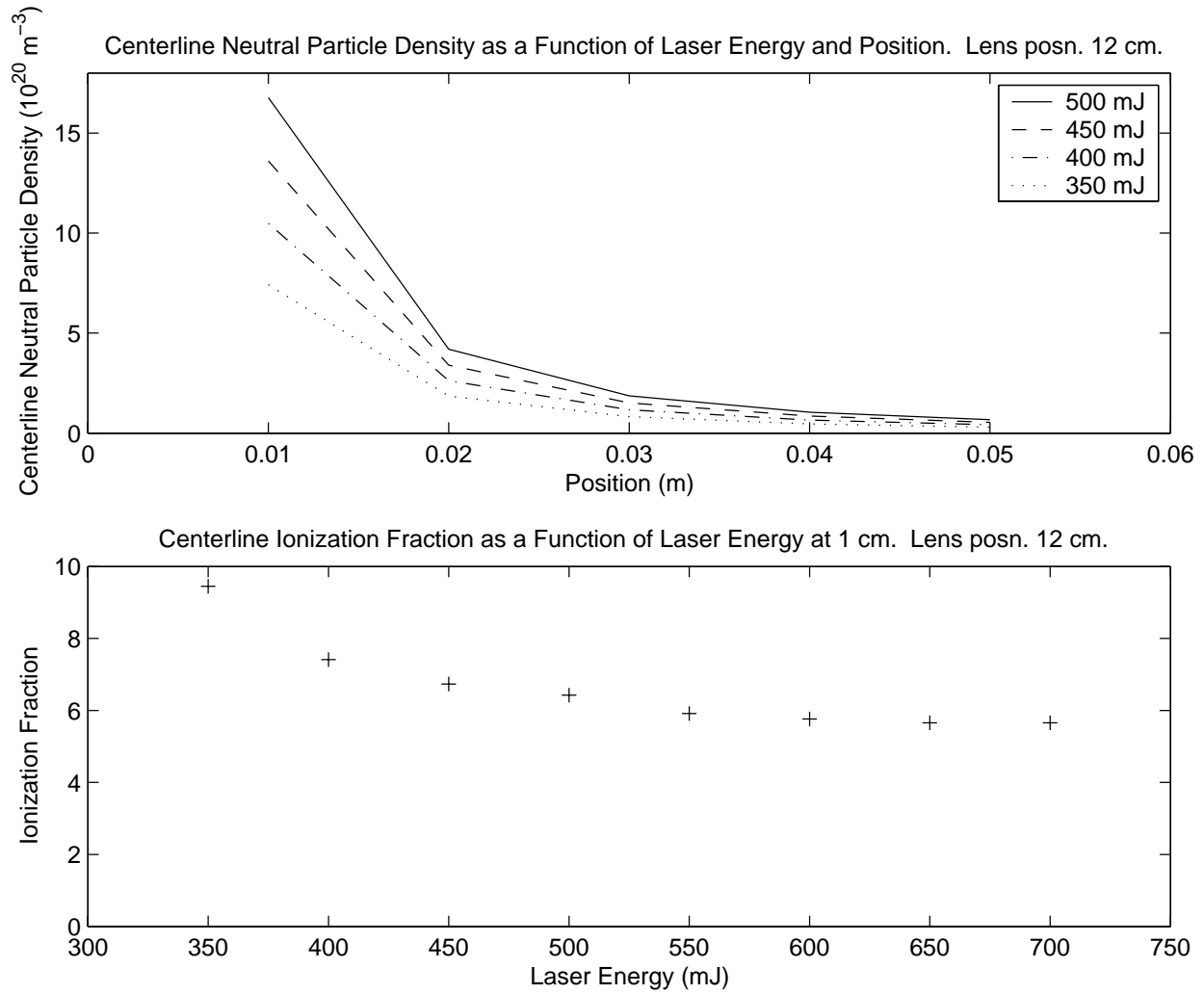


Figure 3.6: Neutral atom density and ionization fraction as a function of laser energy.

ions, is:

$$n(r, \theta) = \frac{m+1}{4\pi\Delta} N \frac{1}{r^2} \cos^m \theta \quad (3.62)$$

The values of m for this experiment are found in previous work on this same experimental setup.[24] Total number of particles have been calculated using Eq. 3.59. The ionization fraction may be calculated from the total particle density and the ion density from the previous research:

$$f_i = \frac{n_i}{n(r, \theta)} \quad (3.63)$$

where f_i is the ionization fraction, n_i is the ion density from previous research, and $n(r, \theta)$ is the total particle density, Eq. 3.62.

Figure 3.6 shows the total heavy particle density and the ionization fraction as a function of energy over the energy range used in this experiment. The heavy particle densities show a clear decrease with decreasing laser energy. This behavior is expected as both the total number of emitted particles and the value of the

forward peaking factor decrease with decreasing laser energy. The behavior of the ionization fraction with laser energy shows an unexpected trend. Ionization fraction decreases with laser energy, at least over the range of laser energies used. However, the relative decrease is not large, only between ≈ 9 to ≈ 5 percent. It is clear that the plasma plume created in the laser ablation of graphite is largely composed of neutral atoms.

3.3.2 Energy Balance

An energy balance on the plasma plume provides an understanding of the transfer of energy between the laser and the plasma. Mass loss data provides ionization fractions and total number of particles in the plume. Flow speeds, ion densities, and electron temperatures are known from the previous work on the same experiment.[24] The incident laser energy will be divided into a number of partitions within the plasma and the target. The first of these is the kinetic energy of the different plasma species. This is expected to be the most significant partition of energy, as adiabatic expansion converts the initial plume thermal energy into kinetic energy. The second energy partition is plume thermal energy. Results show that the electrons have a significant temperature as far away as 5 cm from the target. Third, laser energy may be lost to conduction of thermal energy to the target. Fourth, the plasma may lose energy via radiation losses. Fifth, some amount of the incident laser energy may be reflected. For metallic targets, such as aluminum, or silicon, which behaves as a metal when liquid, reflection losses are significant.

The first energy partition is the kinetic energy of the plume constituents. Two important assumptions are made for this part of the energy balance. First, the total number of particles emitted is a logarithmically increasing function of laser energy. This assumption is used to extrapolate N , the total number of particles emitted, for laser energies of 550 mJ and 700 mJ. Second, the neutral atom flow speed is taken to be equal to the ion flow speed. Experimental results on similar experiments have shown this not necessarily to be true. However, in the absence of such data on the present experiment, this assumption is made. Thus, the total energy associated with flow for ions, electrons, and neutral atoms are as follows:

$$E_{flow}^{ion} = \frac{1}{2} f_i N m_i u_i^2 \quad (3.64)$$

$$E_{flow}^e = \frac{1}{2} f_i N m_e u_i^2 \quad (3.65)$$

$$E_{flow}^n = \frac{1}{2} (1 - f_i) N m_i u_i^2 \quad (3.66)$$

In Eqs. 3.64, 3.65, and 3.66, f_i is the ionization fraction, N is the total number of particles, m_i is the ion mass, m_e is the electron mass, and u_i is the ion flow speed. In fact, the electron flow component is negligible. This is due to the small electron mass.

$$E_{flow}^e = \frac{m_e}{m_i} E_{flow}^{ion} \approx 4.573 \times 10^{-5} E_{flow}^{ion} \quad (3.67)$$

Table 3.5 shows the results of the kinetic energy partition of the energy balance. Note that $E_i = \frac{1}{2} m_i u_i^2$. The kinetic partition of the energy balance contains a significant amount of the incident laser energy. Due to the

Table 3.5: Kinetic energy partition of the energy balance.

E_l (mJ)	E_i (eV)	$N \times 10^{15}$	f_i	E_{flow}^{ion} (mJ)	E_{flow}^n (mJ)
350	108.27	5.676	0.0945	9.29	89.03
440	149.53	9.689	0.0581	13.5	218.34
550	196.56	12.146	0.0449	17.15	364.83
700	281.91	15.465	0.0364	25.39	672.2

low ionization fraction, the neutral atoms carry the dominant fraction of the plume kinetic energy. In the 700 mJ case, 97 percent of the energy is accounted for in the flow component alone. This is an indication that the neutral atom flow speeds are less than the ion flow speeds, as the contribution from other partitions of the energy balance will make this number greater than 100 percent.

The second energy partition is the thermal component of the plume. In the adiabatic expansion process, thermal energy is converted to kinetic energy. Electron temperatures are the only experimentally known temperature from the previous work on the same experiment.[24] Ion temperatures and neutral atom temperatures have not been determined experimentally. An optical multichannel analyzer with sufficient small resolution can detect doppler broadening, which leads to an estimate of the neutral atom or ion temperature. The thermal energy of each component is as follows:

$$E_{th}^{ion} = f_i N k T_i \quad (3.68)$$

$$E_{th}^e = f_i N k T_e \quad (3.69)$$

$$E_{th}^n = (1 - f_i) N k T_n \quad (3.70)$$

For the purposes of this estimate, the neutral atom and ionic thermal energies are set equal to the electron thermal energy. However, it is likely that the ions and neutral atoms, after expanding, are cold. The low electron-ion and electron-neutral collision frequencies permit electrons to maintain a larger thermal energy while the ions and electrons are cold. By summing Eqs. 3.68, 3.69, and 3.70, the thermal component of the energy balance is determined and is shown in Table 3.6. Electron temperatures are for the 1 cm Langmuir probe position. The thermal energy component represents only a small component of the plume energy balance. Thermal energy contributes 3 to 4 percent of the total incident laser energy at the 1 cm Langmuir probe position. This is consistent with adiabatic, as opposed to isothermal, expansion.

As stated previously, the third energy partition is conduction of thermal energy to the target. At the plasma-solid interface, thermal energy is transferred to the solid. Thermal energy losses may be estimated from the heat flux at the plasma-solid interface. Under this assumption the thermal energy lost by conduction, E_{cond} , would be:

$$E_{cond} = k_G A_s \tau_{laser} \frac{dT}{dx} \quad (3.71)$$

where k_G is the thermal conductivity of graphite, A_s is the spot size, τ_{laser} is the laser pulse length, and T is the temperature. This could be calculated exactly if the heat flux from the plasma were known at

Table 3.6: Thermal energy partition of the energy balance.

E_l (mJ)	$N \times 10^{15}$	f_i	kT_e (eV)	E_{th} (mJ)
350	5.676	0.0945	10.12	10.06
440	9.689	0.0581	10.61	17.40
550	12.146	0.0449	11.21	22.76
700	15.465	0.0364	12.02	30.82

Table 3.7: Conducted energy partition of the energy balance.

E_l (mJ)	Δz m	E_{cond}
350	2.326×10^{-7}	65.94
440	3.285×10^{-7}	46.68
550	3.971×10^{-7}	38.62
700	4.313×10^{-7}	35.56

the plasma-solid boundary, as well as the thermal properties of the solid at the evaporation temperature. However, knowledge of the heat flux from the plasma requires a knowledge of the electron temperature at the plasma-solid interface. For a simple order-of-magnitude estimate, let dx be the thickness of evaporated material, and $dT \approx 3426.5$ K, the vaporization temperature of graphite. The thermal conductivity of graphite is taken to be the room temperature value, $k_G = 37.7$ W/mK. Using a spot size of 0.04 cm², and evaporated thicknesses calculated from Eq. 3.6. It is not clear that the values in Table 3.7 are necessarily correct. The larger laser energies have larger evaporated thicknesses. This makes the heat flux smaller, since the same increase in temperature is over a larger area. As laser energy increases, the plume temperature is expected to increase. The heat flux due the plasma at the solid-plasma interface should increase with increasing electron temperature. Also, the plasma during the laser pulse must be very warm to produce the observed ionization states, and thus the temperature differential larger. Without access to more detailed data on the plume physics during the laser pulse, these values will be used in the energy balance.

The fourth partition of energy is energy which is radiated out of the plasma volume. Losses by radiation are difficult to quantify. During the laser pulse, the plume is considered to be in local thermodynamic equilibrium. This, it should radiate similar to a black body. Use of the temperatures in Table 3.1 will yield radiation losses several times as large as the incident energy. However, this temperature listed is the temperature at the end of the laser pulse, which means that time dependant data on the temperature is necessary. Also, the plasma may not emit as a perfect black body, reducing the amount of energy lost from the black-body value.

$$E_{rad} = \epsilon \sigma A T^4 \tau_{laser} \quad (3.72)$$

where ϵ is emissivity, σ is the Stefan-Boltzmann constant, T is the temperature, τ_{laser} is the laser pulse length, and A is the laser spot area, neglecting the small thickness of the plasma plume during the pulse. If

Table 3.8: Energy balance of the pulsed laser deposition plasma.

E_l (J)	E_{flow}^{ion} (mJ)	E_{flow}^n (mJ)	E_{th} (mJ)	E_{cond} (mJ)	E_{rad} (mJ)	E_{refl} (mJ)	E_{tot} (mJ)
0.35	9.29	89.03	10.06	65.94	80.76	94.5	349.58
0.44	15.6	216.21	17.55	46.68	97.57	118.8	512.41
0.55	22.61	359.37	23.07	38.62	121.59	148.5	713.76
0.70	39.48	658.08	31.43	35.56	160.72	189	1114.27

the plasma is not a perfect black body, then $\epsilon < 1$. Furthermore, for the adiabatic assumption to be true, radiation losses must not be significant after the laser pulse ceases. It has been shown that line radiation represents a very small fraction of the total laser energy, less than one percent.[78] As an order of magnitude estimate, let the average plume temperature be half the experimental electron temperature and to account for the effects of time dependant temperatures, which will be small until the electron population becomes significantly large, and of deviations from the black body approximation. The energy loss is shown in the complete energy balance, Table 3.8.

Finally, the fifth partition of energy considered is that laser light which is reflected from the target. Metallic elements will reflect a significant fraction of incident light. For example, aluminum has a reflectivity of 97 percent. Carbon in graphite form has a reflectivity of 27 percent. Coupling the 27 percent reflection loss, the final energy partition is shown below in Table 3.8.

Clearly, this energy balance is incorrect. The ion and neutral atom temperatures are unknown in this research. There is uncertainty in the proper method to treat radiation and conduction losses. Neutral atom particle flow speeds are less than the ions, although they are still of the same order of magnitude.[75] The results of Claeysens, et al, indicate that the ion slow speed is approximately three times as great as the neutral atom flow speed.[75] Lade and Ashfold suggest that the neutral atom flow speed is half that of the ion flow speed in 193 nm laser ablation of graphite. A neutral atom flow speed of half to a third of the ion speed would bring the net energy balance to physical values.

The important result from the energy balance is that the dominant partition of incident laser energy is in kinetic energy. Thermal energy represents a small fraction, although it is still significant. Excitation and ionization within the plume is a function of the thermal energy. However, the majority of the excited and ionized species must form in the early stages of plume formation when densities are sufficiently large so that electron-ion and electron-neutral collisions are likely. Neutral atoms carry the majority of the incident laser energy. This is not surprising, given the small ionization fraction of the laser produced plasma. Neutral atoms must play a significant role in film formation. This idea will be developed in detail in the next chapter.

Table 3.9: Sheath potentials at a substrate 4 cm from the target as a function of laser energy.

E_l (mJ)	u (m/s)	T_e (eV)	ϕ (V)
350	41705	5.887	-18.24
440	49011	6.1544	-18.28
550	56192	6.4218	-18.38
700	67295	6.8230	-18.59

3.4 Plume-Substrate Interaction

Plume substrate interaction is typically not discussed in the modelling of laser ablation plasmas. However, it is quite relevant to the discussion of film growth and formation. A simple model of sheath formation and plume substrate interaction is proposed. In order to understand how the incident ions will interact with the substrate, it is necessary to understand sheath formation.

The first step is to calculate the potential of the substrate. In an arbitrary PLD system, the substrate may be biased via a voltage supply. For this research, there was no biasing of the substrate. The silicon substrate, which is backed by a metal plate, and then a ceramic holder, cannot conduct a net current. Thus, it is assumed that the substrate is at the floating potential. This potential is estimated as follows.

At the floating potential, the ion and electron currents are equal. The electron current is given by:

$$i_e = J_e A_e = en_{e0} v_{th,e} A_e \exp\left(\frac{e\phi}{kT_e}\right) \quad (3.73)$$

In general, the floating potential is less than the plasma potential, so $\phi = \phi_{plasma} - \phi_{subs.} < 0$. Thus, electrons are repelled by the substrate and the electron flux is reduced. Assuming the sheath potential does not significantly perturb the incident ion speed, the ion current to the substrate is:

$$i_i = J_e A_e = en_{i0} 0.61 \frac{kT_e}{m_i} + en_{i0} u A_{\perp} \quad (3.74)$$

In this case, the area perpendicular to the flow A_{\perp} is identical to the total ion collection area A , which is equal to the total electron collection area A_e . By setting Eqs. 3.73 and 3.74 equal, an expression for the potential ϕ is derived:

$$\phi = kT_e \ln\left(\frac{0.61 u_{boh m}}{v_{th,e}} + \frac{u}{v_{th,e}}\right) \quad (3.75)$$

The plasma potential may be arbitrarily set to zero, assuming quasineutrality in the bulk plasma. With this assumption, Eq. 3.75 is the sheath potential.

The substrate potential becomes less negative as the flow speed increases, or the electron thermal speed decreases. If the flow speed increases, the potential must become less negative to compensate for the increase in ion flux. Similarly, if the thermal speed of the electrons decreases, then the potential must become less negative to compensate for the decrease in the electron flux. As the electron temperature is a function of position within the plasma, the sheath potential will change with substrate location.

Sheath potentials as a function of laser energy are shown in Table 3.9. The electron temperature is calculated from the average of the 3 *cm* and 5 *cm* data. There is only a difference of a few tenths of an *eV* between these positions. Given that flow speeds and temperatures are not better than ten percent accurate,[24], these sheath potentials are essentially identical for the laser energies used. Ions traveling through this sheath will gain ≈ 18 *eV* of energy. This increases further the ion speed from the neutral atom flow speed.

When the incident flux of particles interacts with the substrate, it may sputter off some of the already deposited material. The sputtering yield is calculated using an empirical model from Nastasi, Mayer, and Hirvonen.[81] It is calculated with the following formula:

$$Y(E) = \frac{0.42\alpha_s Q_s S_n(E)}{U_0(1 + 0.35U_0 S_e(\epsilon))} \left(1 - \left(\frac{E_{th}}{E}\right)^{1/2}\right)^{2.8} \quad (3.76)$$

where $Y(E)$ is the sputtering yield for ions of energy E . The parameters U_0 and Q_s are equal to 7.37 *eV* and 2.69 *eV*, respectively. E_{th} is given by:

$$E_{th} = \left(\frac{4}{3}\right)^{4/3} \frac{U_0}{\gamma} \quad (3.77)$$

The parameter γ is defined as:

$$\gamma = \frac{4M_1M_2}{(M_1 + M_2)^2} \quad (3.78)$$

where M_1 and M_2 are the mass of the incident ion and the target, respectively. The function α_s is an experimentally determined function, given by:

$$\alpha_s = 0.10 + 0.155 (M_2/M_1)^{0.73} + 0.001 \frac{M_2}{M_1} \quad (3.79)$$

In Eq. 3.76, the reduced energy ϵ , is given by:

$$\epsilon = \frac{0.03255}{Z_1 Z_2 \left(Z_1^{2/3} + Z_2^{2/3}\right)^{1/2}} \frac{M_1}{M_1 + M_2} E \quad (3.80)$$

where E is the energy in *eV*, Z_1 is the incident ion atomic number, and Z_2 is the target atom atomic number. The electronic stopping cross section, $S_e(\epsilon)$ is simply:

$$S_e(\epsilon) = k\epsilon^{1/2} \quad (3.81)$$

with the constant k given by:

$$k = \frac{Z_1^{2/3} Z_2^{2/3} (1 + M_1/M_2)^{3/2}}{12.6 \left(Z_1^{2/3} + Z_2^{2/3}\right)^{3/4} M_2^{1/2}} \quad (3.82)$$

The nuclear stopping cross section, $S_n(E)$ is given in terms of the reduced energy as $S_n(E) = K_n S_n(\epsilon)$. The parameter K_n is given by:

$$K_n = \frac{8.478 Z_1 Z_2}{\left(Z_1^{2/3} + Z_2^{2/3}\right)^{1/2}} \frac{M_1}{M_1 + M_2} \quad (3.83)$$

Table 3.10: Sputtering yield and sputtered flux as a function of laser energy. Note that the density indicated is at 4 cm from the target.

E_l (mJ)	E_i (eV)	n_i (m^{-3})	ϕ_i ($m^{-2}s^{-1}$)	$Y(E)$	Γ_S ($m^{-2}s^{-1}$)
350	108.27	1.01×10^{19}	4.21×10^{23}	0.0386	1.62×10^{22}
440	149.53	1.30×10^{19}	6.37×10^{23}	0.0764	4.85×10^{22}
550	196.56	1.70×10^{19}	9.55×10^{23}	0.118	1.12×10^{23}
700	281.91	2.27×10^{19}	1.53×10^{24}	0.182	2.77×10^{23}

The nuclear stopping cross section in terms of the reduced energy is:

$$S_n(\epsilon) = \frac{3.441\epsilon^{1/2} \ln(\epsilon + 2.718)}{1 + 6.355\epsilon^{1/2} + \epsilon(6.882\epsilon^{1/2} - 1.708)} \quad (3.84)$$

The set of equations describing sputtering is best calculated with a computer program. For the incident ion energies, the sputtered flux is calculated from the sputtering yield by:

$$\Gamma_S = Y(E)n_i(E)v(E) \quad (3.85)$$

where Γ_S is the sputtered flux, $Y(E)$ is the sputtering yield, $n_i(E)$ is the density, and $v(E)$ is the speed of ions with energy E . The ion density must be that at 4 cm from the target, as this is the location of the substrate. This is calculated using the inverse square model as discussed in the mass loss and energy balance discussion. The results of the sputtering yield and flux analysis are shown in Table 3.10. Incident ion flux, ϕ_i is also shown for comparison.

The calculated sputtering fractions agree with those determined computationally.[82] There exists the possibility of sputtered atoms becoming redeposited. Even if the sputtered atoms are ionized, they will gain a maximum energy equal to the sheath potential. The collision cross section with plume atoms will be small as discussed in the Collisions subsection of the Langmuir probe section. These low energy atoms will preferentially form sp^2 coordination. However, the probability of ionization is small, as the ion-ion collision frequency is approximately identical to the electron-electron collision frequency. Those sputtered atoms which remain neutral will also not likely be backscattered by the incident plume, given the small ion-neutral and neutral-neutral collision frequencies, and large collision mean free paths.

Chapter 4

Growth of Diamond-like Carbon Films

The mechanisms by which diamond-like carbon films grow have not been completely determined. Several attempts have been made to describe and model film formation. These models include kinetic energy and thermal quench models,[83] molecular dynamics simulations,[84] and the subplantation model.[82, 85] The first section of this chapter will discuss these models of diamond-like carbon film growth. While these models are important for understanding the growth of diamond-like carbon films, they do not consider all of the constituents in the plasma and their effects on film growth. The second section of this chapter discusses an energy barrier deposition model for diamond-like carbon films as a function of plasma parameters. In the third section of this chapter, experimental results are presented and interpreted in terms of the energy barrier model.

4.1 Current Diamond-like Carbon Models

4.1.1 Cuomo's Model

One of the earliest models of diamond-like carbon film growth is due to Cuomo, et al.[83] The incident ion kinetic energy and the removal of excess heat, the thermal quench, are key to their model. Ions with a sufficient kinetic energy will form sp^3 coordinated sites, whereas low kinetic energy carbon atoms will form sp^2 sites in a graphitic structure. In this model, the kinetic energy of the incident ion drives a change in geometry from graphite to diamond structure. The details of the processes by which kinetic energy controls sp^3 fraction are not discussed. Once an sp^3 site has been formed, the excess energy must be removed sufficiently rapidly, because the sp^3 coordination is metastable. If thermal energy cannot be removed in a sufficiently small time, then sp^3 coordinated sites which have formed will revert to sp^2 coordination.

In their pulsed laser deposition data, there is not a significant change in the sp^3 fraction of DLC films deposited on substrates with different thermal diffusivities. A reduction in the substrate temperature caused a slight decrease in the sp^3 fraction for DLC films deposited by PLD, whereas the sp^3 fraction for DLC films deposited via ion beam sputtering increased. The most significant increase was seen for *NaCl* substrates,

although the thermal conductivity of *NaCl* does not change dramatically between room temperature and 77 K. Later work by Chhowalla, et al, showed that the sp^3 fraction of DLC did not change with deposition temperature until ≈ 250 C.[3] While it may be important to rapidly remove heat locally, the thermodynamic properties of the substrate do not appear to play a role in the deposition of diamond-like carbon. Substrate temperature becomes important if local temperature remains high enough to promote the transition of sp^3 sites to sp^2 sites.

4.1.2 Molecular Dynamics

Molecular dynamics(MD) simulations are a more accurate means of analyzing the growth of DLC films. [18, 86, 84, 87, 88, 89] In these methods, an ensemble of carbon atoms is heated to liquid at 5000 K and then cooled to room temperature in a time scale of the order of picoseconds. Atomic bonding and dynamics of these atoms are followed using classical mechanics calculations. The number of atoms which may be simulated is limited by available computational power. Recent results have used 640 carbon atoms in the simulation of the deposition of diamond-like carbon.[86] Cooper, et al, attempted a simulation of deposition of DLC on diamond with 100 eV carbon atoms.[86] They were able to reproduce experimental results suggesting that the surface layers of DLC films are mostly sp^2 coordinated.[90] The computational results of Marks, et al,[18] show an increase in sp^3 fraction with shorter cooling times, in agreement with the conclusions of Cuomo's model, in that thermal energy must be removed rapidly to preserve the metastable sp^3 coordination. Film density must be supplied a priori and these models tend to underestimate the sp^3 fractions found experimentally.[84] They do, however, show the experimentally observed increase in film density with increasing sp^3 fraction.[84] It should be noted that carbon does not form a liquid unless under extreme pressure. These models assume that a thermal spike created by the incident ion induces a small, liquid region in the film.[91] Computational power is improving, and as many as 10,000 atoms or more may be used in MD simulations.[92]

4.1.3 Subplantation

A third model of DLC formation is the subplantation model, which is mostly due to Lifshitz. [1, 82, 22] The model posits that film growth occurs not on the surface, but a few layers beneath the surface, dependent on the ion and substrate properties. Lifshitz summarizes the processes as follows: carbon atoms penetrate the surface layer, incorporate themselves into the existing diamond-like carbon matrix, and increase stress locally within the film. He postulates that it is this increased stress which drives formation of the sp^3 phase. It is not clear, however, why increasing ion kinetic energy would act to increase the local stresses and increase the sp^3 fraction.

The subplantation deposition model of Lifshitz is placed on a quantitative basis by Robertson.[85, 93] He calculates an expected increase in density in the first few monolayers of an already deposited film from an incident carbon ion flux. Then, using known experimental relation between density and sp^3 fraction,

the sp^3 fraction is calculated from the density increase via interpolation. His explanation for the physical mechanism behind this is:[85]

In the highly energetic conditions of ion bombardment, atomic hybridizations are expected to adjust readily to the local density, becoming more sp^2 if the density is low and more sp^3 if the density is high.

Film density does not always increase as a result of ion implantation. This model must assume that the surface is infinitely rigid, so that there will be no deformation of the surface layers to accomodate stress. Furthermore, the adjustment of bonding to density is an equilibrium thermodynamic process. This neglects the non-equilibrium nature of ion deposition processes, and the necessity to surpass the activation energy between the sp^3 and sp^2 states.

For the deposition of diamond in CVD type systems, the preferential displacement of graphite is necessary in his model. However, in diamond-like carbon, the displacement energies of sp^3 and sp^2 coordinated carbon should be similar, as the reduced displacement energy of carbon in graphite is due to the weak Van der Waals bonding between graphite planes. In fact, the in-plane bond strength of sp^2 coordinated carbon is stronger than the bonding found in sp^3 coordinated carbon. There are, however, three σ bonds for sp^2 coordinated carbon and four σ bonds for sp^3 coordinated carbon. Thus, it is expected that the displacement energy for the sp^2 components of diamond-like carbon films to be slightly less than that of the sp^3 component.

4.2 Energy Barrier Deposition Model

Each of the previously discussed models provides insight in to the formation of diamond-like carbon films. These models do not, however, discuss the importance of different plasma parameters in detail. They state the importance of ion kinetic energy, but do not describe by what means ion kinetic energy is a factor in the formation of sp^3 coordination states in diamond-like carbon. The energy barrier model discussed in this section is an extension of the previous models, accounting for the different plasma constituents and the means by which sp^3 coordination is related to these parameters.

First, consider the mechanism by which the carbon atoms achieve three and four-fold coordination. Given the ground state of carbon $1s^2 2s^2 2p^2$, it might be expected that carbon will form only two bonds via its two $2p$ electrons. However, this limitation is overcome by electron excitation and orbital hybridization. Excitation occurs when a $2s$ electron is excited to an empty $2p$ state.



Three and four-fold coordination is achieved by hybridization of the one $2s$ electron and the three $2p$ electrons. In order for four-fold coordination to occur, further excitation is necessary.[94]



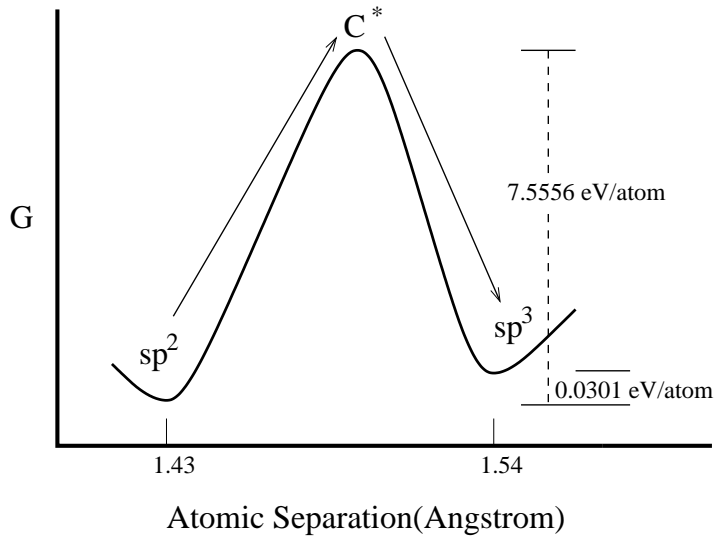


Figure 4.1: Free energy diagram describing the processes involved in formation of sp^3 coordination.

At sufficiently high temperatures and pressures, this reaction becomes thermodynamically favorable. However, under typical deposition conditions, some amount of energy must be supplied to drive this reaction. This is shown in Fig. 4.1. The net energy difference at room temperature is only $2.9 \text{ kJ/mol} \approx 0.0301 \text{ eV/atom}$ between the sp^2 and sp^3 states.[95] As shown in Fig. 4.1, the energy that must be supplied to drive the $sp^2 \rightarrow sp^3$ reaction is large, 7.5556 eV/atom . Thus, during ion-solid interaction, approximately 8 eV/atom must be supplied to form sp^3 coordination. However, if the transferred energy is close to the damage energy, existing sp^3 sites will be converted into graphitic sp^2 sites.

In pulsed laser deposition, this energy is supplied through laser-solid interactions. A large amount of laser energy is deposited in to a small volume on the target material, in this carbon, which creates a plasma plume with highly energetic species. A dense, isothermal plasma is created at the surface of the target. It expands adiabatically, converting thermal energy into kinetic energy.[96, 24] After expansion, the energetic neutral atoms and ions within the plasma plume form diamond-like carbon films as they interact with the substrate. The neutral atoms at ions may be in excited states due to interaction with electrons and photons within the plume. In pure ion beam techniques, such as mass selected ion beam deposition, only ions are incident upon the substrate. These nonequilibrium growth techniques permit the creation of non-equilibrium structures as their associated energies per atom are significantly greater than the thermal energy of the film.

The energy of the initial laser pulse is present in the plasma plume as the kinetic energy of the plume constituents and the electronic excitation of the various species within the plume. Electronic excitation occurs by electron and photon interaction with the plume species. It is the electronic excitation of the incident species which helps drive the reaction in Eqs. 4.1. and 4.2. For ionized species, recombination during interaction with the target is a second source of electronic excitation. Recombination at the surface will not necessarily be to the ground energy state, depending on the neutralization mechanism. For neutral

atoms, excitation is due to electron-neutral collisions. During the initial stages of the plume, photon driven excitation may occur provided the density of neutral atoms is sufficiently high.

Incident ions will recombine and become neutral atoms within a monolayer of the surface by capturing a film or substrate electron. This can occur by radiative capture, Auger recombination, or resonance tunneling. In radiative capture, the incident ion captures a film electron in the ground state. Given the long radiative state lifetimes, this process is not important.[97] Resonance recombination occurs when a film electron tunnels to the incident ion. This process is degenerate in energy. Thus, in resonance recombination of a film electron from a π or σ orbital to an incident carbon ion, the now neutral ion will be left in an excited state with electron excitation energy equivalent to the energy of the π or σ orbital from which it was captured. Auger recombination is similar to radiative recombination in that a film electron is captured by the incident ion in the ground state, however, rather than photon emission occurring, a film electron is excited.[97] A simple estimate of the capture cross section is given in the Bohr-Lindhard model as:

$$\sigma_c \approx \pi a_b^2 Z_1^2 Z_2^{1/3} \left(\frac{v}{v_b} \right)^3 \quad (4.3)$$

where v is the incident ion speed, v_b is the Bohr velocity, $2.188 \times 10^6 \text{ m/s}$, a_b is the Bohr radius, 0.0529 nm , Z_1 is the incident ion atom number, and Z_2 is the film atomic number. For a typical ion speed of $5 \times 10^4 \text{ m/s}$,[24], the capture cross section is $\sigma_c \approx 4.8 \times 10^4 \text{ nm}^2$. Using an assumed density of 3 g/cm^3 , typical for diamond-like carbon, the mean free path for electron capture is $\approx 1.4 \times 10^{-7} \text{ nm}$. Any ion created in typical pulsed laser deposition conditions will be neutralized within the first monolayer. After neutralization, the atom may be left in an excited state. Thus, ions and excited neutrals within the plume are indistinguishable once they have begun to interact with the substrate or previously deposited film.

In order to create the sp^3 coordination and form a σ bond, the incident, excited atoms may:

- I) Diffuse to another incident, excited atom within the film
- II) Attach to an sp^3 coordinated film atom and form a σ bond
- III) Attach to an sp^2 coordinated film atom and form a σ bond
- IV) Excite an already deposited film atom from sp^2 coordination to sp^3 coordination.

These processes are determined by the range of the incident atoms in the film. The range of the incident atom is controlled by the manner in which it interacts and loses its kinetic energy to the film atoms. As the incident atom interacts with either the substrate or the previously deposited atoms, its kinetic energy is lost via nuclear and electronic stopping. Briefly, electronic stopping is due to excitation of the film electronic structure through Coulombic interactions and nuclear stopping is due to collisions with the nuclei of the deposited atoms. Given that the incident ions are rapidly neutralized, nuclear stopping is dominant.

The range of the incident atoms controls two parameters. The first is the number of opportunities that the incident atoms has to exchange electronic excitation. If the range is too large, then there will be a

sufficient amount of collisions such that the incident, excited, atom will lost its electronic excitation. The second is the probability that two incident, excited atoms will interact and form an sp^3 dimer. Excitation energy is transferred in a manner similar to excitation energy transfer in gases and plasmas:



In the interaction, the incident excited atom X^* collides with film atom Y , which is in an unexcited state. After the collision, the incident atom is de-excited to state X^{**} . It is possible that the incident atom loses its excitation energy entirely. The film atom is left in an excited state Y^* with energy equal to the amount lost by the incident atom X . Collisional excitation due to the kinetic energy of an incident atom is small, of the order of m_e/m_i where m_i is the incident atom mass. The cross section for the excitation exchange process described in Eq. 4.4 decreases with increasing incident atom (atom X for this case) kinetic energy. [] Thus, atoms with a larger incident kinetic energy will have a smaller probability of losing excitation energy during a collision.

An estimate of range derived from experimental data is given in the book by Nastasi, Mayer, and Hirnoven.[81] The reduced(dimensionless) range, ρ is given by a power law expression:

$$\rho = \frac{1 - m}{m\lambda_m} \epsilon^{2m} \quad (4.5)$$

where m and λ_m are fitting parameters, and ϵ is the reduced energy. The fitting parameters are taken to be $m = 1/3$ and $\lambda_m = 1.309$, as are appropriate for low incident energies. The reduced energy, ϵ is given by:

$$\epsilon = \frac{M_2}{M_1 + M_2} \frac{a_{TF}}{Z_1 Z_2 e^2} E \quad (4.6)$$

where M_1 is the incident atom mass, M_2 is the film atom mass, a_{TF} is the Thomas-Fermi screening distance, a_0 is the Bohr radius, Z_1 is the incident atom atomic number, Z_2 is the film atom atomic number, e is 1.44 eV nm and E is the incident atom kinetic energy. The Thomas-Fermi screening distance is:

$$a_{TF} = 0.885 \frac{a_0}{Z_1^{2/3}} \quad (4.7)$$

The true range is found from Eqs. 4.5 – 4.7 using the relation:

$$\rho = RN4\pi a_{TF}^2 \frac{M_1 M_2}{(M_1 + M_2)^2} \quad (4.8)$$

where N is the film density in nm^{-3} and R is the true range. An expression for the true range is thus derived from Eq. 4.8, with the appropriate values for carbon. The true range in a carbon film with density 3.0 g/cm^3 is:

$$R \approx 2.43\epsilon^{2/3} \text{ nm} \quad (4.9)$$

Table 4.1 shows the ranges of the incident carbon ions used in this experiment. If one monolayer is taken to be 1.54\AA , the atomic separation distance in diamond, then the incident atom ranges are only a few

Table 4.1: Atomic range in diamond-like carbon for the ion kinetic energies used in the experiment.

E (eV)	ϵ	R (Å)
108.27	0.03	2.35
149.53	0.041	2.89
196.56	0.054	3.47
281.91	0.078	4.44

monolayers. At these energies, the growth occurs beneath the surface. For the carbon ion energies used in this research, the number of collisions that the incident atom will undergo is no greater than four.

One conceivable mechanism of sp^3 formation is the diffusion of incident, excited, atoms to form sp^3 dimers (process I as stated earlier). The flux of incident atoms is given by:

$$\Gamma = nv \quad (4.10)$$

where n is the incident atom density and v is the incident atom speed. As necessary, but not sufficient condition, the flux should be sufficiently large such that there should be at least two incident atoms within an area with a radius equal to the atomic range within the time it takes to slow down and capture the incident atom. Ion beam techniques have fluxes of the order of $10^{22} \text{ m}^{-2}\text{s}^{-1}$. [1] From the previous chapter, the incident ion flux is of the order of $10^{23} - 10^{24} \text{ m}^{-2}\text{s}^{-1}$. The range of the incident carbon atoms is no greater than 0.5 nm for incident atom energies of interest. For ion beam techniques, there are thus 7.85×10^3 atoms within an area with radius equal to the range arriving per second on the film surface. The time scale of stopping within the diamond-like carbon film is $\approx 10^{-13} \text{ s}$. [1] Thus, there are 7.85×10^{-10} atoms which arrive within the incorporation time with an area swept out by the incident atom range. Even though the fluxes present in laser ablation are two to three orders of magnitude greater, this process is highly unlikely. Such processes may occur on the surface where diffusion lengths and times scales are much larger.

Processes, II and III from the earlier list, involve the slowing down and capture of the incident atom in sp^3 coordination by the film atoms. The film atoms remain unchanged in processes II and III, where the incident atom slows, is captured in sp^3 coordination, and forms a sigma bond with either sp^2 or sp^3 coordinated film atoms. It is important that the incident atom not undergo too many collisions, or it will lose its excitation energy. When the incident atoms slows sufficiently that it may be captured, the probability p of it being captured in sp^3 coordination is:

$$p \approx \exp\left(\frac{-\Delta G_{2 \rightarrow 3}}{E^*}\right) \quad (4.11)$$

where E^* is the excitation energy of the incident atom, $\Delta G_{2 \rightarrow 3}$ is the free energy required for the $sp^2 \rightarrow sp^3$ transition, 7.5556 eV/atom , and kT is the local temperature. If there are N incident atoms, then number of atoms which will be captured in sp^3 coordination:

$$N \exp\left(\frac{-\Delta G_{2 \rightarrow 3}}{E^*}\right) \quad (4.12)$$

The reverse reaction, that is, the reversion of those incident atoms from sp^3 to sp^2 coordination is:

$$N\nu_D \exp\left(\frac{-\Delta G_{2\rightarrow3}}{E^*}\right) \exp\left(\frac{-\Delta G_{3\rightarrow2}}{kT}\right) \quad (4.13)$$

If the excitation energy is greater than the free energy of formation, $\Delta G_{2\rightarrow3}$, then Eq. 4.11 indicates a probability of sp^3 fraction formation of greater than 100 percent. In this case, process IV from the earlier list will occur. Processes IV involves the creation of an sp^3 coordinated atom from both the incident atom and a film atom. The incident atom has a sufficient amount of excitation energy excite the electronic structure of a film atom while remaining electronically excited itself. This can drive a film atom from sp^2 to sp^3 coordination. Thus, from one incident atom, two sp^3 coordinated atoms are formed. However, if the incident atom interacts with an already sp^3 coordinated atom, it can cause it to revert to the sp^2 coordination. The probability for process IV to occur and produce two sp^3 coordinated sites is:

$$p \approx \exp\left(\frac{-\Delta G_{2\rightarrow3}}{E_i^*}\right) \times \exp\left(\frac{-\Delta G_{2\rightarrow3}}{E_f^*}\right) \quad (4.14)$$

where E_f^* is the excitation energy available to the film atom and E_i^* is the energy available to the incident atom. Thus, the excitation energy acts to reduce the effective barrier between sp^2 and sp^3 coordination. If the excitation energy is increased, the sp^3 fraction of the film will increase. The local temperature must not be allowed to rise too significantly, or the reverse $sp^3 \rightarrow sp^2$ reaction may become favorable. The rapid removal of thermal energy is therefore important, as indicated in the previously discussed models.

The speed of the incident atom controls how much of the initial excitation energy is lost through collisions with film atoms. As the speed of the incident atom increases, its range increases, and thus the number of collisions which it will experience with film atoms. In order to explain the increase in sp^3 fraction with increasing ion kinetic energy, the following is proposed:

- I The cross section for electron capture by an incident ion to an excited state increases with increasing ion kinetic energy.
- II The cross section for exchange of excitation energy increases as atom speed decreases in collisions of incident atoms with atoms in a solid.

The result of postulate I is that as the incident ion kinetic energy increases, the fraction of incident ions which are neutralized to excited atomic states increases. The result of postulate II is that incident atoms at slow speed will lose more of their excitation than those at higher speeds. Even though incident atoms with higher kinetic energies will have a larger range, they will have a lower probability of losing their excitation energy before capture. Eventually, the range will become sufficiently long that the decrease in excitation cross section is compensated for by the number of collisions.

The fraction of the incident ion or neutral kinetic energy which is not lost to electronic stopping is the damage energy. Damage energy is important in diamond-like carbon formation as displacements will cause reduction in the sp^3 fraction. Also, displacements and bond breaking permit relaxation of stress within

the film. The displacement energy of diamond is 80 eV, whereas the displacement energy for graphite is 25 eV.[82] This relatively low displacement energy for graphite is a result of the weak Van der Waals bonds between planes. In amorphous carbon, there is no such ordering of carbon atoms. Thus, the displacement energy of amorphous carbon is assumed to be similar to that of diamond. An estimate of the number of displacements is found from the incident kinetic energy E_0 and the damage energy E_d :[98]

$$N_d \approx \frac{0.8E_0}{2E_d} \quad (4.15)$$

At 200 eV the number of displacements per incident atom reaches 1. Further increases in ion kinetic energy may not lead to increases in sp^3 fraction due to the breaking of sp^3 bonds. Thus, more sp^3 bonds will be broken than are created. The breaking of sp^2 bonds will not lead to reduction in sp^3 fraction, although it can lead to stress reduction. Given the Eq. 4.15 is approximate, it is expected that at energies approximately equal to 200 eV, the sp^3 fraction of diamond-like carbon films will decrease. This is seen in the work of Praver, et al., with an ion beam source.[62]

The different processes of creation of sp^3 coordinated carbon atoms must balance the processes which form sp^2 coordinated carbon or revert sp^3 coordinated carbon atoms to sp^2 coordination. Displacement of carbon atoms from their sites acts to reduce the sp^3 fraction.

It should be noted that the neutral carbon atoms within the plume travel slower than the ions. During the expansion process, both hydrodynamic and electrostatic forces act on the ions. However, the neutrals are only influenced by hydrodynamic forces. This effect has been observed experimentally. Diamant, et al., found that the velocity of C^{++} was greater than the velocity of singly ionized carbon, C^+ , which was in turn greater than the neutral carbon C^0 velocity.[37] Claeysens, et al, found similar results. They observed a carbon ion flow speed of 41.2 km/s and a flow speed for neutral carbon atoms of 16.0 km/s.[75] The speed and fraction of neutral carbon atoms within the plume are thus important for film growth.

In laser plasmas which show a significant concentration of C_2 molecules, it has been observed that the sp^3 fraction is low. This effect is due to both the physics of molecular interaction with solids and with the types of plasmas that form C_2 molecules in appreciable concentrations. Strong evidence of C_2 formation is found only in plasmas created from low laser energy density. At low laser energy densities, the ions and neutrals have slow speeds not optimum for forming a large concentration of sp^3 coordinated carbon. Given their higher mass than single carbon atoms, C_2 molecules travel slower than the bulk of the plume. Furthermore, upon interaction with the first monolayer, the C_2 molecule will dissociate. If a C_2 molecule had an incident energy of 100 eV, it will dissociate in to two carbon atoms each with a kinetic energy of 50 eV.

The energy barrier model is summarized as follows: The laser ablation of carbon produces neutral carbon atoms and ions. These ions and neutral atoms possess both large kinetic energy and excitation energy. Ions recombine within a monolayer, potentially to an excited electronic state. Electron excitation energy drives the conversion of sp^2 coordinated carbon atoms to sp^3 coordinated carbon atoms, as it effectively reduces the energy barrier needed to drive the $sp^2 \rightarrow sp^3$ reaction. The exchange of the electronic energy and kinetic energy affect the sp^3 fraction of the diamond-like carbon film. As the excitation energy exchange cross section

Table 4.2: Fit parameters determined from Raman spectra for different laser energy densities.

E_l (J/cm^2)	E_i (eV)	ω_{max} (cm^{-1})	Q	Γ
1.6	108.27	1536.04	-2.66	296.5
2.0	149.53	1541.11	-2.77	280.8
2.5	196.56	1550.76	-3.37	275.8
3.2	281.91	1582.38	-15.82	295.8

increases as kinetic energy decreases, slow atoms will lose their excitation energy and preferentially enter sp^2 coordination. As kinetic energy increases, less excitation energy will be lost, and thus, more carbon atoms will enter sp^3 coordination. However, the kinetic energy of the ions and neutral atoms cannot be increased indefinitely. Two factors will act to decrease the sp^3 fraction. First, damage increases as the ion and neutral atom kinetic energy increases. Second, increasing the kinetic energy increases the range. Thus, more collisions will occur in which excitation energy may be exchanged.

4.3 Results of Diamond-like Carbon Deposition at Varying Plasma Conditions

A set of undoped diamond-like carbon films is deposited on Silicon 100 substrates at different plasma conditions as described in Section 2.1. The laser energy densities were $1.6 J/cm^2$, $2.0 J/cm^2$, $2.5 J/cm^2$, and $3.2 J/cm^2$. The ordering of the sp^2 phase is determined by visible Raman spectroscopy. From the Raman data, the sp^3 fraction is estimated. Electron energy loss spectroscopy(EELS) is performed to directly determine the sp^3 fraction within the DLC films. Film density is also estimated from the EELS data. In this section, the visible Raman spectroscopy and electron energy-loss spectroscopy results are presented. These results are then discussed in terms of the energy barrier deposition model.

4.3.1 Raman Spectroscopy

Visible Raman spectra were taken on the diamond-like carbon films as described in Section 2.3. In each case, the G peak is fit with the Breit-Wigner-Fano(BWF) lineshape, given by Eq. 2.7. A plot of the Raman data and their fits are shown in Fig. 4.2. In some of the Raman spectra, a peak near $1555 cm^{-1}$ is visible. This is due to atmospheric oxygen. For each laser energy density, the BWF function is an excellent fit for the G peak. The residuals show no Raman D peak present. Therefore, since $I(D)/I(G) \approx 0$, the sp^2 phase within the DLC films is ordered in to chains, rather than in hexagonal rings to within the detection limits of the experiment.

The results of the BWF fit to the visible Raman G peak data are shown in Table 4.2. It shows the ion kinetic energy at the given laser energy density, ω_{max} as calculated by Eq. 2.8, the skewness parameter Q ,

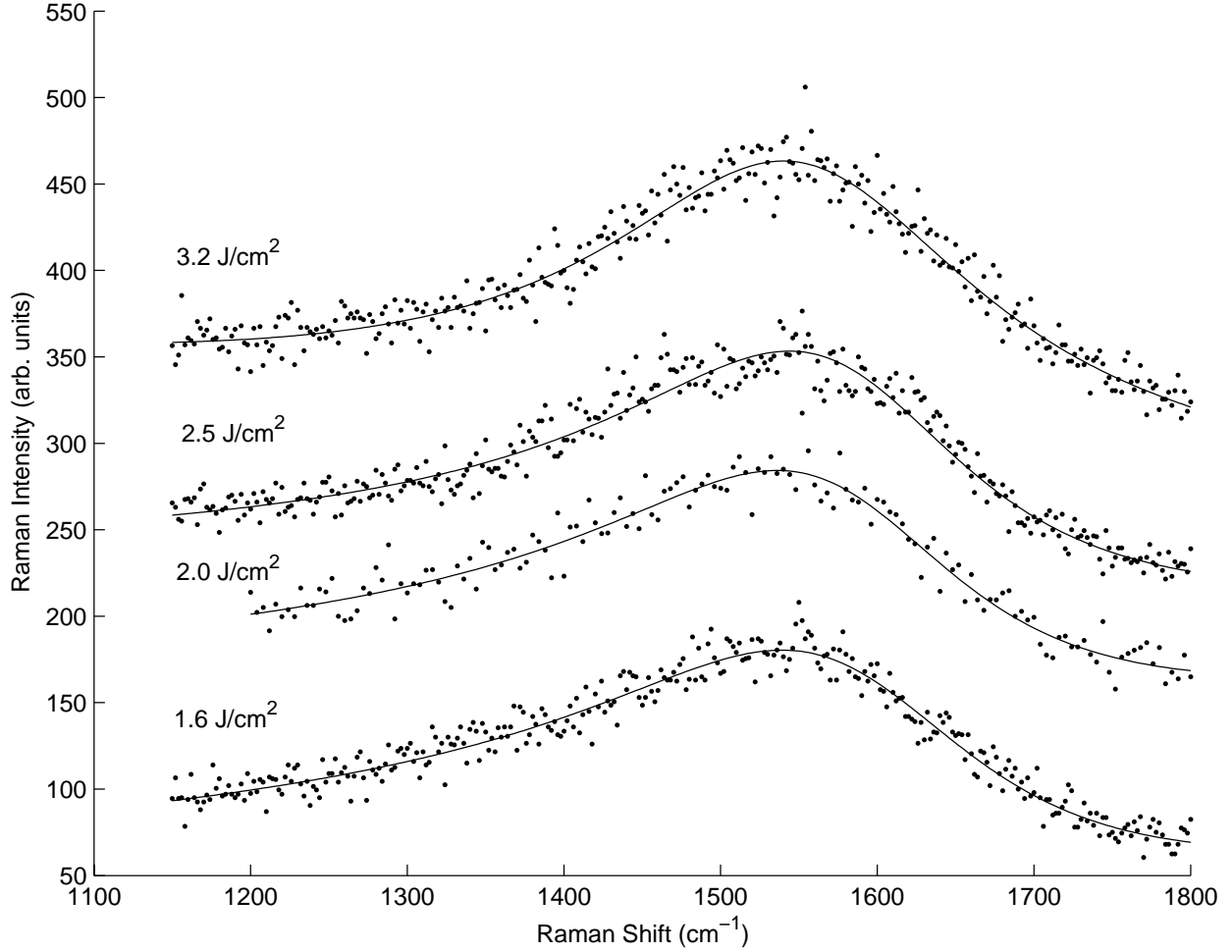


Figure 4.2: Raman spectra of $t-\alpha C$ films deposited at different laser energy densities. These different laser energy densities correspond to the kinetic energies of the Carbon ions within the plume.

and the full width at half maximum Γ . The value of the peak skewness, Q increases with increasing laser energy density. At the largest laser energy density, $3.2 J/cm^2$, the value of Q is large and negative. From the data of Praver, et al.[62] and Gilkes, et al.,[20], the sp^3 fraction for this film is ≈ 80 percent. For values of $Q < 10$, however, Q is not a strong function of the sp^3 fraction.[20] Thus, for those films with $Q \approx 3$, the sp^3 fraction is estimated to be between 10 and 50 percent. From the theory of Ferrari and Robertson, the full width at half maximum of the G peak, Γ , is expected to decrease with increasing sp^3 fraction as the distribution of sp^2 chain sizes becomes narrow.[2]

The G peak position, ω_{max} is used as a more quantitative estimate of the sp^3 fraction than either the peak skewness or the full width at half maximum. It is seen to disperse to higher wavenumbers as the sp^3 fraction increases.[2, 62, 20, 15] Ferrari and Robertson present a set of ω_{max} versus sp^3 fraction data from which estimation of the sp^3 fraction can be made. Data from the current work is also included, with the sp^3 fractions calculated from EELS results. This is shown in Fig. 4.3. Data from Ferrari and Robertson are

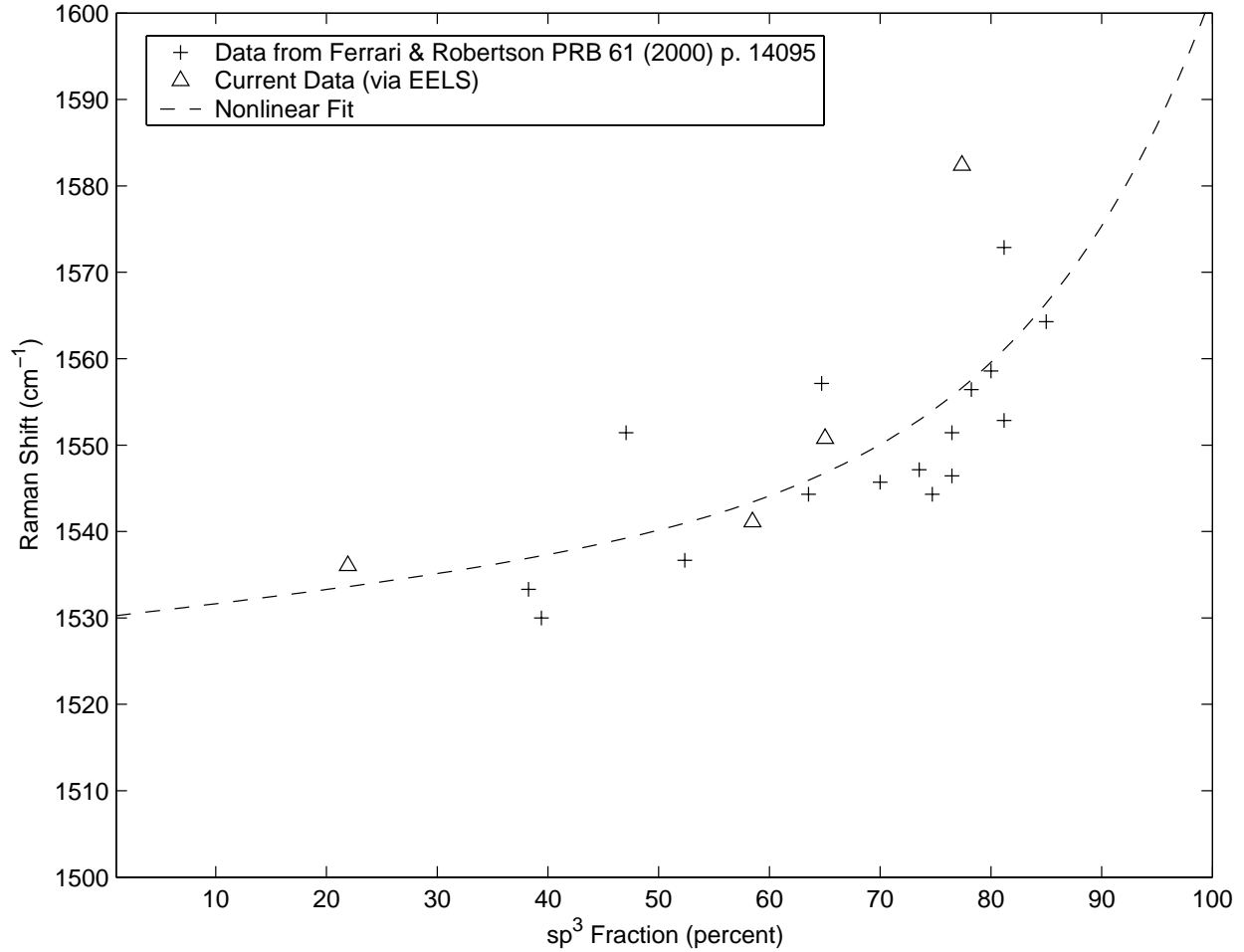


Figure 4.3: G peak position versus sp^3 fraction. Data is from Ferrari and Robertson, Phys. Rev. B 61 (2000) p. 14095 and from current work. A non-linear fit used for estimation of sp^3 fraction is shown.

shown with the + symbol and data from the current work shown by Δ . There is no a priori reason for using any particular fit to the data. It is found, however, that a linear fit yields impossible sp^3 fractions of greater than 100 percent. From the shape of Fig. 4.3, the G peak position increases linearly with sp^3 fraction until approximately 65 percent. After this, there is an exponential type increase. Thus, the relation between the G peak position and the sp^3 fraction is assumed to be of the form:

$$G = af + b + c \times \exp(df) \quad (4.16)$$

The exponential fit in Eq. 4.16 fits the data reasonably well. Ferrari and Robertson attribute the dispersion of the G peak to higher wavenumbers with increasing sp^3 fraction as due the change in microstructure from hexagonal rings to chains. Hexagonal sp^2 chains have higher vibrational frequencies than sp^2 rings.[2] However, the Raman fits shown no indication of the sp^2 phase ordering in to rings, as there was no discernable D peak in any case.

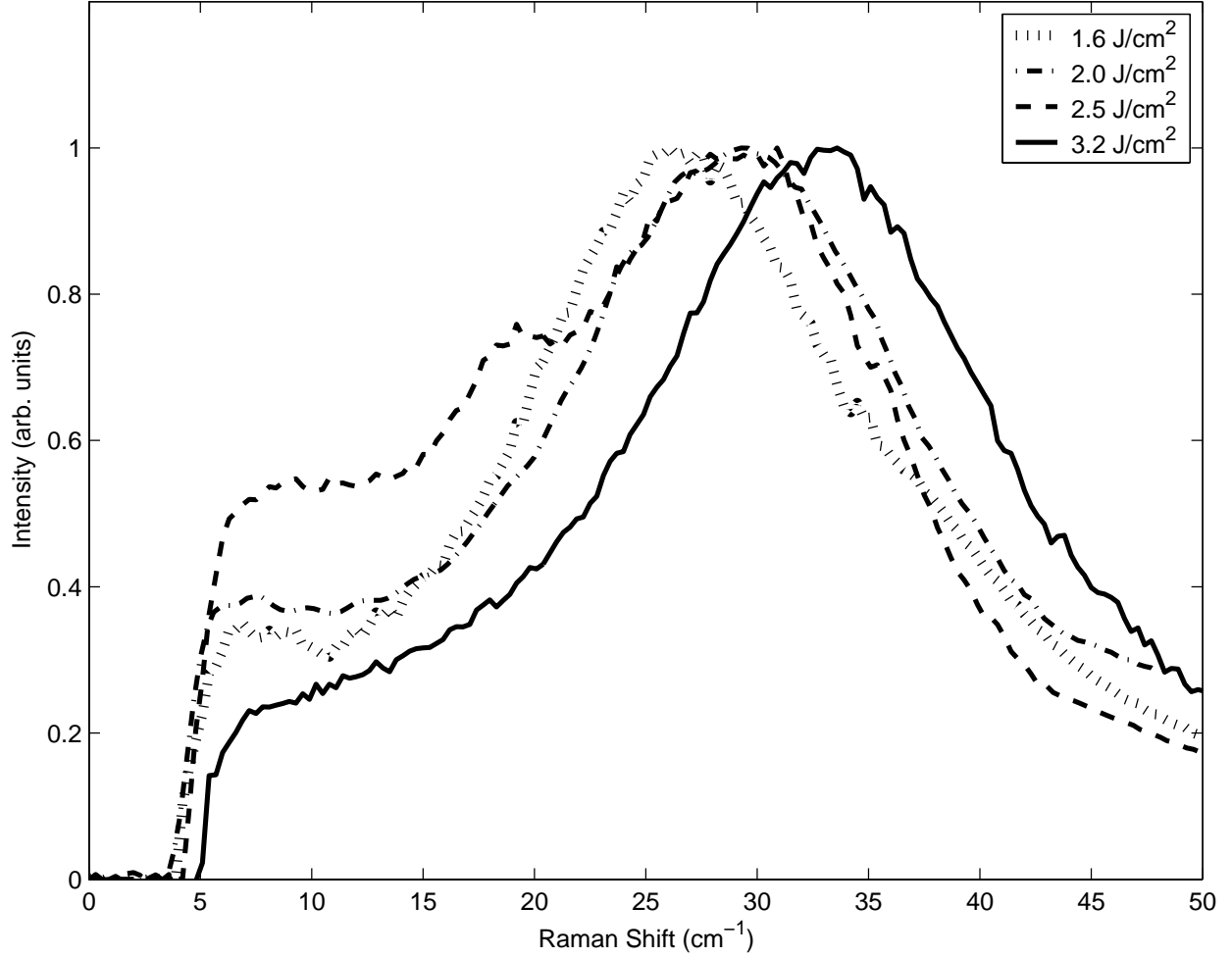


Figure 4.4: Low-loss spectra of $t - \alpha C$ films deposited at different laser energy densities. These different laser energy densities correspond to the kinetic energies of the carbon ions within the plume.

4.3.2 Electron Energy Loss Spectroscopy

Low Loss

Electron energy loss spectra in the low-loss region are shown in Fig. 4.4. A prominent plasmon peak between 25 eV and 35 eV is seen for films deposited at each laser energy density. In order to determine the plasmon energy, the peaks are fit using Eq. 2.2. In the case of the $2.5 J/cm^2$ deposition, there is a small silicon plasmon peak at approximately 18 eV due to incomplete removal of silicon during chemical polishing. The silicon plasmon peak is fit to Eq. 4.5 as well. No silicon K-edge was found in the EELS spectrum, indicating that a significant amount of silicon was not present. The results of the plasmon energy, and subsequently the density of deposited film, are shown in Fig. 4.5. Film density increases with increasing laser energy density.

A second interesting feature is seen in the low-loss spectra. There is a peak separate from the plasmon peak for those films deposited at $1.6 J/cm^2$, $2.0 J/cm^2$ and $2.5 J/cm^2$ located at $\approx 5 eV$. This feature

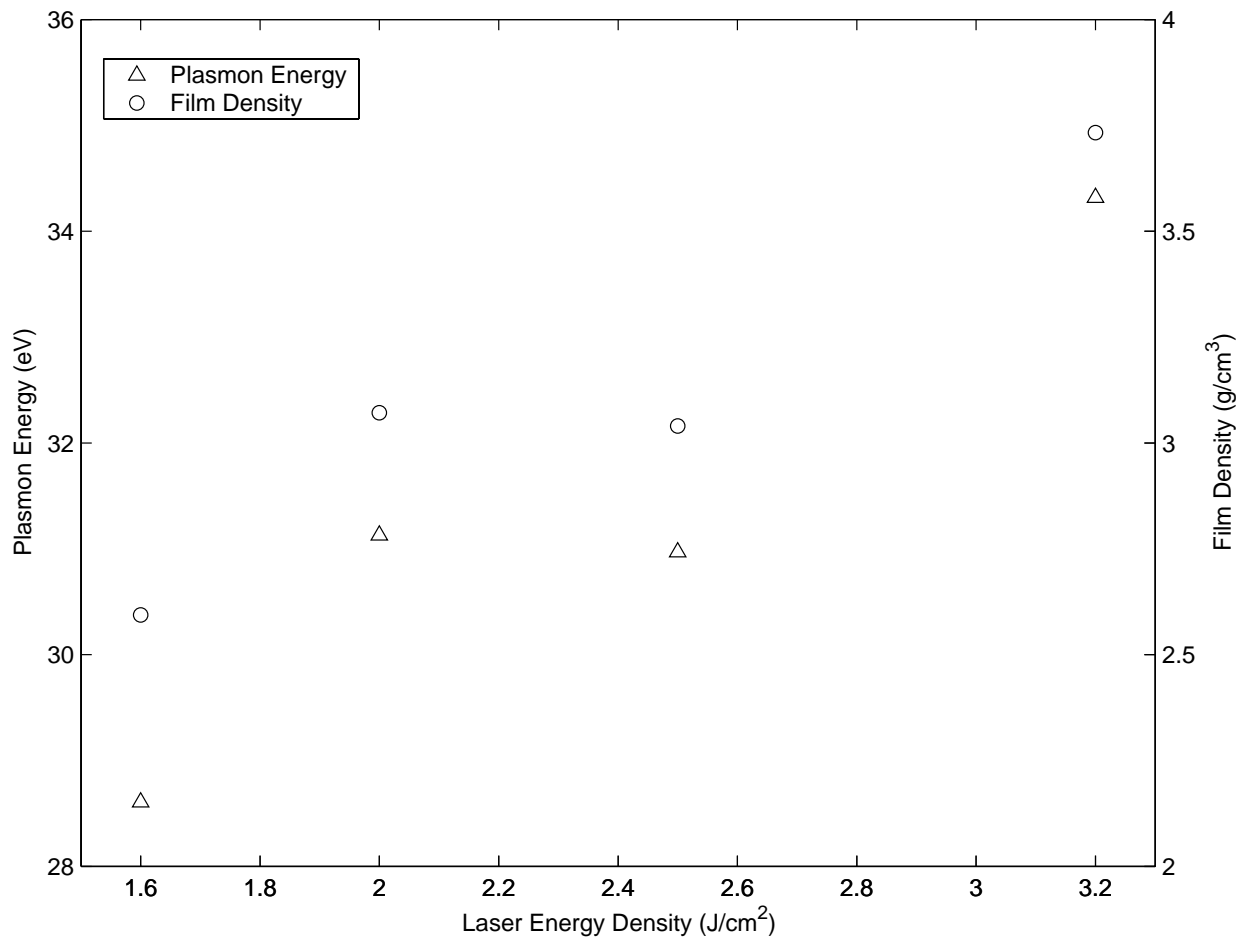


Figure 4.5: Plasmon energy and estimated film density as a function of laser energy density.

is not due to a surface plasmon. Rather, this feature is due to bonding-antibonding transitions. Incident electrons may lose energy by exciting a valence electron to an antibonding state. In diamond-like carbon, the possible transitions are $\pi \rightarrow \pi^*$, $\pi \rightarrow \sigma^*$, $\sigma \rightarrow \pi^*$, and $\sigma \rightarrow \sigma^*$. The $\sigma \rightarrow \sigma^*$ excitation has an energy between 10 eV and 13 eV.[9]

High Loss

As-deposited diamond-like carbon films are prepared through the chemical polishing technique as described in the experimental section. Single-scattering spectra are deconvolved from the raw spectrum using Fourier-log deconvolution. The carbon K-edge single scattering spectra of the deposited, undoped, diamond-like carbon films are shown in Fig. 4.6.

The π^* and σ^* feature from transitions from the $1s$ state to the π^* and σ^* antibonding states, respectively, are clearly visible. As the laser energy density increases, the π^* peak changes from a distinct peak with nearly half the magnitude of the σ^* peak to a weak shoulder on the σ^* peak. As sp^2 states contribute to the π^*

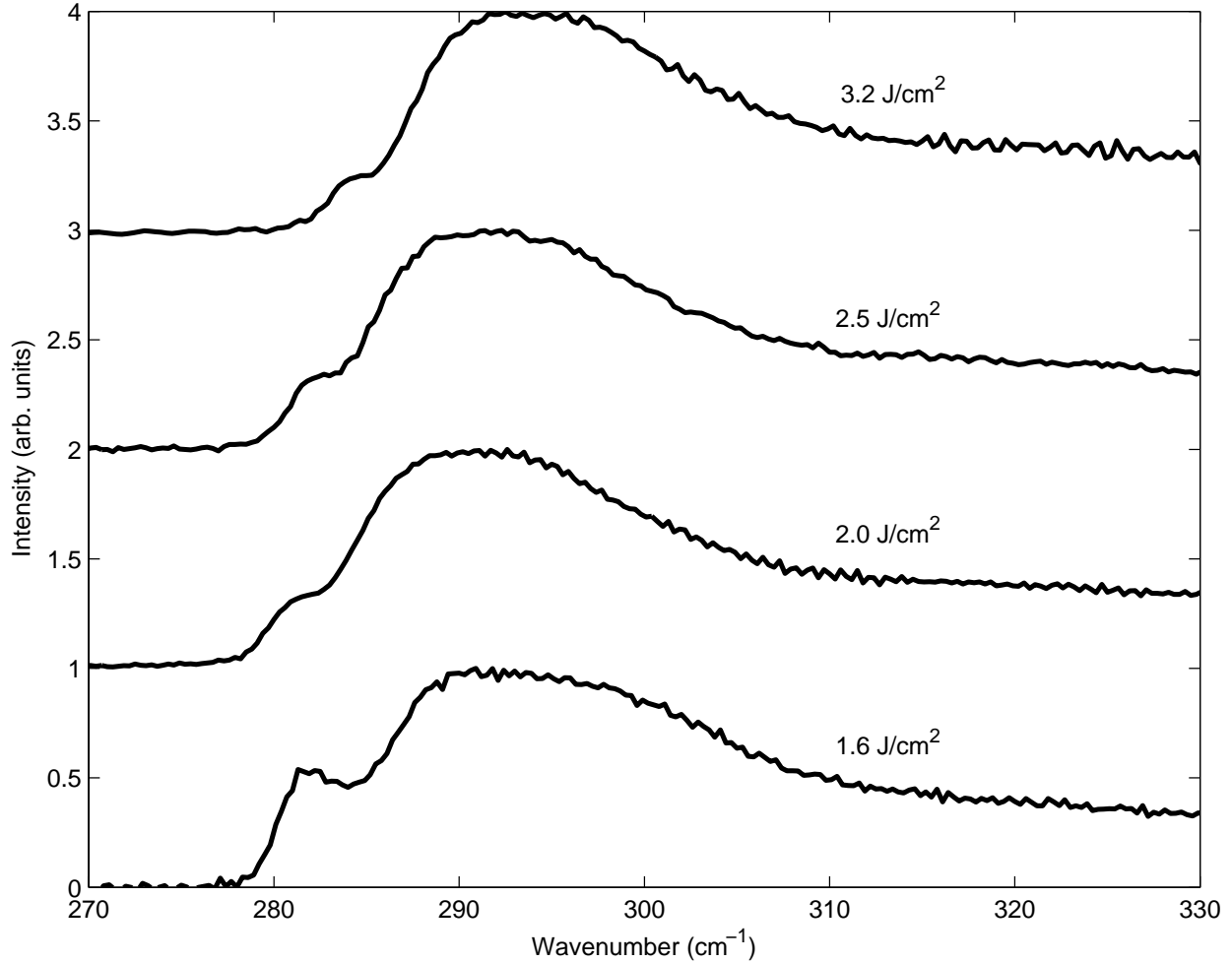


Figure 4.6: High-loss spectra of $t - \alpha C$ films deposited at different laser energy densities.

intensity and sp^3 states do not, the relative decrease in π^* intensity is an indication that the fraction of sp^2 coordinated carbon is decreasing as laser energy density increases. There also appears to be a slight shift in the location of the start of the K-edge peaks with increasing laser energy density. This is likely due to the deconvolution method. However, it is possible for shifts in the $1s$ shell energy to occur with different bonding types. The sp^3 fraction is quantified from the carbon K-edge spectra as discussed in the Experimental section with Eq. 2.4. An estimate of the sp^3 fraction is taken from the visible Raman spectra as discussed previously. A plot of the sp^3 fraction as a function of the laser energy density is shown in Fig. 4.7.

4.3.3 Discussion in Terms of Energy Barrier Model

The relationship between sp^3 fraction and ion kinetic energy is shown in Fig. 4.7. It shows that the sp^3 fraction increases approximately logarithmically with laser energy density on target. From this work and

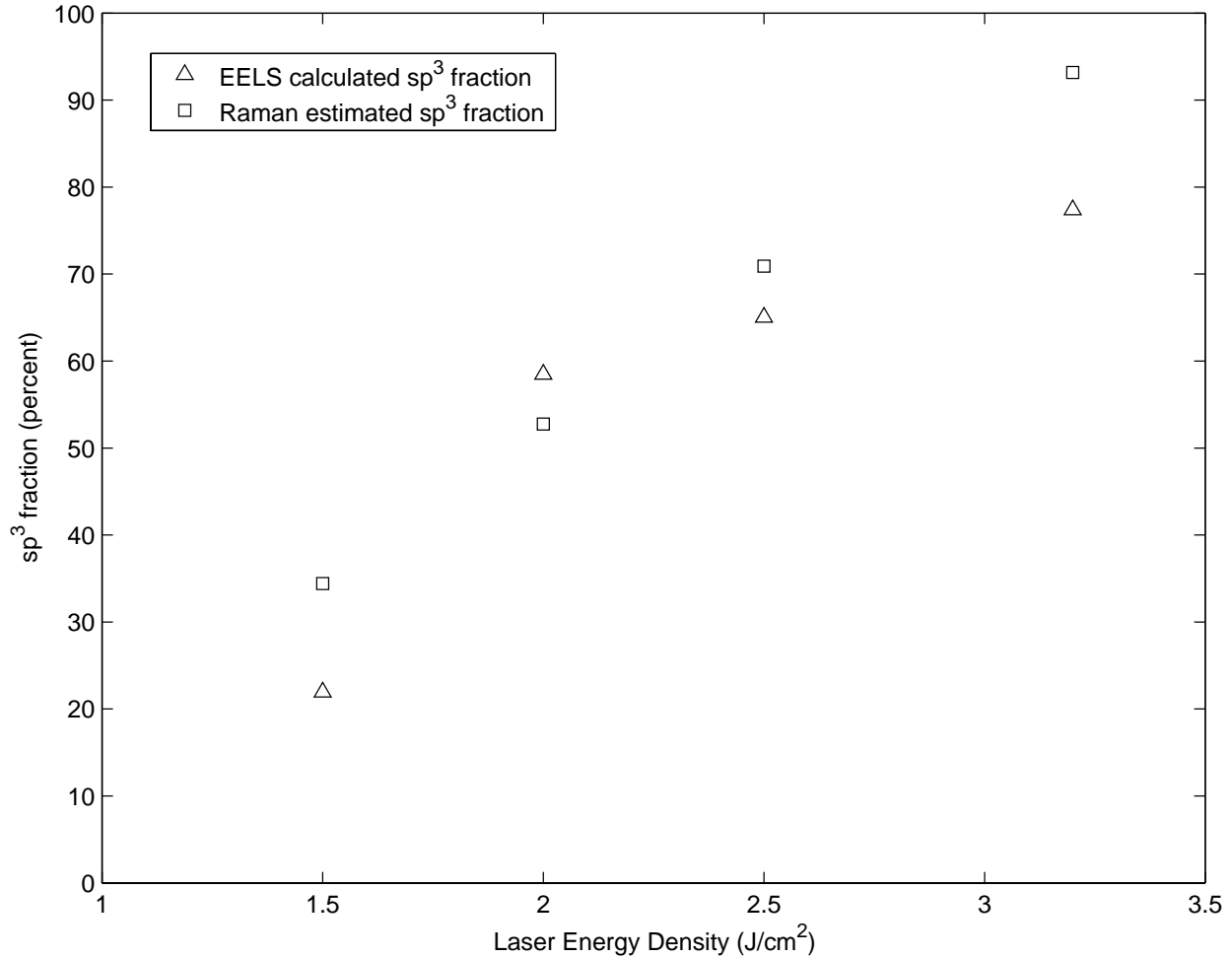


Figure 4.7: sp^3 fractions as a function of laser energy density as calculated by electron energy loss spectroscopy and by Raman spectroscopy.

the previous work, it is known how the plasma properties change as the laser energy density is changed. At the smallest laser energy density used, $1.6 J/cm^2$, the electron temperatures, flow speeds, and densities are the smallest present in the experiment. The plasma plume possesses a larger ionization fraction than those plumes created at higher laser energy densities. However, the neutral particles are still the dominant (> 90%) plume constituent. It is their velocity which is most important when describing how their electronic excitation energy will be transferred as the incident atom interacts with the previously deposited atoms. Ions upon capture are neutralized in to excited states. Lower velocities mean an increased collision time during which electronic excitation may be exchanged. At low laser energy densities, it is known that C_2 populations are present, especially at the periphery of the plasma.[99] Dicarbon, with its heavier mass, is slower, and will dissociate on impact to form two carbon atoms with half the initial energy.

The particle kinetic energies at the lowest laser energy densities are not large, thus, the number of displacements per atom is small. Chains of sp^2 atoms with a variety of sizes may form under these conditions.

The presence of a large distribution of chain sizes at this lowest laser energy density is seen in the Raman spectroscopy results. Large chains, with their distributed π bonds, have smaller force constants than shorter chains whose π bonds are not as delocalized. This means that the Raman shift is small. Plasmon results indicate that the smallest mass density of the DLC films was formed at the lowest laser energy density. Given that the bonding of sp^2 atoms is two-dimensional, a population of sp^2 coordinated atoms is less efficient at filling space than sp^3 coordinated atoms with their three-dimensional bonding. The presence of an electronic transition peak *eg.* ($\pi \rightarrow \pi^*$) in the low-loss spectrum is also an indication of a significant number of π states, and thus a large fraction of sp^2 coordinated carbon atoms.

As laser energy density is increased, a number of different phenomena occur. First, the presence of C_2 , with its slow flow speed, is reduced.[99] The flow speeds and densities increase, although the ionization fraction decreases. Neutrals are still the dominant plume constituent. The increased flow speeds, and thus particle kinetic energies, mean that they have a smaller probability of energy transfer during collisions. The number of collisions does not greatly increase, from one to two at the lowest laser energy density, to between two to three at the higher laser energy densities. Given the exponential relationship between sp^3 coordination probability and electronic excitation energy, only slight changes in electronic excitation energy yield large changes in film sp^3 fraction. Also, the electron temperature increases, and thus a larger population of excited states, and excited states of higher energies, exist. Carbon atoms with sufficiently large excitations may form two sp^3 coordinated carbon atoms as they interact with the film via conversion of an existing sp^2 site in to an sp^3 site.

The sp^2 chain size distribution narrows because there are simply more sp^3 coordinated carbon atoms present, and because the amount of displacements per atom is increasing as the particle kinetic energy increases. Plasmon results indicate that the density of the DLC film increases as laser energy density is increased. The increase in the sp^3 fraction drives this increase in density, not the reverse as posited by Robertson.[85, 93] The sp^3 sites have a smaller atomic volume than sp^2 sites, and thus, along with their ability to form a three dimensional network, act to increase density.[16] Increased compressive stress arises as new sp^3 sites form and are incorporated in to the three dimensional network. As the number of sp^3 coordinated carbon atoms increases, this becomes more difficult, and thus stress increases with sp^3 fraction. In the low-loss EELS results, the electronic transition peak becomes smaller as the number of π states decreases. The Raman shift increases as sp^3 chain size decreases, and thus the π bonds become more localized, increasing the bond strength.

At the largest laser energy density used in this experiment, the flow speeds, electron temperatures, and particle densities are also the largest present in this experiment. This is also the location of the largest sp^3 fraction and DLC film density. As the production of sp^3 coordinated carbon atoms is a maximum here, the excitation and particle energy conditions are likely optimized at this point. Given the kinetic energy of the ions, the number of displacements created by the incident particles is more than one displacement per atom. The surface layer is the most likely to be damaged. Incident carbon atoms will most likely displace these

atoms, since they have not yet collided with anything to lose their kinetic energy. Further displacements will then be of sp^2 sites, resulting in no net change in the sp^3 fraction due to damage. The effect of displacements creates a maximum sp^3 fraction at a certain kinetic energy of particles, less than 100 percent. If laser energy density were increased further, then damage of the sp^3 component will occur more often than creation of new sp^3 sites. Film stress will begin to decrease, as will the Raman shift, as fewer sp^3 sites are created and graphitization occurs. Significant graphitization occurs when the incident atom range is such that their excitation energy is completely lost before they are slowed and captured.

Chapter 5

Magnetically Assisted Pulsed Laser Deposition

Magnetically assisted pulsed laser deposition has been suggested as a means of removing the macroscopic neutral components within the plume and changing the energetics of the species within the plume. A magnetic field is created perpendicular to the plume flow direction via two NdFeB magnets. The interaction of the plasma with the magnetic field may cause the charged components to be deflected whereas neutral atoms are unaffected. It is reasonable to assume that the neutrals are unaffected if momentum transfer from the charged to neutral components is negligible. Interest in the interaction of laser produced plasmas with magnetic fields is not solely due to materials processing.[100, 39] Researchers in the fields of inertial confinement fusion and astrophysical plasmas have investigated the manner in which plasma plumes interact with magnetic fields. [46, 40, 42, 44, 43, 45, 49]

A series of experiments has been undertaken to investigate the effect of an external magnetic field on the laser ablation plasma and the deposited hydrogen-free diamond-like carbon film. The plasma is studied using Langmuir probes and magnetic probes. Corrections to the quadrupole Langmuir probe equations due to the magnetic field are derived. A hydrogen-free diamond-like carbon film is deposited under magnetized conditions and investigated with electron energy-loss spectroscopy.

5.1 Corrections to Langmuir Probe in Magnetic Field

Earlier analysis of the Langmuir probe signals was derived from standard probe theory of ion and electron collection.[65, 24] The addition of a magnetic field to the plasma affects the motion of ions and electrons within the plasma. Therefore, it is necessary to modify the probe equations due to the influence of the magnetic field. If the magnetic field is weak, collection of electrons and ions by the probe is unaffected, and the probe equations for unmagnetized plasmas may be used. The magnetic field is considered weak if the ion and electron Larmor radii are much larger than the probe radius. If the magnetic field is strong such that the ion and electron Larmor radii are smaller than the probe radius, both ions and electrons must diffuse across the magnetic field to be collected.[66] An intermediate case occurs when the ion Larmor radius is much larger than the probe radius, but the electron Larmor radius is smaller than the probe radius.

For the pulsed laser deposition plasmas found in these experiments, the ion Larmor radius is much greater than the probe radius. As an example, the ion Larmor radius in a typical magnetized PLD plasma with a magnetic field of 0.4 T, and a typical plume flow speed of 5×10^4 m/s is ≈ 1.56 cm. The Langmuir probe radius is 0.025 cm, therefore, the ion saturation current is unaffected by the applied magnetic field. However, the electron Larmor radius calculated with a representative plume flow speed of 5×10^4 m/s is $\approx 7.1 \times 10^{-5}$ cm. Therefore it is not possible to assume that electron current to the probe tips are unaffected by the applied magnetic field. A correction for the effects of the magnetic field on the electron current is necessary.

In a series of papers, Laframboise and Rubinstein present a rigorous theory for the impact of applied magnetic fields on electron collection by cylindrical Langmuir probes. [69, 70] They considered a population of electrons with a Maxwellian velocity distribution. The motion of these electrons under the influence of a magnetic field is derived from classical mechanics. The electron current collected is from those electrons which intersect the probe. Their theory assumes that the plasma is collisionless, and that all electrons which intersect the probe are collected. The calculation of electron temperature from the quadrupole probe, using the theory of Laframboise and Rubinstein, is described herein. The set of derived equations assumes that all electrons incident on the probe are collected, and that the sheath is collisionless. This is verified by investigating the collision frequency and the electron cyclotron frequency. The effects of cyclotron motion must be important, or more quantitatively, greater in magnitude, than collisional effects. The electron-ion and electron-neutral collision frequency are the most important, as they result in net diffusion of electrons. The electron-electron and electron-ion collision frequency are not different to more than an order of magnitude under the assumption of quasineutrality, which is assumed here.[47] If the collision frequency is much less than the cyclotron frequency $\Omega_e = qB/m_e$, $\nu_{ei}/\Omega_e \ll 1$ and $\nu_{en}/\Omega_e \ll 1$, then cyclotron motion dominates over collisional effects. The electron-ion collision frequency is:

$$\nu_{ei} = \frac{2^{1/2} n_i Z^2 e^4 \ln \Lambda}{12 \pi^{3/2} \epsilon_0^2 m_e^{1/2} T_e^{3/2}} \quad (5.1)$$

where ν_{ei} is the electron-ion collision frequency, n_i is the ion density, Z is the average charge state of the plasma, e is the charge on a proton, m_e is the electron mass, and T_e is the electron temperature. The natural log of Λ , $\ln \Lambda$ is:

$$\ln \lambda = \ln \left(\frac{12 \pi}{Z} n_i \left(\frac{\epsilon_0 k T_e}{n_e e^2} \right)^{3/2} \right) \quad (5.2)$$

It will be shown later than at 2 cm Langmuir probe position, a typical density is 10^{18} m⁻³ and a typical electron temperature is 40 eV. This gives $\ln \lambda \approx 15$. Substituting these values in to Eq. 5.1, the ratio of the electron-ion collision frequency to the electron cyclotron frequency is:

$$\frac{\nu_{ei}}{\Omega_e} = \frac{\nu_{ei}}{\frac{qB}{m_e}} \approx \frac{172 \times 10^3 \text{ Hz}}{7 \times 10^{10} \text{ Hz}} \approx 2.5 \times 10^{-6} \ll 1 \quad (5.3)$$

For neutrals, $\nu_{en}/\Omega_e \ll 1$ must be true. The electron-neutral collision frequency is

$$\nu_{en} = n_n v_{th,e} \sigma_{en} \quad (5.4)$$

In Eq. 5.4, n_n is the neutral particle density, $v_{th,e}$ is the electron thermal speed, and σ_{en} is the cross section for electron-neutral collisions. The cross section for electron-neutral collisions is:

$$\sigma_{en} = \frac{2}{3}\pi R^2 \quad (5.5)$$

where R is the atomic radius of carbon, 77 \AA . The electron-neutral collision frequency is estimated assuming that the neutral atom density is unaffected by the presence of the magnetic field. This assumes that once the magnetic field begins to influence the path of the ions, the momentum transfer between ions and neutral atoms is insignificant. With the neutral particle density calculated in Chapter 3 ($n_n \approx 10^{21} m^{-3}$) and $kT_e = 40 \text{ eV}$ as will be found in the results of this chapter, the electron-neutral collision frequency is $32.86 \times 10^6 \text{ Hz}$. Thus:

$$\frac{\nu_{en}}{\Omega_e} = \frac{32.86 \times 10^6 \text{ Hz}}{7 \times 10^{10} \text{ Hz}} \approx 4.69 \times 10^{-4} \ll 1 \quad (5.6)$$

Thus, the use of a collisionless model to determine the effects of the magnetic field on electron collection is valid.

A quadruple Langmuir probe consists of a double probe and a floating probe as shown in Fig. 2.7 was used. The probe is biased such that probe tips 3 and 4 operate in ion saturation, while probe tip 2 is at the floating potential, and tip 1 lies along the repelling region of the probe characteristic. Probe tip 4 is used for flow speed calculations in certian magnetic flows.[101] Although not used for this purpose in this research, it still collects current and must be accounted for in the probe equations.

Probe tip 2 is floating, thus the electron and ion currents to this probe are equal, thus:

$$A_{e2}J_{e2} = A_{i2}J_{i2} \quad (5.7)$$

The sum of the currents in probe tips 1, 3, and 4 are zero, thus:

$$A_{i3}J_{i3} - A_{e3}J_{e3} + A_{i4}J_{i4} - A_{e4}J_{e4} + A_{i1}J_{i1} - A_{e1}J_{e1} = 0 \quad (5.8)$$

Probe tips 3 and 4 operates in ion saturation, thus the electron current collected by probe 3 is equal to zero, $J_{e3} = J_{e4} = 0$. For probe tips 1,2, and 3, the collection area for ions and electrons are identical, with and area of $A = 4 \times 10^{-6} m^2$. Probe tip 4 is perpindicular to the flow direction. The collection area is corrected for supersonic flow past the tip. The ions only see the projected area of the probe tip, A/π . The areas A are eliminated from Eqs. 5.7 and 5.8.

The ion saturation current is assumed to be unaffected by the probe potential. This is a reasonable assumption, provided that the ion kinetic energy is much greater than the probe potential. Ion kinetic energies have been found to be in excess of 100 eV for these plumes, thus satisfying this condition.[24, 102] Furthermore, ion saturation current is unaffected by the magnetic field, since the Larmor radius for ions is much greater than probe dimensions. If J_i is the ion saturation current density to the probe tips, Eqs. 5.8 and 5.7 have the following form:

$$J_{e1} = AJ_i (2 + 1/\pi) \quad (5.9)$$

and

$$J_i = J_{e2} \quad (5.10)$$

Substitution of Eq. 5.10 into Eq. 5.9 gives:

$$(2 + 1/\pi) = \frac{J_{e1}}{J_{e2}} \quad (5.11)$$

Rubinstein and Laframboise give the upper bound on the dimensionless current collected by a Langmuir probe at an angle θ with respect to the magnetic field direction. [70]

$$i = \left[\frac{2}{\pi} (1 - \chi_P) \sin\theta + \frac{1}{\pi\beta} (3 - 2\chi_P) \right] \exp(\chi_P) \quad (5.12)$$

In Eq. 5.12, χ_P , the dimensionless potential, is $-qV/kT_e$, θ is the probe angle with respect to the magnetic field, β is the ratio of the probe radius, r_P to the electron Larmor radius, r_{Le} , and i is the dimensionless current. The dimensionless current i is the ratio of the probe current per unit length to the random thermal current per unit length, $i = I/r_P n_e v_{th,e}$, where $v_{th,e}$ is the electron thermal speed.

As a means of temperature estimation, it is assumed that the current per unit length is not a function of position along the Langmuir probe, and that the probe is aligned perpendicular to the magnetic field, such that $\sin\theta = 1$. Equation 5.12 is substituted into Eq. 5.11, and upon manipulation, the following expression is derived:

$$2 + 1/\pi = \exp(\chi_1 - \chi_2) \frac{\frac{2}{\pi} + \frac{3}{\pi\beta} - \chi_1 \left(\frac{2}{\pi} + \frac{2}{\pi\beta} \right)}{\frac{2}{\pi} + \frac{3}{\pi\beta} - \chi_2 \left(\frac{2}{\pi} + \frac{2}{\pi\beta} \right)} \quad (5.13)$$

In Eq. 5.13, the dimensionless potential for probe tip j is $-e(V_j - V_P)/kT_e$ where V_j is the potential on probe j and V_P is the plasma potential. Further manipulation of Eq. 5.13 gives

$$\ln(2 + 1/\pi) = \chi_1 - \chi_2 + \ln \left(\frac{2\beta + 3 - \chi_1(2\beta + 2)}{2\beta + 3 - \chi_2(2\beta + 2)} \right) \quad (5.14)$$

The third term on the right hand side represents a correction due to the magnetic field. In the weak field limit, $\beta \rightarrow 0$, this third term becomes:

$$\ln \left(\frac{3 - 2\chi_1}{3 - 2\chi_2} \right) \quad (5.15)$$

However, this is not the same result that is derived for an unmagnetized plasma. In that case, it is expected that the third term of Eq. 5.14 would be zero, leaving the standard equation for the calculation of electron temperature in the unmagnetized case. It must be noted that Eq. 5.12 predicts an infinite current drawn in the $\beta \rightarrow 0$ limit. Thus, it cannot be expected that Eq. 5.14 will yield accurate results as $\beta \rightarrow 0$. Note also that in the $\beta \rightarrow 0$ limit, the condition in Eq. 5.3 is no longer satisfied, and thus Eq. 5.12 can no longer be used.

For the strong field limit, with the Larmor radius much smaller than the probe radius: $\beta \rightarrow \infty$, Eq. 5.14 becomes:

$$\ln(2 + 1/\pi) = \chi_1 - \chi_2 + \ln \left(\frac{\chi_2 - \chi_1}{1 - \chi_2} + 1 \right) \quad (5.16)$$

Electron temperature is estimated from Eq. 5.16 provided that the plasma potential is known. Plasma potential is calculated by setting electron current equal to the ion current. In this case both the flow and magnetic field must be considered in the calculation of the plasma potential. The ion current is assumed to be due to ions crossing the sheath with the Bohm velocity and the contribution due to supersonic flow.[24, 67, 65]

$$I_i = n_i 0.61 e A \left(\frac{k T_e}{m_i} \right)^{1/2} + n_i e A_{\perp} u \quad (5.17)$$

As previously assumed, ion collection is not significantly perturbed by the magnetic field. The dimensionless electron current per unit length is given by Eq. 5.12. Restoring dimensions, and assuming properties to be constant over the probe tip length gives:

$$I_e = L_p r_p n_e \left(\frac{2\pi k T_e}{m_e} \right)^{1/2} e^{\chi_2} \left[\frac{2}{\pi} (1 - \chi_2) + \frac{1}{\pi\beta} (3 - 2\chi_2) \right] \quad (5.18)$$

Equating Eq. 5.18 and Eq. 5.17 and taking the large magnetic field limit, one finds:

$$\frac{n_i 0.61 e A \left(\frac{k T_e}{m_i} \right)^{1/2} + n_i e A_{\perp} u}{L_p r_p n_e \left(\frac{2\pi k T_e}{m_e} \right)^{1/2}} = e^{\chi_2} \left[\frac{2}{\pi} (1 - \chi_2) \right] \quad (5.19)$$

The electron temperature may now be estimated using an iterative procedure. First, the electron temperature is estimated using temperature relation in the case of no magnetic field.

$$T_e^{est} = \frac{V_1 - V_2}{\ln(2 + 1/\pi)} \quad (5.20)$$

Second, the plasma potential V_P is calculated from the floating voltage signal recorded from tip 2 with Eq. 5.19. Third, the electron temperature is calculated using Eq. 5.16. The second and third steps are iterated until convergence on the peak temperature. To reduce computation time, only a sample of points from the V_{12} and V_{2g} data are used to calculate T_e .

A sample plot showing the electron temperature at the 3 *cm* Langmuir probe position calculated from the unmagnetized equation (Eq. 2.18) and the magnetized equations for data recorded at a laser energy of 550 *mJ* and a spot size of 0.22 *cm*² is shown in Fig. 5.1. Utilizing a formula for the electron temperature in unmagnetized plasmas will overestimate the electron temperature. In general, the electron temperature is proportional to the inverse of the slope of the Langmuir probe $I - V$ characteristic. Probe tips 1 and 2 lie along this slope, and thus act as a means of estimating the shape of the $I - V$ characteristic without having to sweep the voltage. The effect of the magnetic field is to create an apparent reduction in the slope of the $I - V$ characteristic. Some fraction of the population of electrons that would have otherwise been collected by the probe will follow their Larmor radii out of the sheath and back into the plasma bulk. The reduction in the slope of the Langmuir probe characteristic will cause the unmagnetized electron temperature formula, Eq. 5.20, to overestimate the temperature.

Figure 5.1 shows the estimated electron temperature in the strong magnetic field limit, $\beta \rightarrow \infty$. If the ratio of probe radius to electron Larmor radius β is kept in the analysis, Eq. 5.16 becomes:

$$\ln(2 + 1/\pi) = \chi_1 - \chi_2 + \ln \left(\frac{\chi_2 - \chi_1}{\frac{2\beta+3}{2\beta+2} - \chi_2} + 1 \right) \quad (5.21)$$

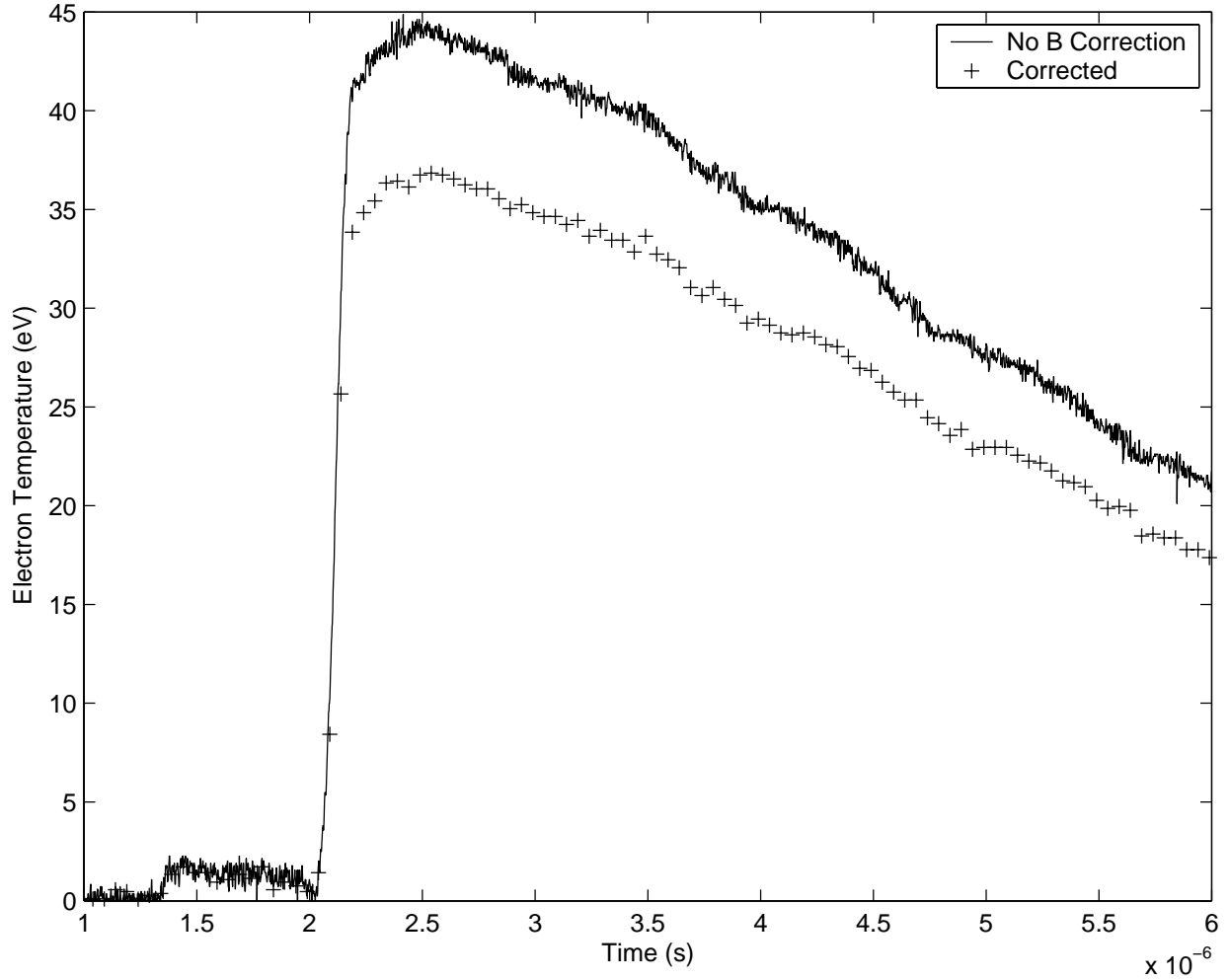


Figure 5.1: Electron temperature at the 3 cm. Langmuir probe position, with and without magnetic field correction. Laser Energy 550 mJ. Lens position 12 cm.

Given an electron temperature from Fig. 5.1 of $\approx 30 \text{ eV}$, the electron Larmor radius is $\approx 0.0036 \text{ cm}$. This yields $\beta \approx 7$. The fraction $\frac{2\beta+3}{2\beta+2}$ is ≈ 1.06 . The correction to the electron temperature found from Eq. 5.21 is not very significant. However, the presence of a finite β also affects the plasma potential calculated by Eq. 5.19. The effect of the second term in the brackets of Eq. 5.18 is minimal, since $1/\pi\beta \approx 0.05$. Thus, the effect of finite β on the estimated electron temperatures calculated in the large β limit is not significant for these plasmas.

Once the electron temperature is determined, the ion density is calculated as in the unmagnetized case.[24, 67, 65] As stated previously, ion current to the probe tip operating in ion saturation is assumed to be the sum of the current due to supersonic flow and the current due to those ions which cross the sheath with the

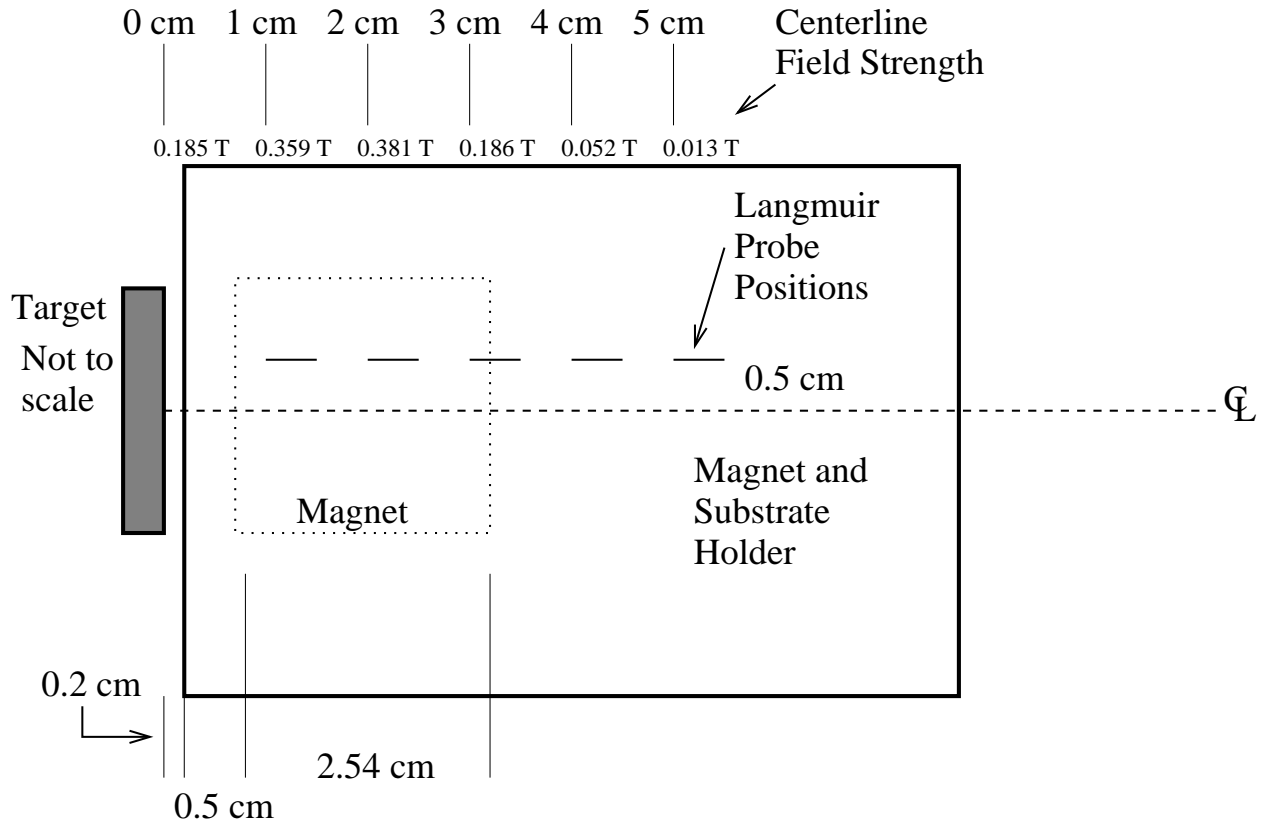


Figure 5.2: Geometry of the target, magnet holder, and Langmuir/ \hat{B} probes. The target and magnet holder are not to scale. The positions of the magnets and the probe positions are to scale.

Bohm velocity. Thus, the ion density, n_i calculated from the voltage V_{i3} across a 10Ω resistor is:

$$n_i = \frac{\frac{V_{i3}}{10\Omega}}{0.61eA \left(\frac{kT_e}{m_i}\right)^{1/2} + eA_{\perp}u} \quad (5.22)$$

5.2 Dynamics of Laser Produced Plasma in Magnetic Field

5.2.1 Flow Speed Calculation

The flow speed of the plasma may be altered due to the presence of the magnetic field. Specifically, if the plasma displaces the magnetic field, it may do so at the expense of its kinetic energy or its thermal energy. There is some indication that the plasma is limited to the $E \times B$ velocity across the magnetic field.[42] Charge separation may occur due to finite ion Larmor radius effects. The ion Larmor radius is not small compared to the device size, whereas the electron Larmor radius is much smaller than the device size. Charge separation may then occur, leading to the development of an electric field. In previous research, ion flow speeds were calculated by observing the arrival time at different Langmuir probe positions of self-similar regions of the ion saturation signal.[24] However, the ion saturation signal is significantly noisier under the

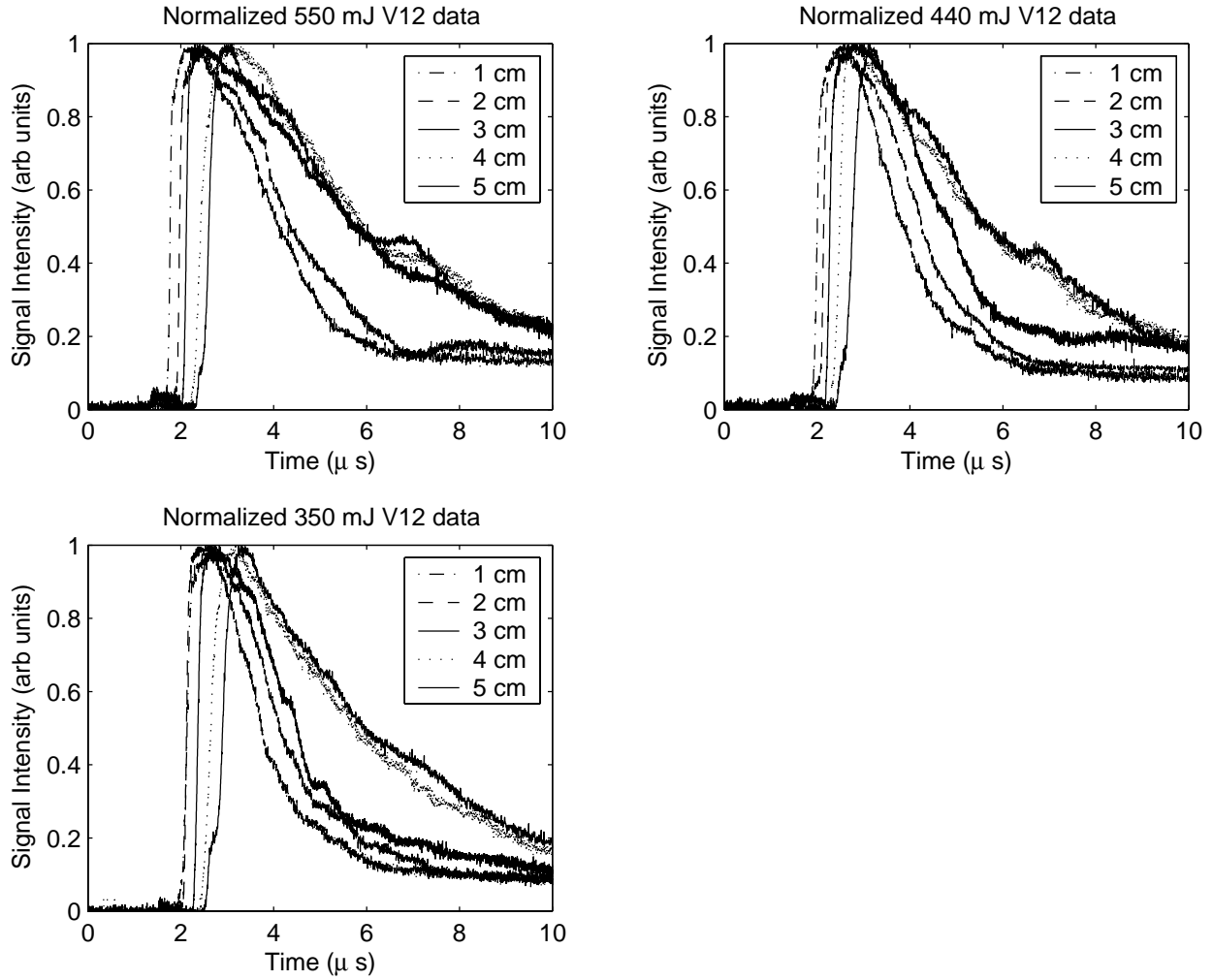


Figure 5.3: Normalized V_{12} data as a function of Langmuir probe position for different laser energies.

presence of the magnetic field. A complete discussion of the ion saturation signal follows in a later section.

With the significant noise on the ion saturation signal, the arrival time of the signal proportional to electron temperature, V_{12} , is used. This signal includes contributions from both ions and electrons, thus the flow speed measured in this section is considered to be the bulk plasma flow speed. For simplicity the V_{12} signal is assumed to be collected at the Langmuir probe tip. In previous research, a density averaged collection position was used. However, the density profile in the magnetized plume is not known, therefore such an average is not possible. The raw V_{12} data are normalized to the peak voltage for each laser energy density and position. Examples of the normalized V_{12} data is shown in Fig. 5.3.

At 550 mJ and 440 mJ, there is clear separation between the arrival of the V_{12} signal for all positions. However, at 350 mJ, the arrival time for the V_{12} signal at the one and two centimeter Langmuir probe positions is indistinguishable. For positions farther than two centimeters from the target, the normalized V_{12} data shows clear distinction between arrival time and position.

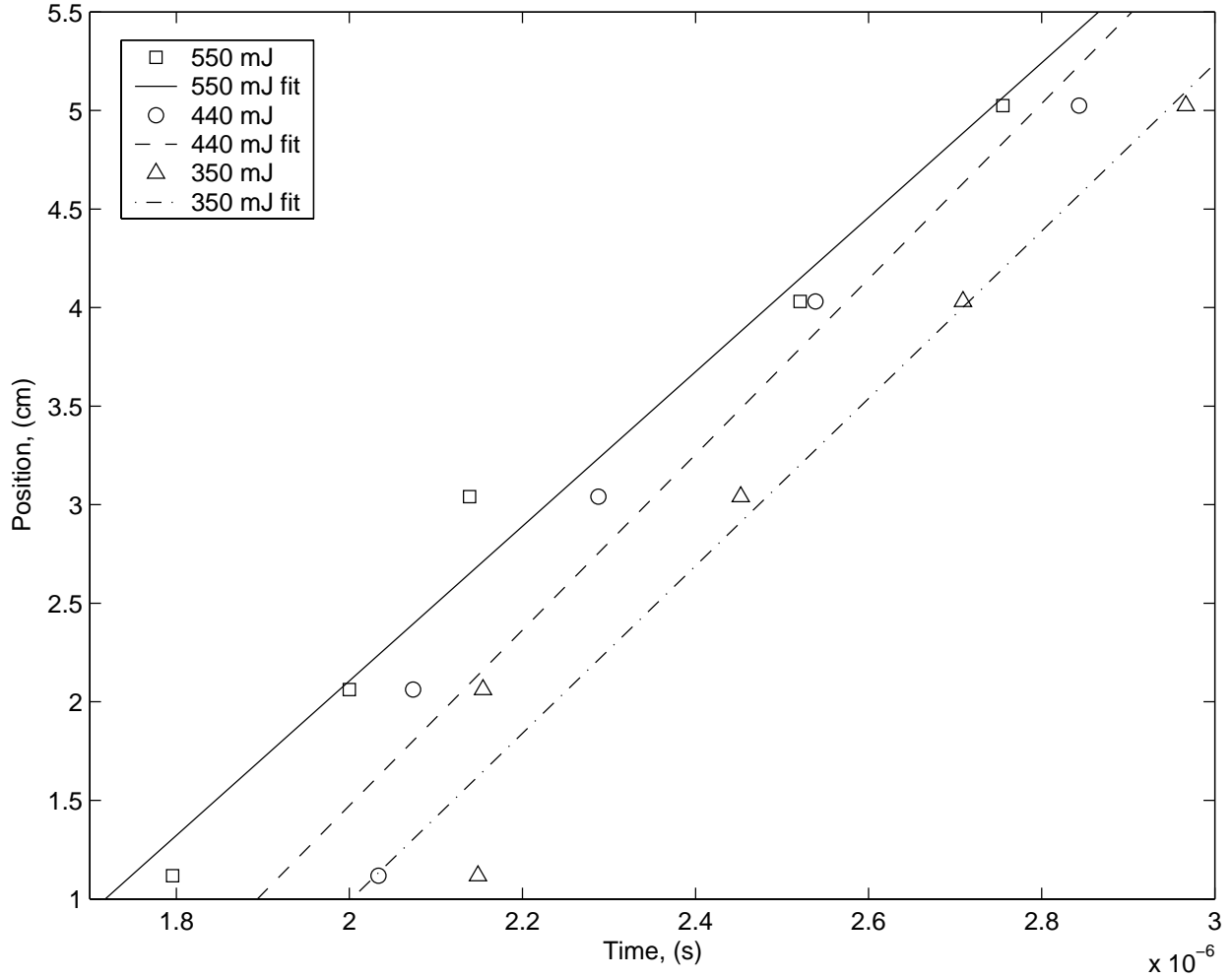


Figure 5.4: Langmuir probe position versus V_{12} signal arrival time for 350 mJ, 440 mJ, and 550 mJ.

To estimate flow speed from this data, the time at which the normalized V_{12} signal reaches 0.5 is determined for each position. Three shots were taken at each laser energy and Langmuir probe position. At each position, the arrival times of the three shots are averaged. These average arrival times are graphed versus position as shown in Fig. 5.4.

In Fig. 5.4, the 550 mJ data shows clear separation between arrival times at different Langmuir probe positions. However, the 440 mJ and 350 mJ data show no such clear separation. This effect is due to the offset of the Langmuir probe from the centerline of the plume. As laser energy decreases at constant spot size, the ion density and flow speed are known to decrease for unmagnetized laser produced plasmas on the identical experiment.[24] The component of the velocity vector perpendicular to \vec{B} and normal to the target surface therefore decreases as laser energy decreases. This means the kinetic $\beta = \mu_0 n_i m_i u_i^2 / B^2$ of the plasma in directions normal to the target decreases as the laser energy decreases. The magnetic field can therefore restrict flow to a larger magnitude in the cases of the 350 mJ and the 440 mJ laser energy. Analysis of the

Table 5.1: Flow speeds and kinetic β .

E_l (mJ)	u_0 (m/s)	u_B (m/s)	n_i ($\times 10^{18} m^{-3}$)	β
550	5.62×10^4	4.24×10^4	1	4.94×10^{-4}
440	4.90×10^4	4.09×10^4	0.75	1.96×10^{-4}
350	4.17×10^4	3.88×10^4	0.5	1.18×10^{-4}

\dot{B} probe signal at the 1 cm position, Fig. 5.5, verifies this. The peak field displacement in the 550 mJ case is approximately 3 times as great as in the case of the 440 mJ and 350 mJ cases. The slower plasma speeds mean that the field will be displaced less. Those regions of the plasma closer to the centerline, however, will be more efficient at field displacement and propagation across field lines. Therefore, the arrival times at 1 cm position for the 350 mJ and 440 mJ laser energies are not used. Rather, the flow speed is calculated with positions 2 cm through 5 cm.

From the results shown in Fig. 5.4, the flow speeds of the plasma are calculated. It is found that flow speeds at all laser energies are decreased. Table 5.1 shows the flow speeds with and without the magnetic field present, u_0 and u_B at the different laser energies used, as well as the kinetic β estimated from the local ion density at the 2 cm Langmuir probe position. If the plasma were perfectly conducting, the plasma would displace the magnetic field until the magnetic field energy density equalled the initial kinetic energy of the plasma as well as the thermal energy of the plasma. As the plasma has a finite resistivity, the magnetic field diffuses in to the plasma. A recent study showed that the ion speed begins to slow within a few millimeters of the target under a similar experimental arrangement with an Aluminum laser produced plasma.[49] This plume slowing represents a source of energy to drive plume heating or other effects.

5.2.2 Magnetic Field Calculations

The rare earth magnets create a large, steady state field in to which the plasma travels. As the plasma expands, it may exclude some of the flux from its path. The magnetic field then diffuses back in to the expanding plasma, as the plasma is not a perfect conductor. After calibration of the \dot{B} coil as discussed in the experimental chapter, Chapter 2, the probe was tested in the case of no external field present. In Fig. 5.5, only a very weak, $< 0.1 G$ field was detected as the plume passes the \dot{B} probe. At the 1 cm probe position with the external field present, the field displacement is smaller in magnitude than the field line displacement found elsewhere. This may seem counterintuitive. However, this is an effect of the offset of the probe as discussed in the previous section. Note that the 550 mJ signal is less affected by the offset, as seen in the flow speed data.

At all positions, the degree of field displacement increases with increasing laser energy on target. The \dot{B} signal arrives later as laser energy is decreased, which indicates that the plasma arrives at a later time, and thus flow speed decreases as laser energy decreases. The increase in flow speed with laser energy density also

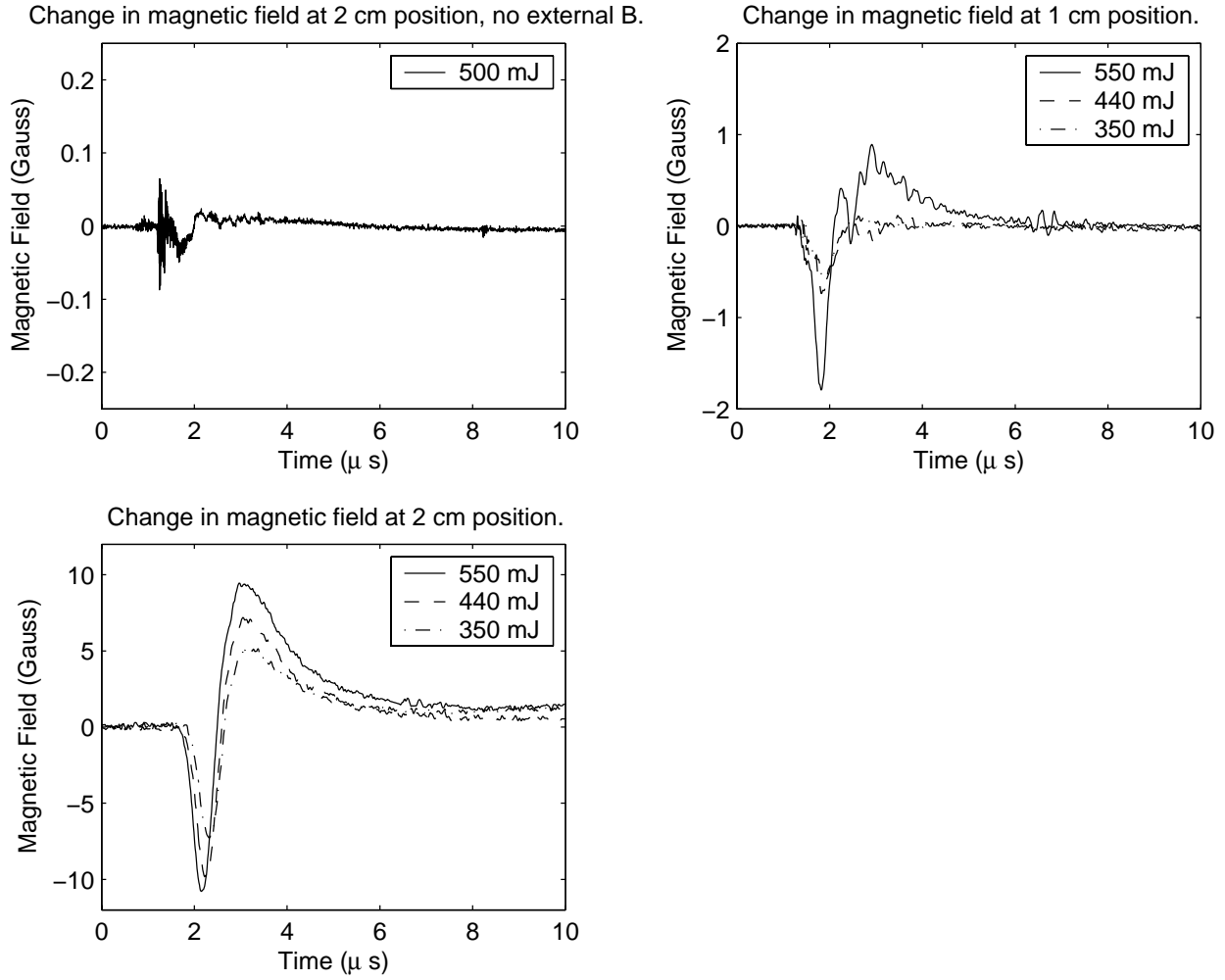


Figure 5.5: Change in magnetic field at a laser energy of 350 mJ, 440 mJ, and 550 mJ at different positions. The first plot contains the change in the field without the external magnetic field present.

acts to increase the kinetic β . Thus, field line displacement will increase as laser energy density increases. Furthermore, increases in density with laser energy, observed in the field free case and only weakly found with the external field present, will act to increase kinetic β . Increases in electron temperature will increase the pressure driven β , $2\mu_0 P/B^2$. All of these factors act to increase the amount of field line displacement as the plume passes the \dot{B} probe.

There is an interesting change in the magnitude and shape of the \dot{B} prone signal seen between 3 cm and 4 cm. The field displacement is greater in magnitude at 4 cm than it is at 3 cm. However, the magnetic field is significantly smaller at 4 cm than at 3 cm, so larger field line displacement is possible. The scientific basis for the change in the shape are unknown. Changes in the magnetic diffusion coefficient due to changes in density or temperature can act to change the temporal dependence of field line diffusion.

From Figs. 5.5 and 5.6, diffusion of the field in to the plasma occurs in a time scale of less than or equal

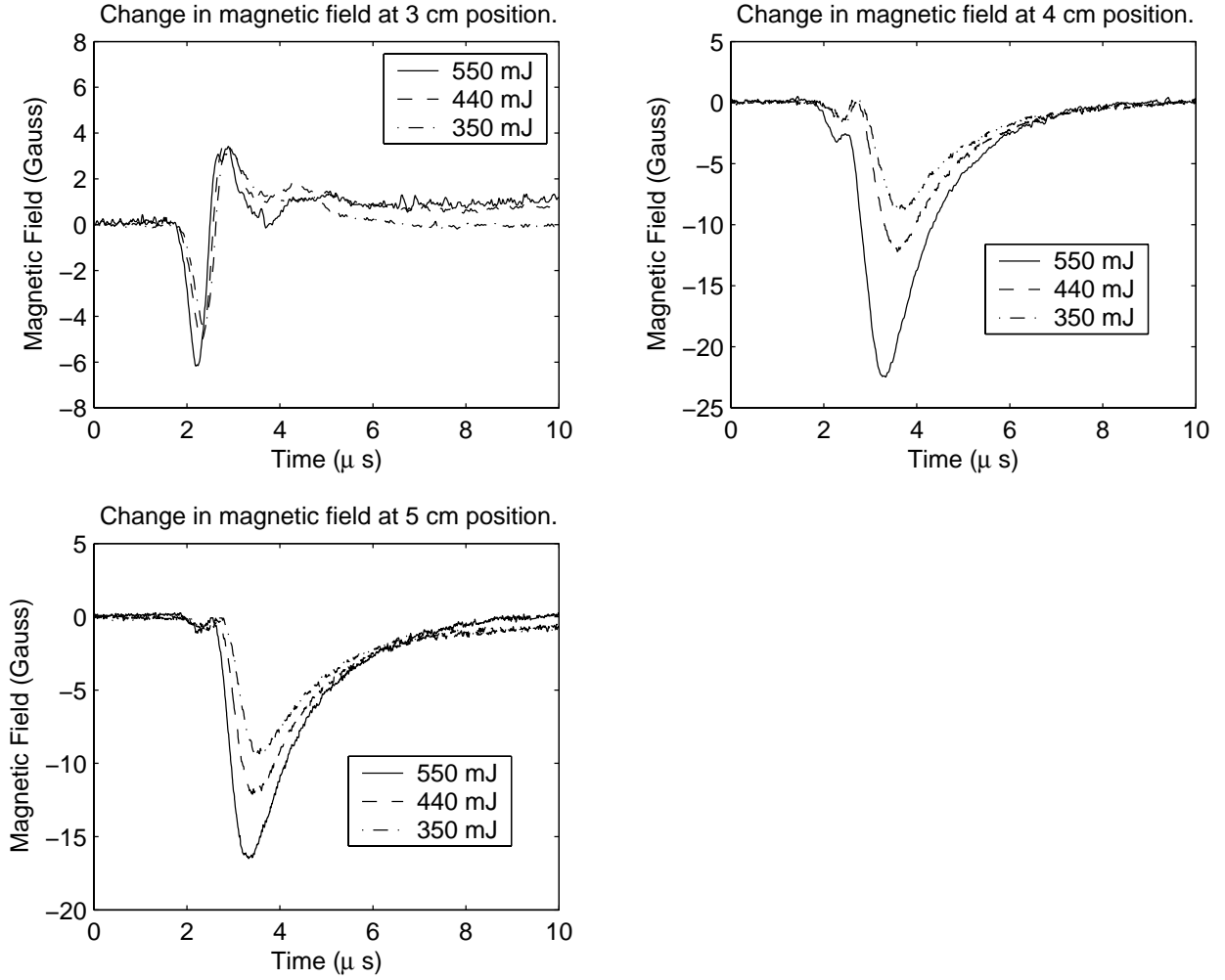


Figure 5.6: Change in magnetic field at a laser energy of 350 mJ, 440 mJ, and 550 mJ at different positions.

to $1\mu s$. The diffusion time may be estimated as:[47, 79]

$$\tau_B \approx \frac{\mu_0 L^2}{\eta_{\perp}} \quad (5.23)$$

where τ_B is the diffusion times, μ_0 is the permeability of free space, L^2 is the scale length of the plasma, and η_{\perp} is the plasma resistivity perpendicular to the magnetic field. The scale length of the plasma is of the order of a few centimeters. The Spitzer resistivity is used to calculate the resistance:[47]

$$\eta_{\perp} = \frac{2^{3/2} m_e^{1/2} Z e^2 \ln \Lambda}{12 \pi^{3/2} \epsilon_0^2 T_e^{3/2}} \approx 1.03 \times 10^{-4} \frac{Z \ln \Lambda}{T_e^{3/2}} \quad (5.24)$$

For a conservative estimate, the scale length of the plasma is taken to be 1 cm. From the previous work without a magnetic field present, the electron temperature at 1 cm is approximately 10 eV. With the magnetic field present, the electron temperature at 1 cm is approximately 40 eV. If $\ln \Lambda \approx 10$, the resistivity is, $3.26 \times 10^{-5} \Omega m$ and $6.27 \times 10^{-6} \Omega m$ for electron temperatures of 10 eV and 40 eV, respectively. These

resistivities result in magnetic field diffusion times of $3.85 \mu s$ and $20.04 \mu s$, for $T_e = 10 eV$ and $T_e = 40 eV$, respectively.

These field diffusion times are of the order or larger than the plume lifetime. This suggests that electron-ion collisions alone do not constitute the resistivity of the plasma. Interactions with neutral atoms may act to increase the resistivity of plasma. Furthermore, anomalous transport may also occur, increasing the effective electron-ion collision frequency.[46, 103]

Neutral atoms can contribute to the resistivity in Eq. 5.23. The resistivity due to neutral atoms is:

$$\eta_n = \frac{m_e \nu_{en}}{n_e e^2} \quad (5.25)$$

The electron-neutral collision frequency, ν_{en} , is given in Eq. 5.4. Therefore, the electron-neutral resistivity is:

$$\eta_n = \frac{m_e n_n v_{th,e} \sigma_{en}}{n_e e^2} \quad (5.26)$$

with the electron-neutral collision cross section defined in Eq. 5.5. As discussed in the first section of this chapter, a representative electron-neutral collision frequency is $\nu_{en} = 32.86 \times 10^6 Hz$. It will be shown later in the chapter, under the assumption of quasineutrality, that the electron density in the magnetized plasmas is $n_e \approx 10^{18} m^{-3}$. This yields a resistivity due to neutral carbon atoms of $\eta_n = 0.00117 \Omega m$. Accounting for the neutral atoms within the plume, the diffusion time for magnetic fields in the plasma is:

$$\tau_B \approx 1.07 \times 10^{-7} s \quad (5.27)$$

Therefore, if the neutral atoms within the plume are considered, the magnetic field line diffusion time becomes compatible with the observed time scale for field line diffusion. If anomalous diffusion is present, it is difficult to discern from the effects of neutrals alone based on field line diffusion measurements.

5.2.3 Electron Temperature

Figure 5.7 shows the electron temperatures as function of time at the laser energies used in this experiment. Figure 5.8 shows the peak electron temperatures for each laser energy as a function of position. It is interesting to note that the electron temperature is larger at the $2 cm$ Langmuir probe position than at the $1 cm$ Langmuir probe position for laser energies $440 mJ$ and $350 mJ$. This further supports the idea that the expansion is more restricted to the $1 cm$ Langmuir probe position at $440 mJ$ and $350 mJ$ than at $550 mJ$.

Electron temperatures are found to be uniformly larger in the presence of a magnetic field compared as compared to electron temperatures in an unmagnetized pulsed laser deposition plasma. In earlier work on the same experiment without the presence of a magnetic field, electron temperatures were found to be between 5 and $10 eV$, depending on the distance from the target.[24] In the magnetized case, electron temperatures were found to be between approximately 20 and $40 eV$. A similar increase in electron temperature in magnetized PLD plumes has been observed by several authors. Koopman found an increase in electron temperature

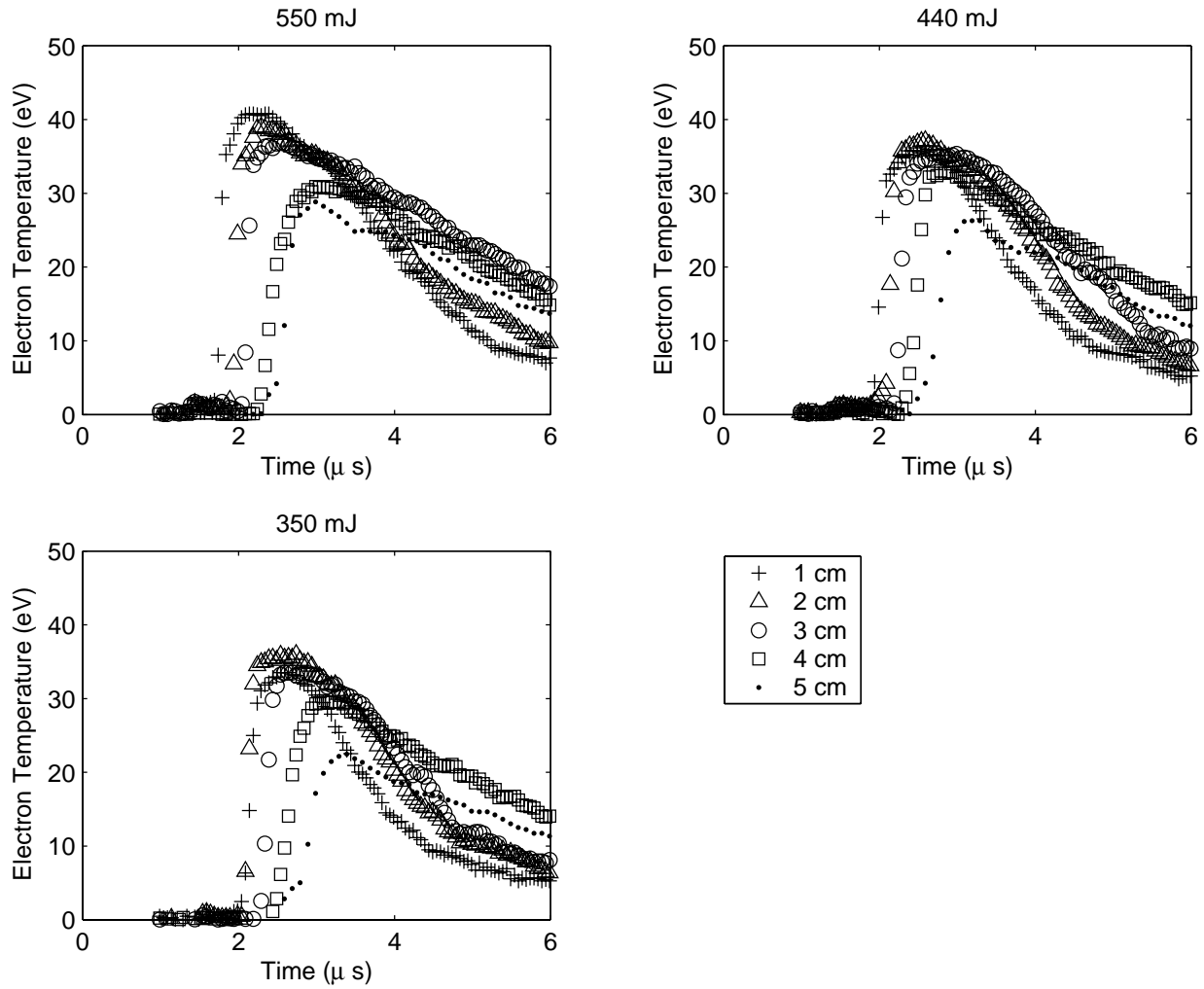


Figure 5.7: Electron temperatures corrected for the presence of a magnetic field as a function of time at 550, 440 and 350 mJ Lens position 12 cm.

in a copper PLD plasma from approximately 4 eV in the unmagnetized case to 50 eV in the magnetized case.[46] The results of Dirnberger, et al, suggest an increase in electron temperature from their optical emission spectroscopy results, however they did not attempt to calculate electron temperature.[41] Neogi and Thareja found the the electron temperature slightly increased in a magnetized carbon PLD plasma.[40] Their estimate was based on the relative spectral line intensity but they did not validate the assumption of local thermodynamic equilibrium which is necessary for the technique to determine accurate temperatures.

Joule heating via induced currents during field line diffusion in the plasma offers one possible heating mechanism which may be visualized as follows. The expanding plume displaces the magnetic field lines. Finite resistivity and anomalous diffusion then permit the field lines to diffuse into the plasma sufficiently rapidly for heating to occur on the time scale of the plasma. The diffusion of field lines in to the plasma creates currents which heat the plasma. Following the diffusion arguments of Chen,[79] an estimate of the

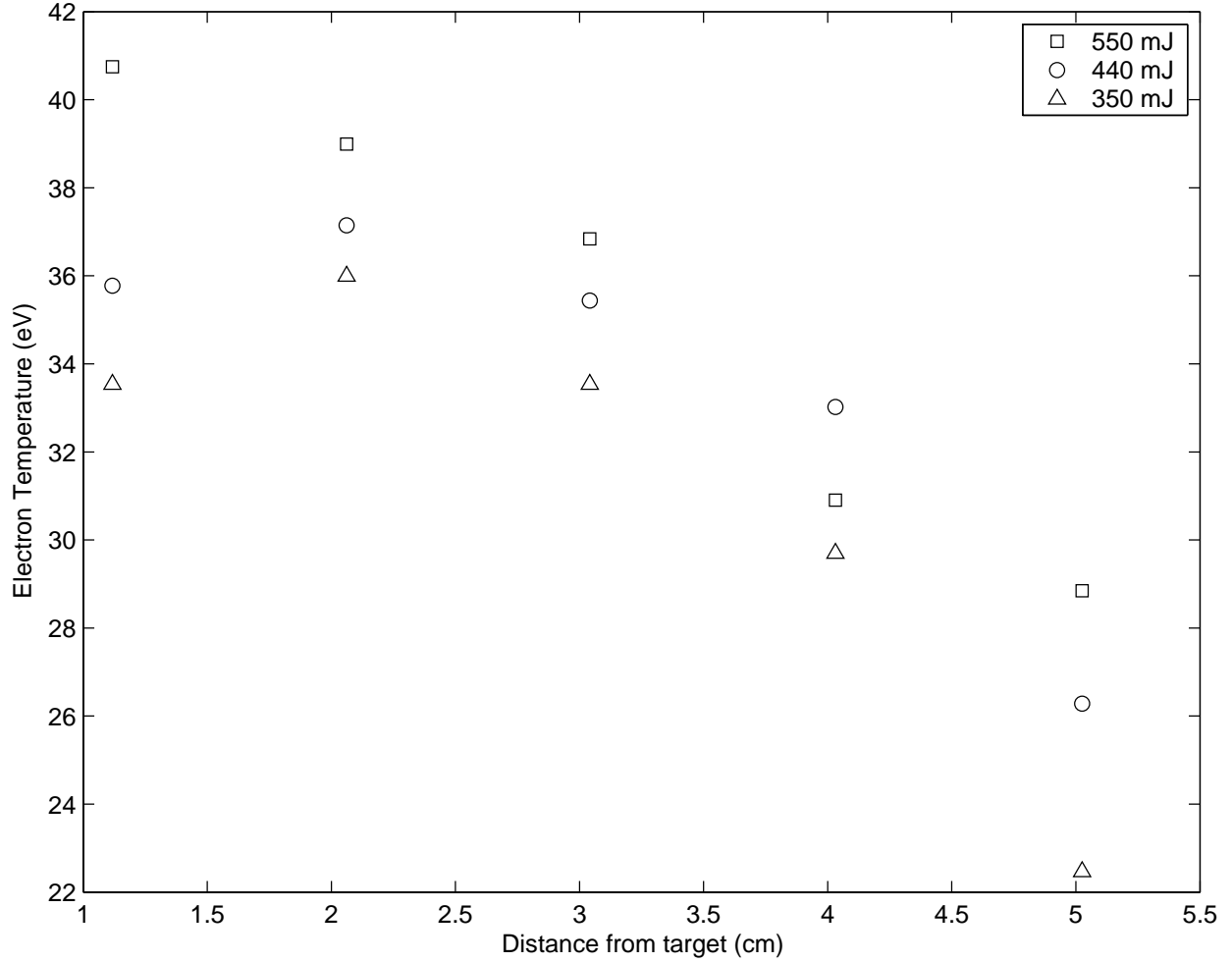


Figure 5.8: Peak electron temperatures corrected for the presence of a magnetic field as a function of position. Laser energy 350 mJ. Lens position 12 cm.

thermal energy gained by the plasma, E_{diff} , is:

$$E_{diff} \approx \frac{VB^2}{\mu_0} \quad (5.28)$$

where V is the volume of the plasma, and B is the magnitude of the displaced magnetic field. At the 2 cm probe position and a laser energy of 550 mJ, the magnitude of the displaced field is ≈ 10 Gauss. From the density results, described in detail in a later section, there are $\approx 10^{12}$ electrons in 1 cm^3 of plasma. Thus, the total thermal energy which could be gained is:

$$E_{diff} \approx \frac{10^{-6} \text{ m}^3 \cdot (10 \text{ Gauss} \cdot \frac{1 \text{ Gauss}}{10000 \text{ T}})}{4\pi \times 10^{-7} \text{ TmA}^{-1}} \approx 7.96 \times 10^{-10} \text{ J} \quad (5.29)$$

On a per-electron basis, this represents 0.005 eV/electron. This is not sufficient to explain the observed increases in electron temperature.

Compression of the electron fluid upon interaction with the magnetic field is another possible heating

mechanism. Once the laser pulsed has ceased, the plume expands outward into space. After travelling some distance, it begins to interact with the region of significant magnetic field. If the plasma were a perfect conductor, it would displace the field lines at the expense of kinetic energy. Even if the plasma is not a perfect conductor, it will still displace the field lines until they diffuse in the plasma. In typical PLD plasmas, finite resistivity and anomalous diffusion [46] permit field line diffusion. The maximum possible increase in electron temperature would occur if the flow of the plasma is completely stopped. From a global energy balance, the increase in electron temperature is:

$$\Delta T = m_e \frac{u_0^2}{2} \quad (5.30)$$

where u_0 is the plume flow speed before it interacts with the field. Assuming an initial flow speed of $5 \times 10^4 \text{ m/s}$, a typical flow speed in the unmagnetized case, $\Delta T \approx 0.007 \text{ eV}$. This cannot account for the large increases in electron temperature observed. Incomplete slowing of the plasma due to diffusion across the field would further reduce ΔT . The expansion of the plume is not restricted parallel to the magnetic field, thus adiabatic effects are still important. Electron heating due to compression of the electron fluid as it interacts with the magnetic field is not important.

As noted in the section on plume flow, the flow speed in the 550 *mJ* case is reduced from a field-free value of $5.6 \times 10^4 \text{ m/s}$ to $3.9 \times 10^4 \text{ m/s}$. Harilial, et al, performed a study using optical spectroscopy, and found a compression of around a factor of two.[49] They found this compression only during very short time scale, less than 50 *ns*. After 100 *ns* the density in the field-free case and the density with the magnetic field present are identical at 1 *mm* from the target. Without considering any possible compression, the change in the flow energy itself represents $\approx 100 \text{ eV/atom}$ of energy which could drive heating. The electron-ion temperature equilibration time must be considered. This time is:

$$\tau_{eq} = \frac{m_i}{2m_e\nu_{ei}} \quad (5.31)$$

In Eq. 5.31, m_i is the ion mass, m_e is the electron mass, and ν_{ei} is the electron-ion collision frequency as calculated in Eq. 5.1. If typical plume parameter values at the 2 *cm* Langmuir probe position are used ($T_e = 40 \text{ eV}$, $n_i = 10^{18} \text{ m}^{-3}$), then $\tau_{eq} \approx 0.06 \text{ s}$, which is significantly greater than the plume lifetime. However, these values are those after the plume has been heated. For instance, if typical field-free values are used ($T_e = 10 \text{ eV}$, $n_i = 10^{20} \text{ m}^{-3}$), then $\tau_{eq} \approx 1.9 \times 10^{-4} \text{ s}$. If plume heating were to occur earlier in the plume lifetime, where densities are higher, the equilibration time may become reasonable. If anomalously large diffusion rates are present, as has been observed in this type of plasma,[46] the equilibration time may be further reduced.[103]

Heating of a plasma interacting with a magnetic field may come from several sources. Magnetic field line diffusion is not sufficient to explain the observed increase in electron temperature, as is deceleration of the electron component of the plasma. Deceleration of the ions is the only sufficiently large source of energy to drive heating. This process is the reverse of the adiabatic expansion process. Anomalous transport must occur in these plasmas.

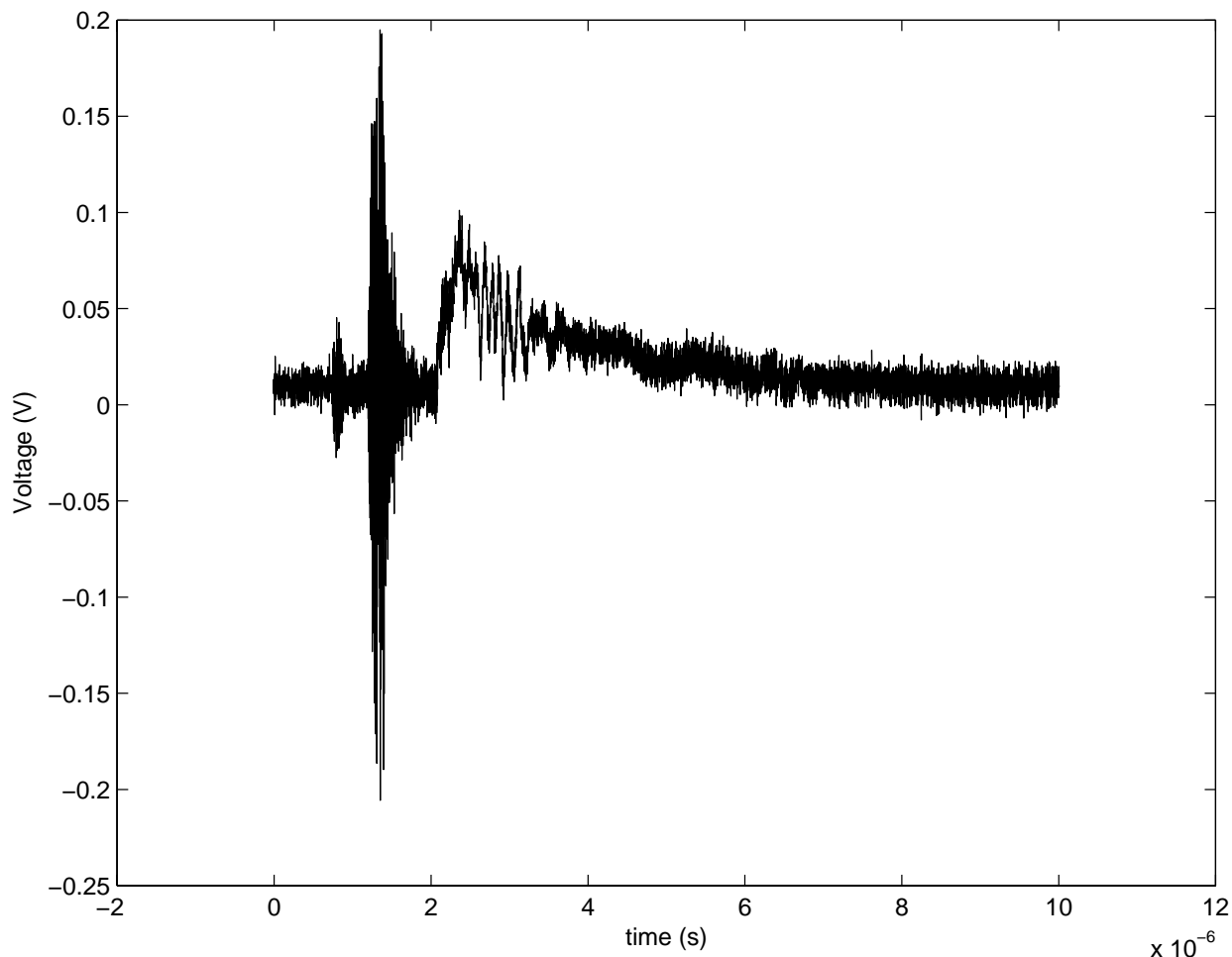


Figure 5.9: Raw V_{i3} signal from Langmuir probe in magnetized plume. Langmuir probe position 3 cm. Laser Energy 550 mJ. Spot size 0.22cm^2 .

5.2.4 Ion Dynamics

Ion dynamics in the plasma plume is investigated using Langmuir probe measurements. Figure 5.9 shows a sample raw V_{i3} Langmuir probe signal. From the V_{i3} data, density may be calculated, provided that plasma flow speed and electron temperature are known. The small signal near $0.8\ \mu\text{s}$ is likely an effect of the laser pulse due to ultraviolet photons from the scattered laser light emitting photoelectrons. The work function for Langmuir probe tips, tungsten wire, is rather low, 4.5eV . A larger signal is present in all density data at close to $1.2\ \mu\text{s}$. This feature is not seen in V_{i3} data taken from unmagnetized experiments, and its physical explanation is currently unknown. It may be a signal at the lower hybrid frequency, but this requires further analysis for confirmation. Near $2\ \mu\text{s}$ is the signal corresponds to the signals from V_{12} and V_{2g} . This signal is considered to be the plasma plume as it travels through the magnetic field.

An oscillation appears in many of the the ion density signals which is not seen in the ion density signals of unmagnetized laser produced plasmas. Figures 5.9, 5.10 and 5.11 show examples of this oscillation in the

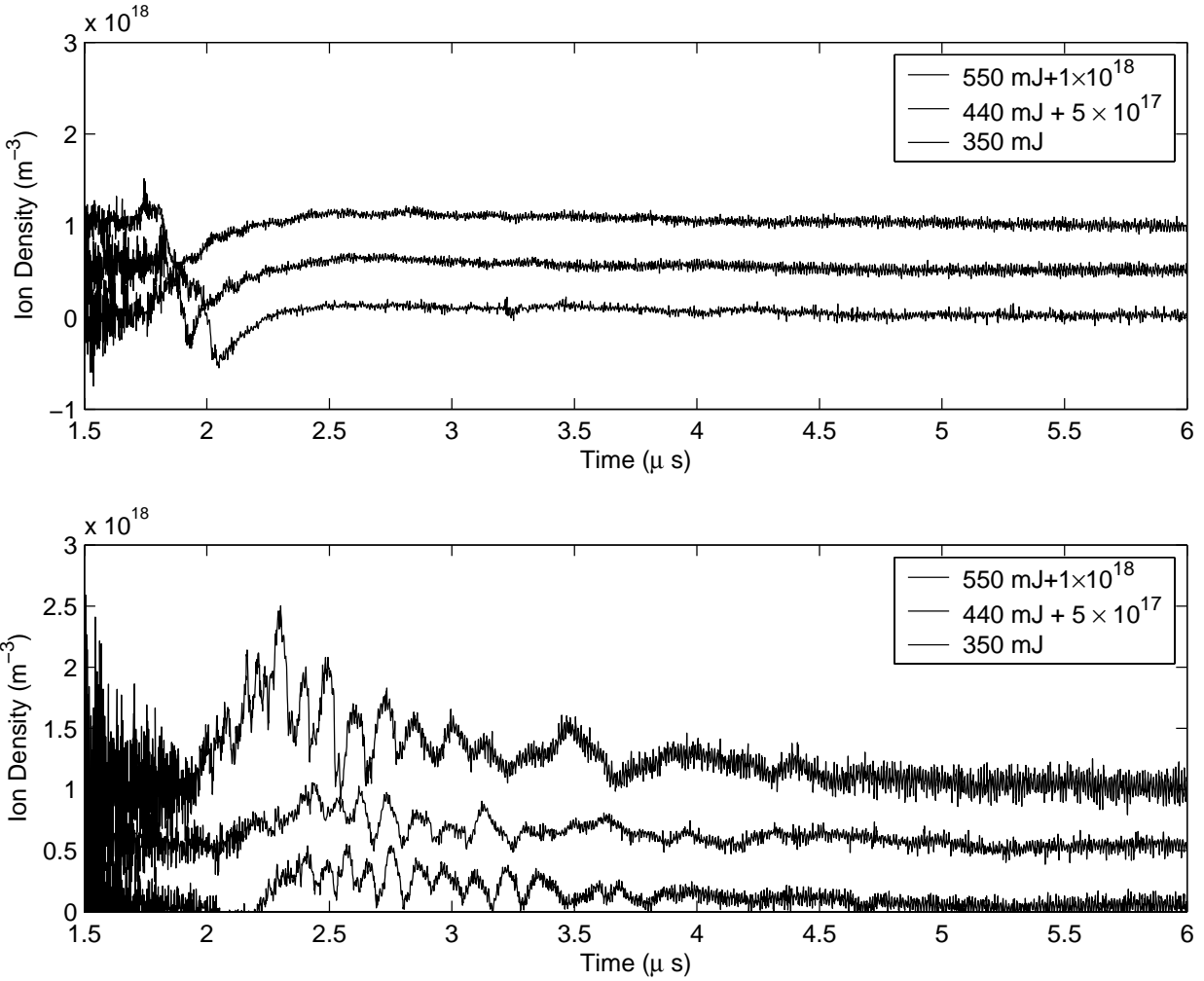


Figure 5.10: Ion densities at 1 cm and 2 cm at different laser energies. Spot size 0.22cm^2 .

density. The oscillatory behavior is highly repeatable and has a magnitude on the order of the peak density itself. This may indicate superposition of an instability or a wave generated in the plasma.

Addition of a magnetic field to a plasma permits a wide variety of waves and instabilities not seen in unmagnetized plasmas. The first step is to determine likely mechanisms for the oscillatory behavior in the Langmuir probe signal. Phenomena that would affect the ion signal include Alfvén waves, both parallel and perpendicular to \vec{B} , ion cyclotron waves, and oscillations at the lower hybrid frequency. Ion drift waves cannot be entirely discounted, as they can exist with a frequency near the ion cyclotron frequency. However, they are stable, unlike electron drift waves, and cannot grow to the large magnitudes observed.[47]

Consider first the possibility of Alfvén waves as a means of affecting the Langmuir probe signal. The Alfvén wave is an oscillation of the magnetic field which may occur parallel or perpendicular to the steady state magnetic field \vec{B} . In these waves, the plasma moves with the field lines. The Alfvén wave dispersion relation is, for waves $\parallel \vec{B}$:

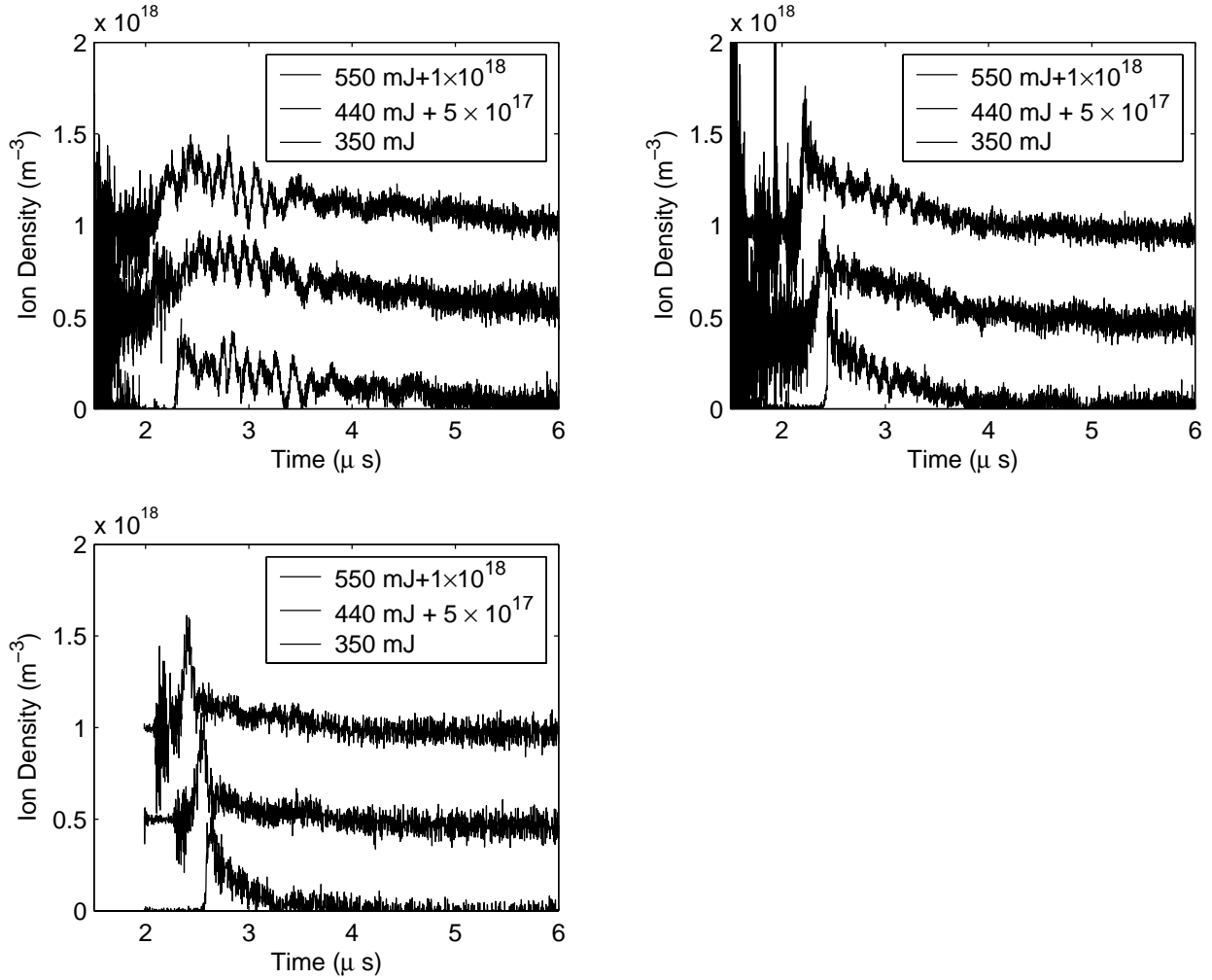


Figure 5.11: Ion densities at 3 cm, 4 cm, and 5 cm at different laser energies. Spot size 0.22cm^2 .

$$\frac{d\omega}{dk} = v_A = \frac{B}{\mu_0 M n} \quad (5.32)$$

with v_A the Alfvén velocity, B the magnetic field, μ_0 the permeability of free space, M is the mass of the ion, and n is the ion number density. Provided that $c^2 \gg v_A^2$, Eq. 5.32 is valid for Alfvén waves perpendicular to the magnetic field as well. For a magnetic field of 0.4 T and an ion density of $4 \times 10^{17}\text{ m}^{-3}$, the Alfvén speed is $\approx 4 \times 10^6\text{ m/s}$. Since the probe is 5 mm long, the smallest wavelength with \vec{k} parallel \vec{u} that it can detect is of this order. For $\vec{k} \perp \vec{u} \perp \vec{B}$, the smallest wavelength is of the order of the probe diameter, 0.025 cm . Corrections for the motion of the plasma are minimal since the flow speed is much less than the Alfvén speed. Let k then be $1/0.005\text{ m}^{-1}$, as the probe is 5 mm long. The Alfvén frequency is then $\omega = kv_A \approx 0.8 \times 10^9\text{ Hz}$, which is greater than the observed frequency for these oscillations. If $\omega = \Omega_C$, the wavelength is $.44\text{ m}$, which is much larger than the size of the device. A second order of magnitude argument can be made based on the time for an Alfvén wave to cross the length of the device, in this case taken to be 2.54 cm . The Alfvén time is $t_A = \frac{2.54\text{ cm}}{4 \times 10^6\text{ m/s}} \approx 6.4 \times 10^{-9}\text{ s}$. This time is much smaller than

the observed wave period of 1.11×10^{-7} s. It is therefore unlikely that the observed signal is due to Alfvén waves. Furthermore, since an Alfvén wave is an oscillation in the magnetic field, it should be observed in the \vec{B} probe data.

Oscillations at the lower hybrid frequency occur when the wave vector \vec{k} is exactly perpendicular to the magnetic field. The oscillations occur with a frequency $\omega_{lh} = (\omega_C \Omega_C)^{1/2}$, where ω_C is the electron cyclotron frequency and Ω_C is the ion cyclotron frequency. For a magnetic field of 0.4 T, the lower hybrid frequency is $\omega_{lh} \approx 475.09 \times 10^6$ Hz. This is substantially larger in magnitude than the recorded frequency. Thus, oscillations at the lower hybrid frequency are not the cause of the oscillations in the Langmuir probe signal.

The frequency of the oscillation is approximately 9×10^6 Hz. It is only observable at the 2 cm and 3 cm Langmuir probe positions, although it is weakly present at the 4 cm position. At these positions, the magnetic field is approximately 0.4 T. Thus, the ion cyclotron frequency, Ω_C , is $\Omega_C = 3.213 \times 10^6$ Hz for $Z = 1$. Ion cyclotron waves propagate approximately perpendicular to the magnetic field. The ion cyclotron dispersion relation is:

$$\omega^2 = \Omega_i^2 + k^2 C_s^2 \quad (5.33)$$

where ω is the frequency of the wave, Ω_i is the ion cyclotron frequency, k is the wave vector, and C_s is the sound speed. For this analysis, the sound speed is taken to be kT_e/m_i . The peak magnetic field in the region where the plasma propagates is ≈ 0.4 T. This gives an ion cyclotron frequency of $\Omega_i \approx 3.21 \times 10^6$ Hz. From the results in Fig. 5.8, a typical electron temperature is ≈ 35 eV. The observed waveform has a frequency of $\approx 8.5 \times 10^6$ Hz. The dispersion relation, Eq. 5.33, thus yields a wave vector $k \approx 473.92$ m⁻¹. The corresponding wavelength for this ion cyclotron wave is $\lambda \approx 2.11$ mm. For a wave with this wavelength to be accurately detected by the Langmuir probe, it must be propagating perpendicular to the flow speed \vec{u} , as well as propagating perpendicular to \vec{B} . This is because the probe length parallel to the flow is 5 mm. The dimension of the probe perpendicular to the flow and the magnetic field is the probe diameter, 0.25 mm.

Essentially, the ion cyclotron wave is an ion acoustic wave which is affected by the cyclotron motion of the ions. Given that the signal frequency is approximately the ion cyclotron frequency, much less than the frequency of other plausible phenomena, and only appears in the ion saturation signal, and disappears at probe positions with a weaker magnetic field, it is concluded that this feature is the result of an ion cyclotron wave. The magnitude of the wave is of the order of the signal itself. This suggests that the wave has grown by some means. Typically, this is the result of an instability.

Previous researchers have observed instabilities in laser produced plasmas. However, none have observed an instability at the ion cyclotron frequency. Thareja, et al., suggest that a Rayleigh-Taylor (RT) instability will occur in PLD plasmas as they interact with a magnetic field. In the current work, the instability is observed in a region where the field line geometry is approximately favorable for the RT instability to occur, at positions 3 cm to 5 cm from the target. At 2 cm the oscillation is also observed, although the probe tip encompasses regions that are favorable and unfavorable to the growth of the RT instability. At 1 cm, small oscillations are present, but they are difficult to discern.

The growth rate of the Rayleigh-Taylor instability for magnetized plasmas is estimated by allowing curvature and gradient-B forces to take the place of gravity in the RT instability for magnetized plasmas. An effective acceleration, which takes the place of gravity, g , is therefore:[47]

$$g = \frac{2P}{\rho R_C} \quad (5.34)$$

where P is the pressure, ρ is the mass density and R_C is the radius of curvature. The e-folding time of the RT instability is, with Eq. 5.34:

$$\tau_{RT} = \left(g \frac{|\nabla P|}{\rho} \right)^{-1/2} \approx \left(\frac{2|dP/dz|}{\rho R_C} \right)^{-1/2} \quad (5.35)$$

The radius of curvature is taken, for a conservative estimate, to be half the length of the magnet separation, 1.75 cm. This is an overestimate of the field line curvature. In this case, the density as a function of position can not easily be supposed as in the unmagnetized case. There is no a priori reason to expect a $1/r^2$ dependance. Figure 5.11 shows that the density is approximately constant between 3 cm and 5 cm. The most significant density changes occur between 2 cm and 3 cm, at 550 mJ. In this case, estimating the derivative with a forward difference, $dP \approx n_3 k T_3 - n_2 k T_2$ and $dz \approx 1$ cm, ignoring the probe offset corrections for the purposes of this estimation, and with values from Fig. 5.11, Eq. 5.35 becomes:

$$\tau_{RT} \approx \left(\frac{2 \times 1.6 \times 10^{-19} \left| \frac{5 \times 10^{17} \times 38 \text{ eV} - 2 \times 10^{18} \times 40 \text{ eV}}{0.01 \text{ m}} \right|}{2 \times 10^{18} \text{ m}^{-3} \cdot 12 \times 1.66 \times 10^{-27} \text{ kg} \times 0.0175 \text{ m}} \right)^{-1/2} \quad (5.36)$$

The growth time for the RT instability is estimated to be $\tau_{RT} \approx 6 \times 10^{-7}$ s. As the laser firing time is ≈ 0.5 μ s for this experiment, the instability would have ≈ 2 μ s to grow before reaching the probe, as shown by the arrival time of the instability at the different Langmuir probe positions in Figs. 5.10 and 5.11. This time represents $\approx 2/0.6 \approx 3.33$ e-folding times for the instability. Thus, the instability is estimated to increase in magnitude by a factor of $\approx e^{3.33} \approx 28$. However, the instability cannot grow unless the field geometry is favorable. Thus, the instability would not have 2 μ s to grow. Instead, it has at maximum the time it takes for the plasma to cross the 2 cm probe position, as the instability appears fully developed by then. Therefore, it has $\approx 0.5 \text{ cm} / 4 \times 10^6 \text{ cm/s} \approx 1.25 \times 10^{-7}$ s to form. As this is less than the Rayleigh-Taylor growth time, the RT instability is eliminated as a possible source of the instability. Also, note that Eq. 5.36 underestimates the growth time, since the radius of curvature used is too small. The radius of curvature used would require that the field lines be perfect half circles with a radius equal to half of the magnet separation distance. The magnetic field displacement results show that the plasma does not induce large bending of the field lines as it passes through the field region.

As a physical argument against the detection of the RT instability with the current experimental setup, it must be noted that the Rayleigh-Taylor instability forms at the boundary between the vacuum and the plasma. However, the ion saturation signal suggests the instability is present within the plasma bulk. The RT instability in the case would occur at the leading edge of the plasma plume.

A second possibility is an ion cyclotron instability. These instabilities have been studied in papers by Bernstein,[104], Hall, et al.,[105], Harris,[106] and Dory, et al.[107] The relevant conclusion of their papers is that ion cyclotron waves are unstable for certain ion velocity distribution functions. For velocities perpendicular to the magnetic field, Maxwellian ion distribution functions are stable against small perturbations, whereas delta function ion distributions are not. A special class of distribution functions which approaches Maxwellian in certain limits is also unstable. Dory gives an example of the delta distribution function as:[107]

$$f(v_{\perp}, v_{\parallel}) = \left(\frac{1}{2\pi v_{\perp}} \right) \delta(v_{\perp} - \alpha_{\perp}) \delta(v_{\parallel}) \quad (5.37)$$

In Eq. 5.37, $f(v_{\perp}, v_{\parallel})$ is the ion distribution function, v_{\perp} is a velocity perpendicular to the field, v_{\parallel} is a velocity parallel to the magnetic field, α_{\perp} is the speed of ion motion, and δ is the delta function. In the delta function distribution, there is no spread in ion velocities around the speed of ion motion, α_{\perp} . Dory, et al, show functions with a sufficiently small spread of ion velocities around α_{\perp} are also unstable.

For delta function distributions the instability condition is that waves that satisfy

$$n < \frac{\omega}{\Omega_C} < n + 1 \quad (5.38)$$

where n is an integer, ω is the wave frequency, and Ω_C is the ion cyclotron frequency, will be unstable on ranges

$$mJ_n < \frac{k_{\perp} \alpha_{perp}}{\Omega_C} < mJ_{n+1} \quad (5.39)$$

where mJ_n is the m th zero of the n th order Bessel function.

For the earlier estimate of $\omega \approx 8.5 \times 10^6$ Hz, and $\Omega_C = 3.21 \times 10^6$ Hz, $\omega/\Omega_C \approx 2.65$. Thus, $n = 2$ in Eqs. 5.38 and 5.39. Assuming that the distribution of ion velocities is not Maxwellian, but represented by a delta function with α_{\perp} equal to the flow speed, then α_{\perp} is given by u_B in Table 5.1. For $n = 2$, and $m = 1$, and taking the flow speed for the 550 mJ case, the condition in Eq. 5.39 becomes

$$2.57 \text{ mm} < \lambda < 2.07 \text{ mm} \quad (5.40)$$

The wavelength derived earlier for the ion cyclotron wave was 2.11 mm. Thus, this ion cyclotron wave satisfies the criterion for instability for laser pulses of 550 mJ. It can also be shown that the instability condition is also satisfied for the 440 mJ and 350 mJ flow speeds. Growth rates formulae do not appear to be cited in the literature for this specific instability. The growth rates for ion-cyclotron instabilities in general functions of the ion cyclotron frequency, with maximum growth rates equal to the ion cyclotron frequency.[108] Thus, the fastest growth time for this instability is $\Omega_i^{-1} = 3.11 \times 10^{-7}$ s. This a sufficiently short growth time to explain the presence of an ion cyclotron instability. Further study is necessary to completely describe the behavior of instabilities within the laser ablation plasmas.

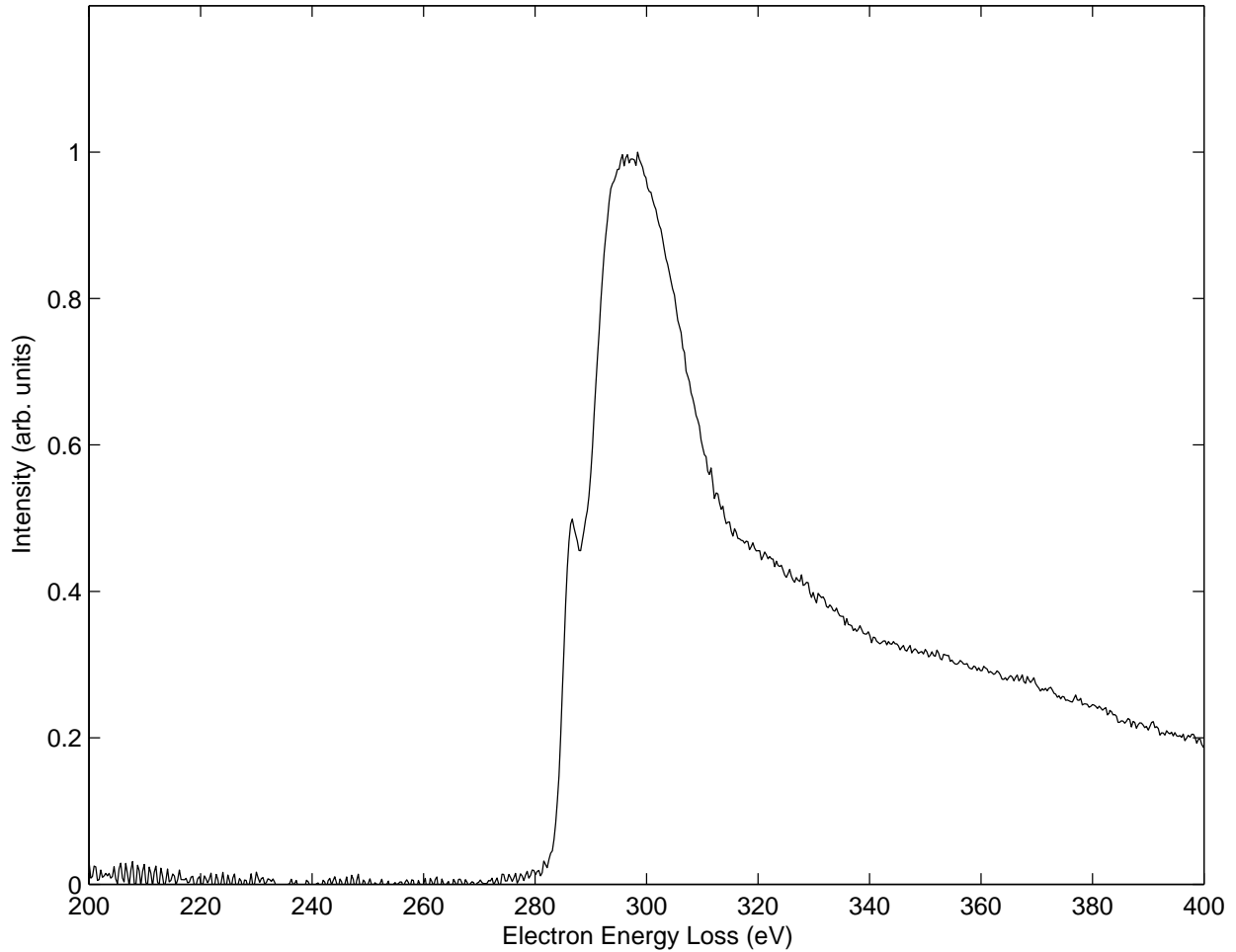


Figure 5.12: EELS spectrum of DLC film deposited with magnetic field.

5.3 Effect on Film Quality

The goal of magnetic deflection is to deflect the plume so that macroscopic particles travel along their usual paths whereas the ionic component of the plume is deflected. However, it is not apparent that the plume is deflected. Instead, the plume is decelerated by its interaction with the magnetic field, but still propagates across the field. From the flow speed results, it was found that the ions propagate with a speed of approximately 4×10^4 m/s. With typical magnetic fields in the range of 0.3 T to 0.4 T, the ion cyclotron radius would be between 1.66 cm and 1.245 cm. If the ionic component were deflected along this path, then there would be no noticeable ion population farther than 1 cm from the target. However, a significant ion density was found at all Langmuir probe positions.

In this case, the laser ablation plume behaves like a plasma, rather than an ion beam. The main effects of the magnetic field on the ion dynamics are the creation of instabilities and slowing of the ionic component. The dominant effect of the magnetic field on the dynamics of the plume electrons is to increase

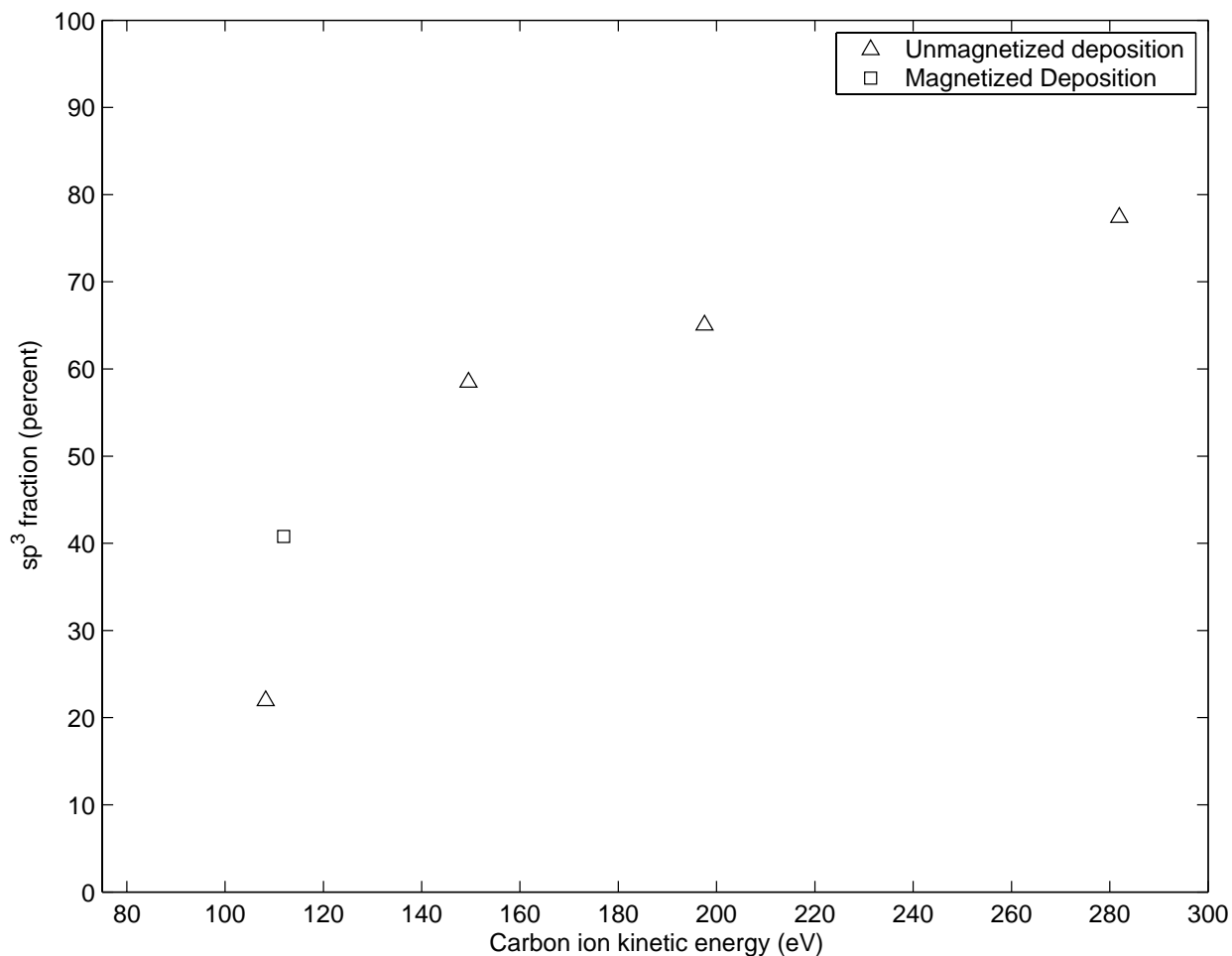


Figure 5.13: Effect of magnetic field on the sp^3 fraction of DLC films.

their temperature. To determine what effect this has on the growth of DLC films, a diamond-like carbon film was deposited with the magnetic field present as described in the Experimental chapter.

Figure 5.12 shows the electron energy loss spectrum from the DLC film deposited in the presence of the magnetic field. It shows the typical π^* and σ^* antibonding features typical of the K ionization edge in DLC films. The sp^3 fraction is quantified as described in the Experimental chapter. The sp^3 fractions for the previous, unmagnetized DLC depositions and the sp^3 fraction of the film deposited under unmagnetized conditions is shown in Fig. 5.13 as a function of ion kinetic energy. Although the laser energy was 550 mJ , the flow speed was significantly reduced due to the magnetic field as discussed earlier. The corresponding kinetic energy in this case, as derived from flow analysis, is 111.9 eV . The sp^3 fraction for this case is 40 percent. In the unmagnetized case, a carbon ion with energy of 108.27 eV yielded an sp^3 fraction of approximately 20 percent. The difference in these two energies is within the error of the measurement, approximately ten percent. However, the sp^3 fractions are quite different. Therefore, the flow speed and excitation energy of the neutrals are more important than that of the ions during the film formation process.

Chapter 6

Doped Diamond-like Carbon

The previous chapters have discussed the formation of diamond-like carbon films from the plasma plume created during pulsed laser deposition. From this, it is known how to control the sp^3 fraction and sp^2 microstructure of DLC films. This enables the control of hardness, electrical properties, and optical properties of DLC films. However, one of the problems in using diamond-like carbon in practical applications is the large internal compressive stresses within deposited films.[4, 1] One means by which the internal stresses may be reduced or eliminated is with the addition of certain dopants.[7, 6]

Two sets of doped diamond-like carbon films were created as described in the experimental section. Copper, which does not form a carbide, and Titanium, a carbide former were selected as dopants. Silver was also used as a dopant for Z-contrast imaging. Raman spectroscopy, hardness measurements, electron energy-loss spectroscopy(EELS), and high resolution transmission electron microscopy (HRTEM) were used to characterize these films.

6.1 HRTEM and Z Contrast

High resolution TEM was performed at the Scherzer defocus to investigate the structure of the diamond-like carbon and any dopants present within the film.[109] Diamond-like carbon appears as a diffuse, random pattern typical of HRTEM images from amorphous materials. Titanium and copper form nanocrystals within the diamond-like carbon, examples of which are shown in Fig. 6.2. The nanocrystals are all randomly oriented, as is expected for deposition on an amorphous material.

The production of copper nanocrystals in DLC created via ion beam synthesis has been reported by Gerhards, et al.[110] Copper does not form carbides, and has no solubility in carbon. Therefore, it should form nanocrystals of copper. Copper nanocrystals are found in the current work, as shown in Fig. 6.1. The copper nanocrystal size is ≈ 10 nm. Analysis of the copper doped DLC HRTEM images yields an interplane spacing of 3.624\AA . This is approximately the interplane spacing of $\{100\}$ planes of copper, 3.6148\AA . Thus, copper forms nanocrystals within the diamond-like carbon matrix.

Titanium, however, is a carbide former. This will act to reduce the mobility of titanium atoms on

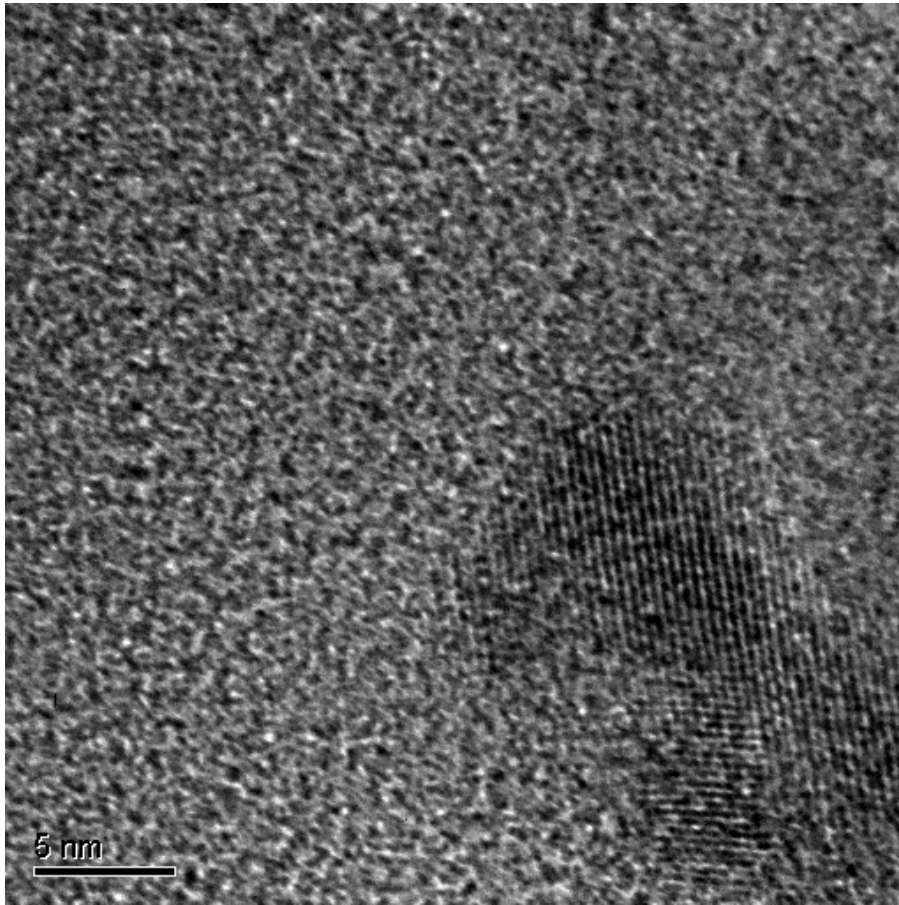


Figure 6.1: High resolution image of copper nanoparticles in diamond-like carbon.

the DLC surface. It might be expected to form titanium carbide crystals, or become incorporated in the amorphous matrix. If the dopant concentration is sufficiently high, layers of titanium or titanium carbide may be formed. The HRTEM images show that titanium will form titanium or titanium carbide crystals in DLC. Figure 6.2 shows titanium nanocrystals in diamond-like carbon. Analysis of the titanium doped image yields an interplane spacing of 2.263\AA . This is near the interplane spacing between $\{10\bar{1}1\}$ planes in titanium with a hexagonal structure, 2.2436\AA . Titanium carbide has a spacing between the $\{200\}$ planes of 2.165\AA . It is most likely that titanium crystals are formed, with bonding between the carbon and titanium occurring at the crystal-DLC boundary. The dimensions of the crystal are $\approx 10\text{ nm}$. A large number of Ti nanocrystals are present. The concentration of these nanocrystals can likely be changed by altering the thickness and number of Ti strips used in the deposition process.

In the case of silver doping, which is chemically similar to copper, the Z-contrast image in Fig. 6.3 shows the formation of ordered nanostructures. Self assembled nanostructures have been shown to occur in both crystalline and amorphous systems.[111] The creation of these materials has been described using a strain enhanced migration process in which adatoms migrate to regions of locally high stress.[111] In the case of

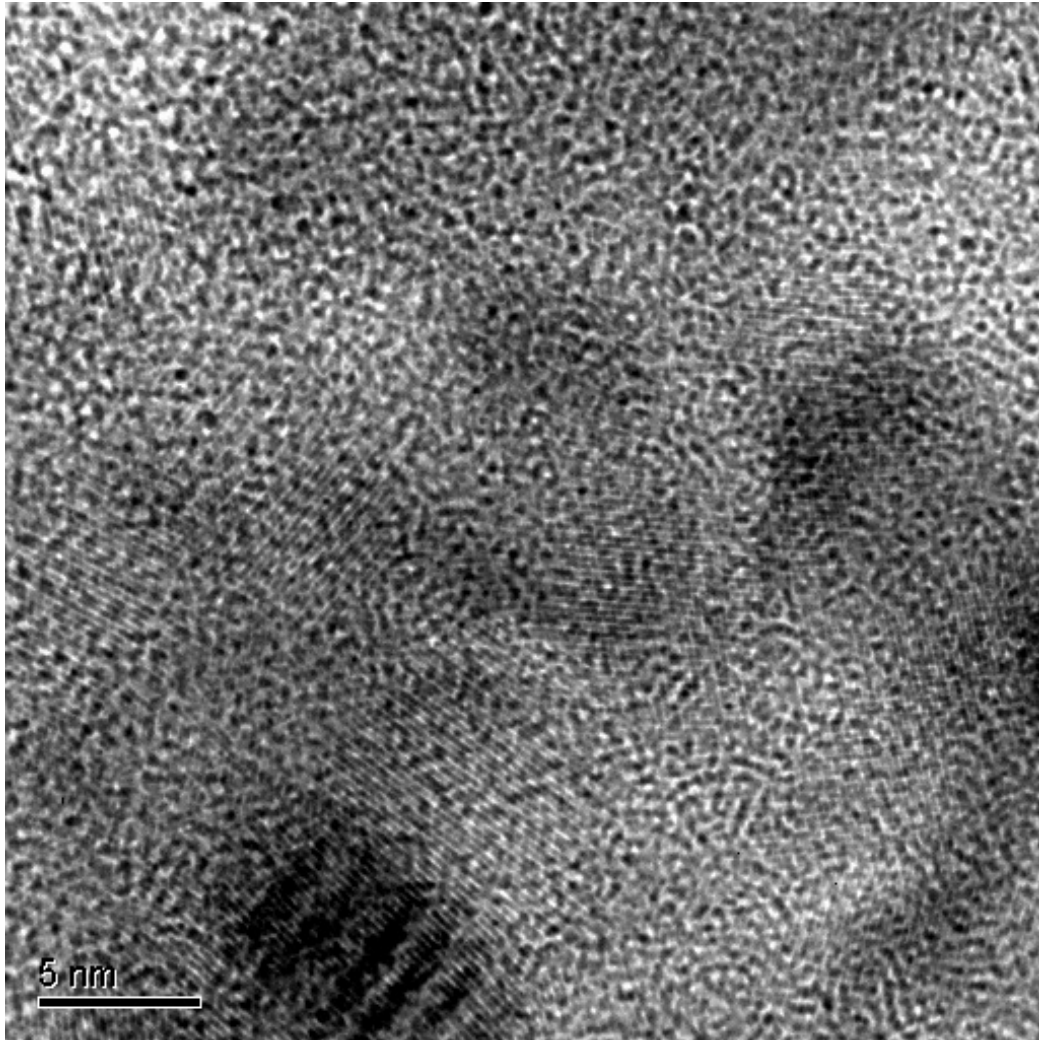


Figure 6.2: High resolution image of titanium nanoparticles in diamond-like carbon.

DLC, the individual dopant nanocrystals reduce the strain locally when a new layer of DLC is deposited. The next set of dopant adatoms will diffuse to regions of locally high stress. These regions will be anticorrelated with the previously deposited nanocrystals. This behavior is shown in the Z-contrast image of the silver doped diamond-like carbon.

6.2 Raman Spectroscopy

Raman spectra are acquired for the doped diamond-like carbon samples as discussed in the experimental section. The G peak is fit to a Breit-Wigner-Fano function, Eq. 2.7. Figure 6.4 shows the Raman data and BWF fits for copper doped and titanium doped DLC, respectively. Peak intensities are much higher than in the dopant free cases, as these films are considerably thicker. The BWF fit is an excellent fit for the Raman data. As in undoped films, there is no evidence of a D peak. This indicates that the sp^2 microstructure

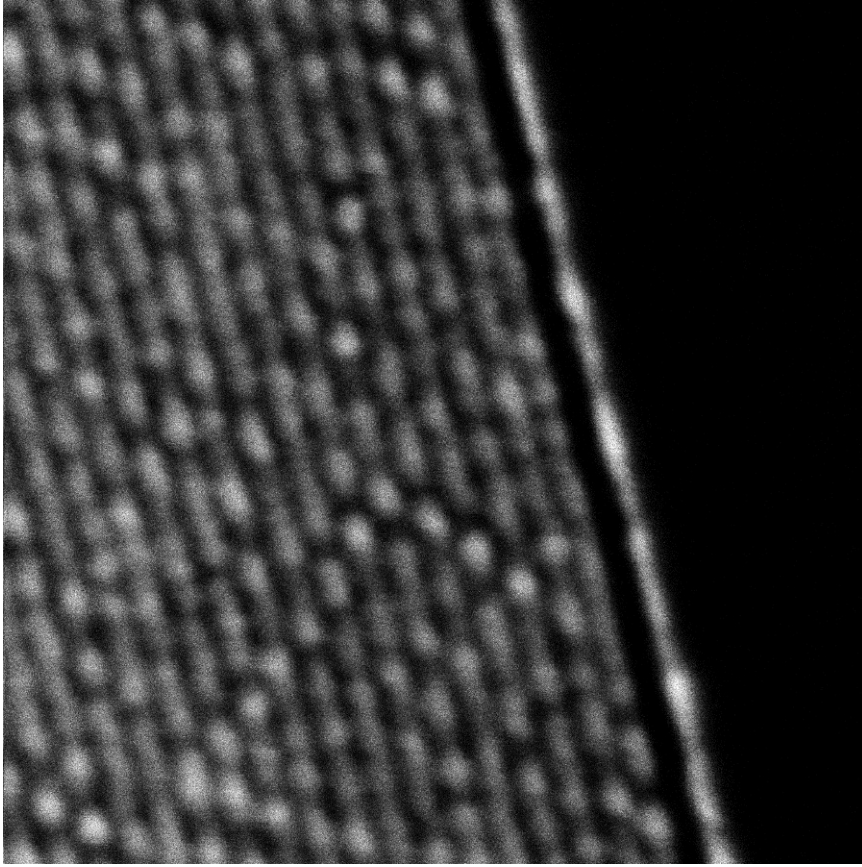


Figure 6.3: High resolution image of silver nanoparticles in diamond-like carbon.

within the film is ordered in to chains, and not in to hexagonal rings. At the largest titanium fraction, there was no discernable Raman signal. The film was highly reflective in nature, indicating the presence of metallic bonding. This suggests the formation of a significant quantity of titanium carbide, which is metallic. Thus, the fit on the highest concentration titanium doped DLC film is not accurate.

There is currently debate over the origin of the position of the Raman G peak. It is natural to assume that stress plays a role. Materials are stressed when there are non-equilibrium bond lengths. These occur at the interface in lattice matching epitaxy, where the substrate and film do not have equal lattice parameters.[112] Ferrari and Robertson theorize that changes in G peak position are a result of changes in the ordering of the sp^2 microstructure.[2] They support their claim by noting that stress reduction via annealing does not change the G peak position.[16] Stress reduction by annealing was also seen by Friedmann, et al., and showed similar Raman results.[113] In Ferrari and Robertson's model, annealing reduces stress by changing a few sp^3 sites to sp^2 sites.[2] This acts to relieve stress, as the size of an sp^2 coordinated carbon atoms takes less volume than that of and sp^3 coordinated site, along the plane of σ bonding. However, it may be that the tendency of the G peak to rise due to the addition of sp^2 dimers, is offset by the tendency of the G peak to fall with decreasing stress. The sp^2 dimers are known to have a G peak of $\approx 1630 \text{ cm}^{-1}$ and will thus shift

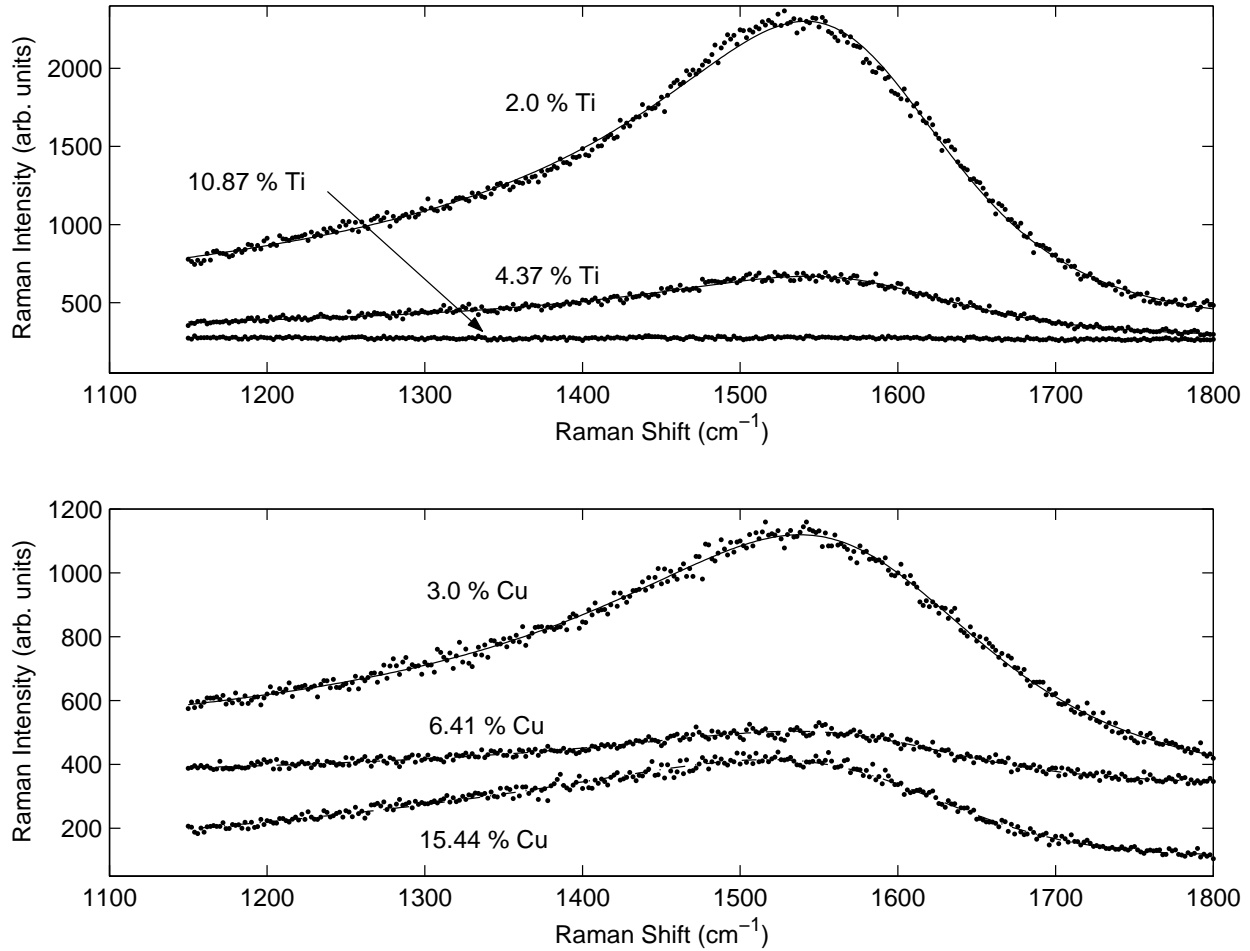


Figure 6.4: Visible Raman spectra of titanium and copper doped diamond-like carbon at different dopant concentrations.

the G peak to larger wavenumbers.[61] This is different than the case of low sp^3 fraction films, in which large sp^2 chains have delocalized π bonds, leading to reduced force constants, and thus a lower G peak position. The creation of sp^2 dimers is essential, as visible Raman spectroscopy is most sensitive to π sites. A lone sp^3 site will have an unbound p_z electron and cannot form a π bond.

If the stress within the films can be altered without changing the film microstructure, then the Raman G peak is an indicator of film stress. Alteration of the microstructure, that is, $sp^3 \rightarrow sp^2$ transitions and chains \rightarrow rings transitions will invoke separate phenomena which will also act on the G peak position. This case should apply for the in situ deposition used for the creation of titanium and copper containing DLC films used here. It is unlikely that the incident dopant ions possess sufficient energy to cause graphitization. The presence of titanium may act to enhance sp^3 fraction, as titanium is a carbide former. This may have to be considered an external means of changing film microstructure, as Ti may bond with carbon. For titanium it may be inappropriate to estimate film stresses via the G peak position of in-situ doped DLC films. Copper

Table 6.1: Fit parameters determined from Raman spectra for different copper and titanium concentrations.

<i>Ti</i>				<i>Cu</i>			
<i>F</i> (pct.)	ω_{max} (cm^{-1})	<i>Q</i>	Γ (cm^{-1})	<i>F</i> (pct.)	ω_{max} (cm^{-1})	<i>Q</i>	Γ (cm^{-1})
2.0	1555.1	-3.3318	243.9756	3.0	1549.2	-3.5563	302.2709
4.37	1555.3	-3.3944	247.2320	6.41	1539.4	-2.6448	276.8551
10.7	1582.2	-7.6972	146.8343	15.44	1503.9	-1.7717	311.2746

does not form a carbide in equilibrium conditions and is not soluble in carbon.

Stress reduction is calculated as described by Wei, et al.[7, 6] Given the G peak position in a reference EELS spectrum, the amount of stress reduction is calculated by:

$$\sigma = 2G \frac{1 + \nu}{1 - \nu} \frac{\Delta\omega}{\omega_0} \quad (6.1)$$

In Eq. 6.1, G is the shear modulus, ν is Poisson's ratio, ω_0 is the G peak wavenumber of a reference state, and $\Delta\omega$ is the difference between the ω_0 and the G peak wavenumber of the sample film. Wei, et al, give the value of $2G \frac{1+\nu}{1-\nu}$ as 300 *GPa*. From the earlier Raman spectroscopy study on undoped diamond-like carbon, the G peak position is located at 1550.76 cm^{-1} . [7, 6] Given the results of the Raman spectroscopy on the titanium doped DLC, Table 6.1, the stress appears to have increased from the undoped state. Unless the sp^3 fraction is significantly increased due to the presence of titanium, this is not possible. This is in contrast to the results of Wei, et al, who indicate that the presence of titanium decreases the local stress.[6] Qualitative proof that the addition of titanium reduces stress in DLC is taken from the fact that the titanium doped films were grown to much larger thicknesses than the undoped films without delamination. It must be noted that they used a different means of fitting the G peak, multiple gaussian fits, rather than the Breit-Wigner-Fano fit used in this research. The copper-doped samples show a decrease in stress of 0.302 *GPa*, 2.198 *GPa*, and 9.065 *GPa*, for concentrations of 3.0, 6.41, and 15.44 percent, respectively. Stress reduction in titanium(or other carbide forming element) doped DLC will occur as the relatively weak(compared to bonding in diamond) bond strengths of the titanium carbide will be deformed by the compressive stresses present in the DLC film. This can occur both in the bulk film and at the location of nanoparticles or other nanostructures within the film. The local compressive stresses can also be relaxed by interaction with nanoparticles. In copper and other non-carbide forming elements, stress reduction must occur via local stress reduction near the nanoparticle-DLC interface. The Z-contrast image of anti-correlated silver nanoparticles in DLC shown in Fig. 6.3 is evidence of this. It is concluded that even though stress reduction occurs in titanium and copper doped DLC films, visible Raman spectroscopy is inaccurate if the species are chemically active and may act to change the microstructure of the film.

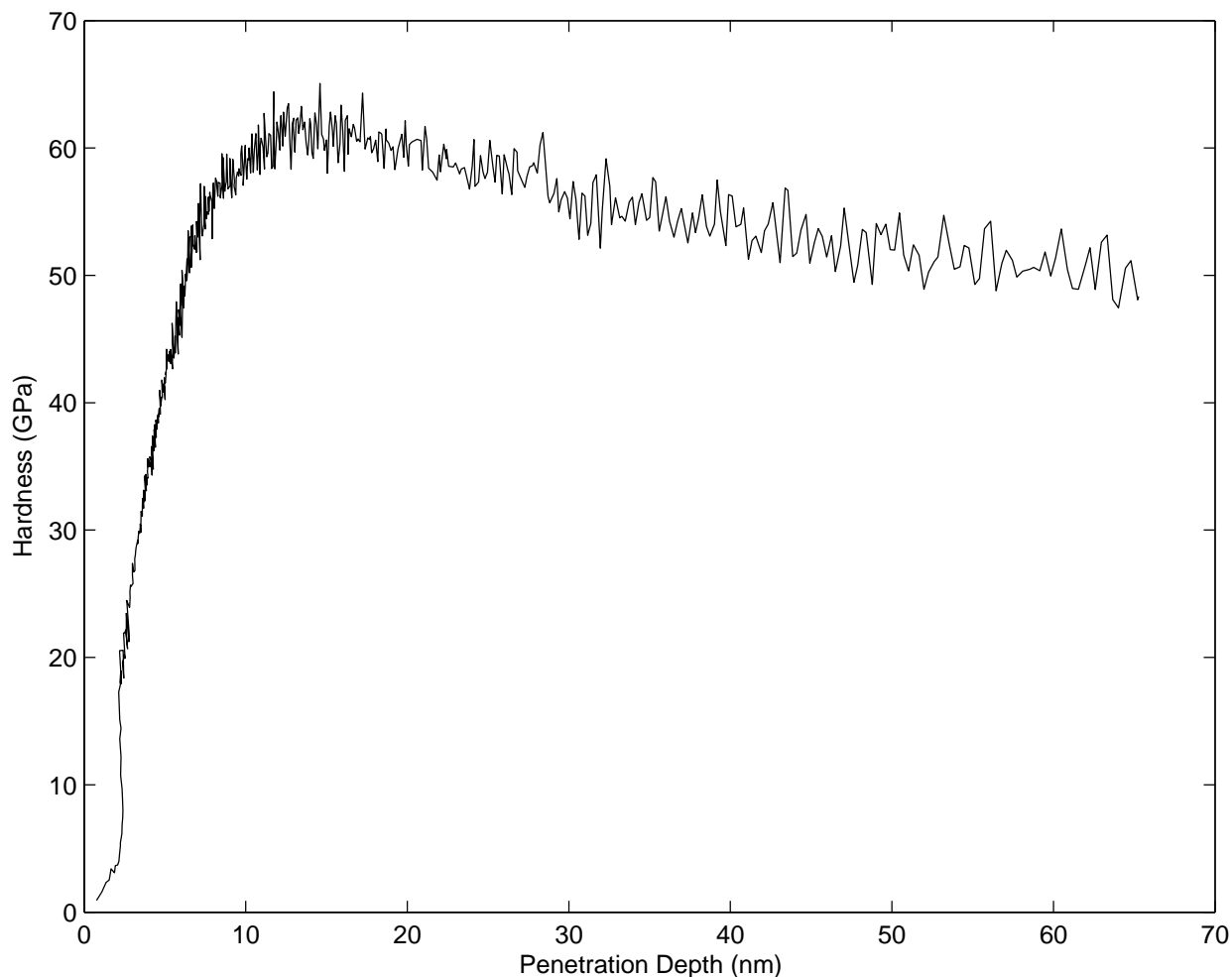


Figure 6.5: Sample hardness measurement of 2.0 atom percent titanium doped diamond-like carbon.

6.3 Hardness Measurements

Hardness measurements are performed as described in the experimental section on the titanium and copper doped specimens. A sample hardness versus depth plot is shown in Fig. 6.5. In this case, the hardness is around 51.35 *GPa* for the titanium doped at the smallest concentration. The results for all of the doped DLC films are shown in Table 6.2. The hardness of highly sp^3 coordinated diamond-like carbon is cited at 120 *GPa*. [1] By increasing the titanium and copper concentrations, the hardness of the films is reduced. In both cases, the hardness is reduced to ≈ 20 *GPa*. At the two largest titanium concentrations, the hardness measurements are within error bars. In undoped DLC, the large hardness value is a result of the highly directional and strong bonds between the sp^3 coordinated carbon atoms.

In the case of titanium, two mechanisms act to reduce the hardness as concentration increases. Titanium-carbon bonds are weaker than the σ and π bonds between carbon atoms, and thus less resistant to plastic deformation. Thus, as the fraction of titanium carbide increases, the hardness of the doped DLC will

Table 6.2: Hardness of copper and titanium doped diamond-like carbon as a function of concentration.

Dopant concentration is calculated from experimental conditions

<i>Ti</i>			<i>Cu</i>		
<i>F (atom%)</i>	<i>Hardness (GPa)</i>	σ (GPa)	<i>F (atom%)</i>	<i>Hardness (GPa)</i>	σ (GPa)
2.0	51.35	6.15	3.0	25.81	1.72
4.37	18.44	4.17	6.41	25.56	3.93
10.87	20.46	2.39	15.44	19.62	1.34

decreases. The presence of titanium carbide bonds also permits stress reduction, as discussed in the Raman spectroscopy section. The presence of nanoparticles also permits stress reduction. This will occur in both copper and titanium doped DLC. As copper does not readily form a carbide, there will be no opportunity for hardness reduction due to a weak carbon-copper bond. However, the presence of nanoparticles which can be deformed will result in a decrease in hardness. As the concentration of nanoparticles increases, the hardness will also decrease. In both titanium and copper doped specimens, the concentration of nanoparticles increases as dopant concentration increases. Thus, hardness of DLC films decreases as the concentration of dopants increases. Three dimensional nanoparticles may be very effective in stress reduction as the compressive stress can be relaxed in all directions.

6.4 Electron Energy Loss Spectroscopy

Electron energy loss spectroscopy is used to provide further information on the doped diamond-like carbon films. The electron energy loss spectra are acquired as discussed in the Experimental chapter. Electron energy loss spectra provide information on sp^3 bonding and dopant concentration. Low loss spectra provide information on electronic structure and bonding. The carbon K-edge spectra determine sp^3 fraction, and also yield information on bonding. Ionization edges of titanium and copper are used to determine dopant concentration.

6.4.1 Low Loss Region

Low loss spectra are shown in Fig. 6.6. Both titanium and copper doped diamond-like carbon films show a large plasmon peak near 25 eV due to carbon. Copper has a plasmon peak at 67.88 eV and titanium has a plasmon peak at 8 eV. The carbon plasmon peak does not shift significantly with titanium or copper concentration. As the titanium and copper plasmon peaks are not near the carbon plasmon energy, they will not act to interfere with the apparent location of the carbon plasmon peak by convolution of peaks. However, changes in valence electron density may alter the location of the plasmon peak. Therefore, increases in the dopant concentration do not greatly affect the density of carbon atoms within the film. Also, the valence

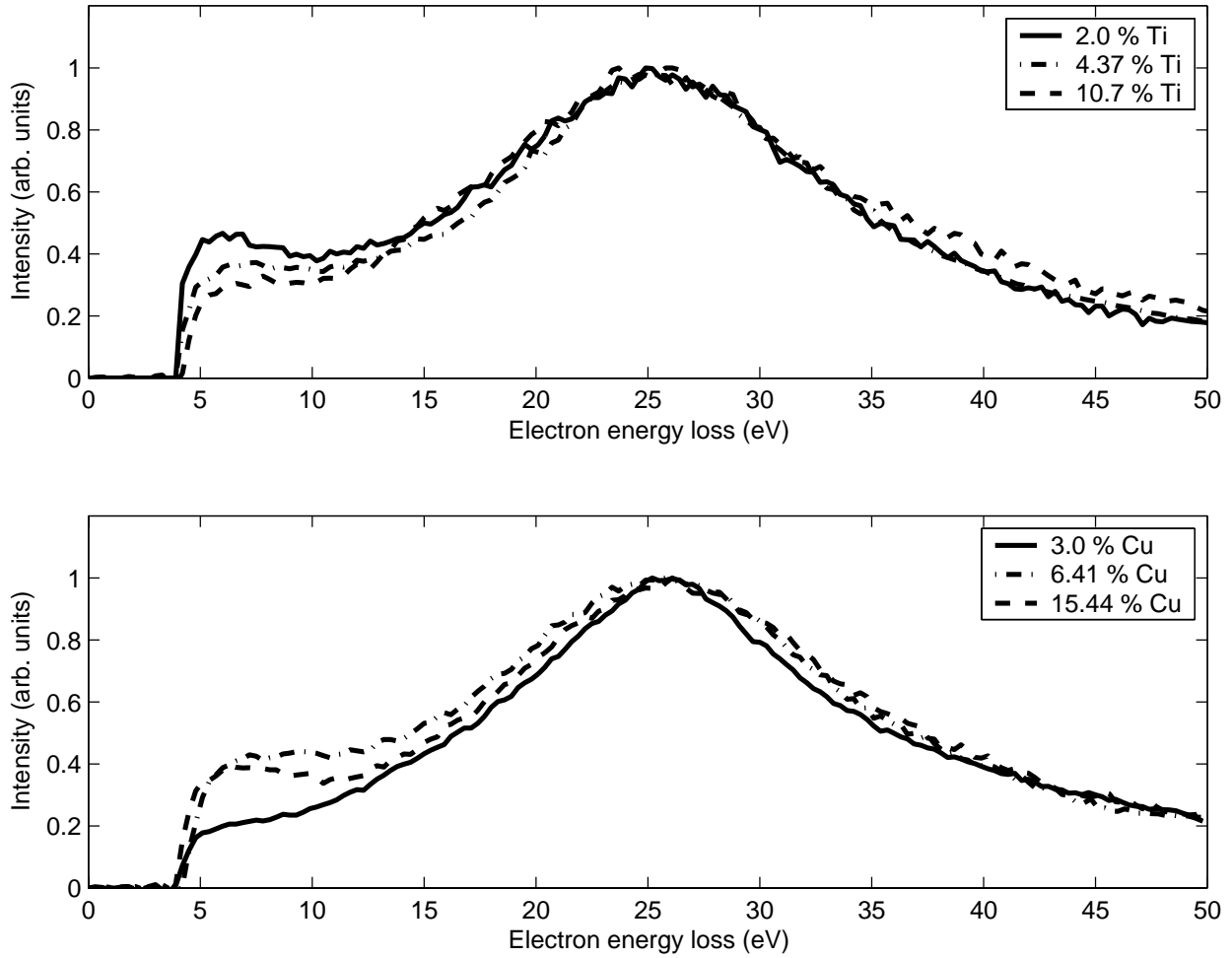


Figure 6.6: Low loss region from EELS spectra of titanium and copper doped diamond-like carbon at different dopant concentrations.

electron density is not noticeably changed. Noticeable modifications to the bulk film density likely occur at higher dopant concentrations.

Titanium readily bonds with carbon to form titanium carbide. This bonding in this compound is metallic. As the titanium fraction increases, the size of the $\pi \rightarrow \pi^*$ feature at approximately 5 eV decreases. Metallic bonding of titanium carbide will act to reduce the amount of bonding-antibonding transitions from π states, as the π electrons will transition directly to the conduction band. This will act to broaden the $\pi \rightarrow \pi^*$ transitions. The decrease in the relative intensity of the $\pi \rightarrow \pi^*$ feature can also occur due to an increase in the sp^3 fraction. The addition of titanium should not act to increase or decrease the sp^3 fraction, however. It will only affect the electronic structure.

As copper does not form a carbide, there should be no effect on the electronic transitions. However, the π bonding-antibonding peak increases between the lowest dopant concentration and the two largest dopant concentrations. This suggests an increase in the number of π states. The number of π states can increase by

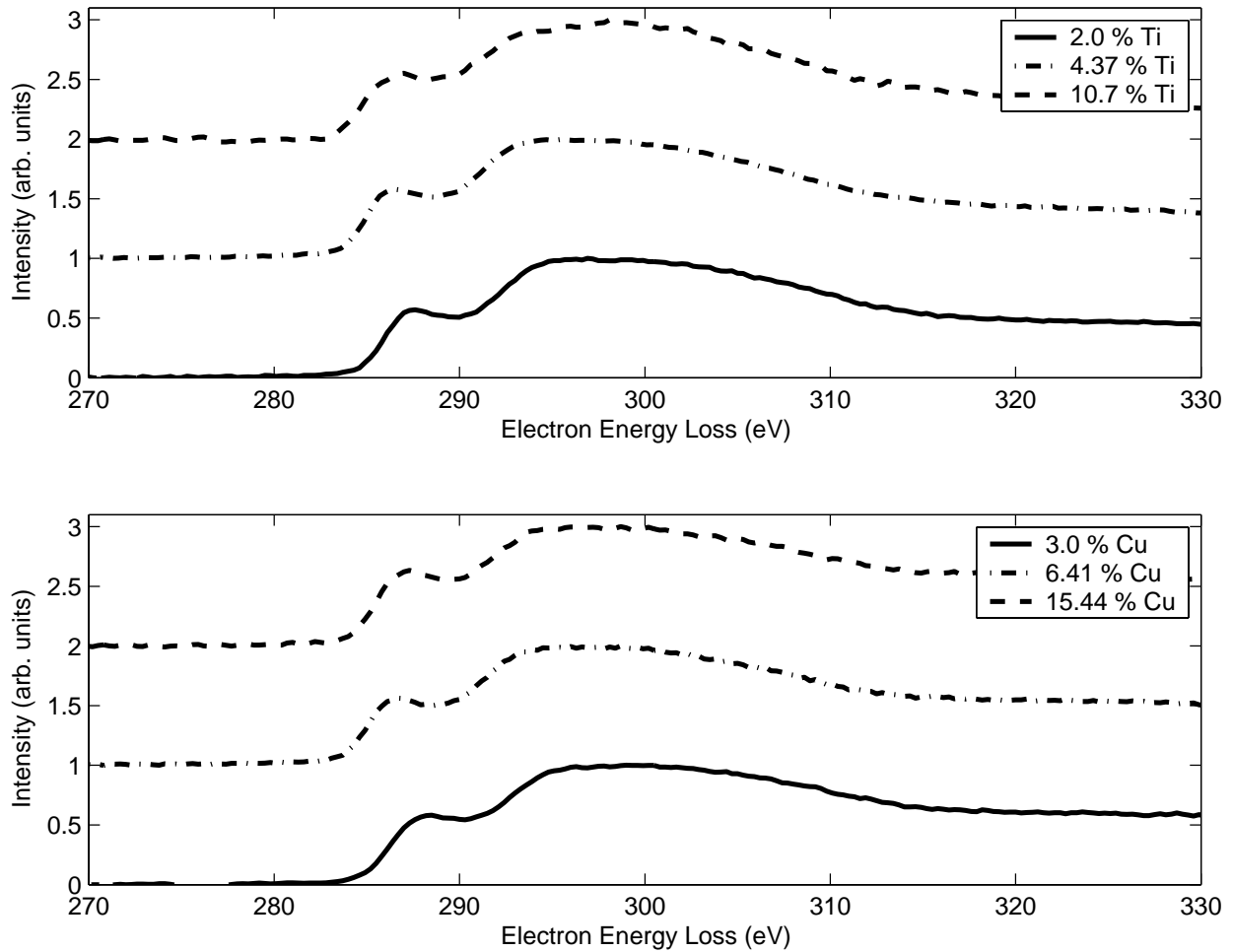


Figure 6.7: Carbon K shell ionization region from EELS spectra of titanium doped diamond-like carbon at different titanium concentrations.

two mechanisms. If the copper ions and neutral atoms have sufficient kinetic energy, they may induce damage as they interact with the DLC. If, in the non-equilibrium conditions of laser deposition, a copper-carbon compound is formed, the number of π states may increase, depending on the coordination of copper.

6.4.2 Carbon K Edge

The carbon K edge is used for quantification of the sp^3 fraction. Figure 6.7 shows the carbon K shell ionization edges from the EELS spectrum. The fraction of sp^3 bonded carbon is calculated as described in the experimental section. The results of this calculation are shown in Table 6.3. In the case of titanium doped diamond-like carbon, the sp^3 fraction is lower than in the undoped case at the same laser energy density by approximately 40 percent. As titanium fraction increases, the sp^3 fraction appears to decrease. The EELS results from the carbon K-edge show that the $1s \rightarrow \pi^*$ feature remains strong regardless of dopant concentration. If titanium carbide is present, the $1s \rightarrow \pi^*$ feature may be enhanced due to bond

Table 6.3: sp^3 fraction of copper and titanium doped diamond-like carbon as a function of concentration. Concentrations are calculated from EELS and from the experimental conditions.

<i>Ti</i>			<i>Cu</i>		
<i>F (EELS)</i>	<i>F (expt.)</i>	<i>sp³ (pct.)</i>	<i>F (EELS)</i>	<i>F (expt.)</i>	<i>sp³ (pct.)</i>
0.094	2.0	26.31	0.52	3.0	17.65
1.08	4.37	21.99	0.655	6.41	27.53
7.21	10.87	20.73	0.79	15.44	22.35

delocalization. The sp^3 fraction may increase without a corresponding change in the carbon K-edge spectrum due to the effects of bond delocalization. Bond delocalization will occur as the fraction of titanium carbide increases, due to the metallic bonding present in titanium carbide.

Similarly, the sp^3 fraction estimated in the case of the copper doped samples is less than in the undoped samples at the same laser conditions. Metallic bonding may lead to bond delocalization and an apparent enhancement of the $1s \rightarrow \pi^*$ feature. It is typically expected that copper does not form a carbide. However, at the interface of a copper nanoparticle with DLC, this may become possible. Interfaces are inherently non-equilibrium, permitting the formation of a copper-carbon compound. This compound has metallic bonding, as indicated by the bond-delocalization effects. Electron energy loss spectroscopy may not be an accurate means of determining sp^3 fraction in doped diamond-like carbon samples.

6.4.3 Copper and Titanium Ionization Edges

The copper and titanium ionization edges can, in theory, provide estimates of the dopant concentration. Copper has an M ionization edge at 74 eV and $L_{2,3}$ ionization edges at 931 eV and 951 eV. Titanium has $L_{2,3}$ ionization edges at 456 eV and 462 eV. The titanium and copper concentrations are calculated as described in the Experimental chapter. The window of integration for the ionization edges for titanium and copper is 50 eV, while for carbon the integration window is 30 eV. The low concentrations of copper make calculation of the copper fraction difficult. Fourier-log deconvolution proved to add enough noise to make the copper $L_{2,3}$ -edges difficult to discern. In this case, the raw spectrum was used to calculate the fraction of copper. For the titanium doped samples, the Ti L-edge was most noticeable in the specimen with the largest concentration.

All samples were prepared by placing strips of dopant material of equal size on to a rotating carbon target. The laser alternately struck the dopant material and the carbon. Calculation of the dopant fraction via EELS indicates titanium fractions of 0.94, 1.08, and 7.21 percent for depositions using one, two and four strips of titanium. The copper fractions calculated via EELS are 0.52 and 0.79 percent for depositions of one and four strips of copper. No copper peak could be found in the sample prepared using two copper strips. There are several problems with determining the dopant fraction using EELS. First, high resolution TEM

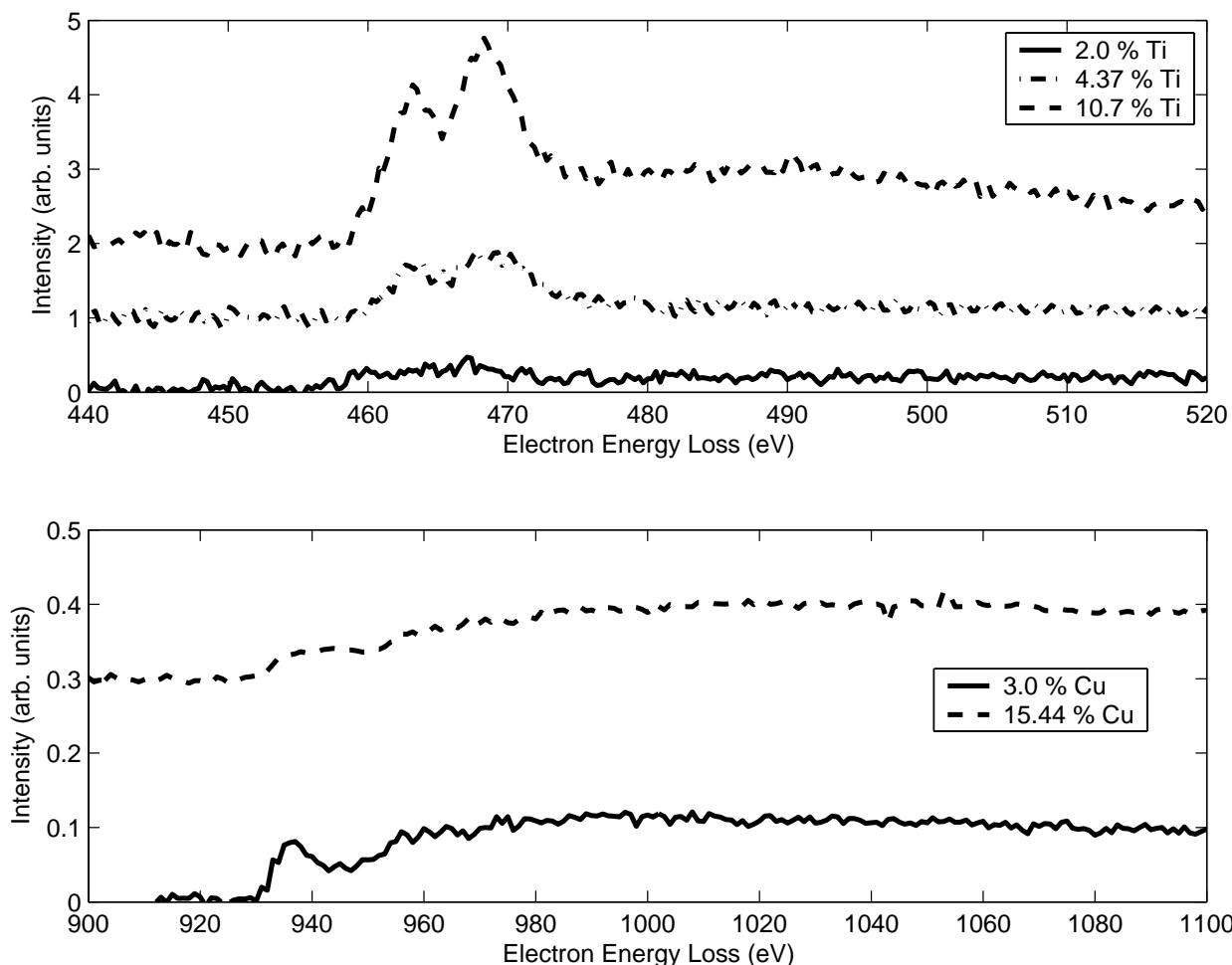


Figure 6.8: L shell ionization region from EELS spectra of copper and titanium doped diamond-like carbon at different titanium concentrations.

reveals that the dopants are present as nanocrystals, rather than evenly mixed throughout the diamond-like carbon matrix. Copper has no solubility in carbon, and thus will not occupy substitutional sites within the amorphous carbon matrix. The location and size of the beam will thus affect the estimated fraction of dopant material. If the film is too thick, then multiple scattering effects will diminish the intensity of the ionization peaks from the dopant materials. For low dopant concentrations, the ionization edges of those dopants may not be visible. All samples prepared in this experiment are plan view specimens. Their thickness, except for a few regions at the edge of the film, is between 1000 Å and 2000 Å. Therefore, it is best to prepare samples for quantitative microanalysis as cross sections, rather than plan view. Other analysis techniques, such as Rutherford backscattering, can also be used to determine the dopant fraction. X-ray photoelectron spectroscopy may be useful, however it will only give the properties of the surface.

An estimate of the dopant concentration can be made by considering the size of dopant strips used in the deposition. The target rotator revolves at six revolution per minute, thus once every ten seconds, the target

makes a complete revolution. The laser pulse frequency was 10Hz , thus there were 100 laser pulses in a complete revolution of the target. It is estimated that the growth rate per pulse for carbon is $2\text{\AA}/\text{pulse}$ and the growth rate for copper and titanium is $1\text{\AA}/\text{pulse}$. The difference in growth rates is due to the difference in surface reflectivity, which is larger for metals than for carbon. The dimensions of the copper and titanium strips are such that if one strip of dopant material is placed on the target, approximately ten out of the one hundred pulses to the target during its revolution will strike the dopant material.

As an example, consider the case of a single titanium dopant strip. The density of titanium is 4.51 g/cm^3 and the density of diamond-like carbon is taken to be 3.1 g/cm^3 . [2] Thus, over a 1 cm^2 area, approximately the dimensions of the silicon substrates, there are $4.51 \times 10^{-8}\text{ g/\AA}$ of titanium and $3.1 \times 10^{-8}\text{ g/\AA}$ of carbon. The molecular weight of carbon is 12 g/mol and the molecular weight of titanium is 47.90 g/mol . Thus, there are $1.55 \times 10^{15}\text{ atoms/\AA}$ of carbon and $5.67 \times 10^{14}\text{ atoms/\AA}$. The total number of titanium atoms deposited in a complete revolution of the target is therefore:

$$N_{Ti} = 10\text{ pulses} \times 0.1 \frac{\text{\AA}}{\text{pulse}} \times 5.67 \times 10^{14} \frac{\text{atoms}}{\text{\AA}} = 5.67 \times 10^{14}\text{ atoms Ti} \quad (6.2)$$

Performing a similar analysis on carbon for a single strip of dopant material yields a total number of carbon atoms of $N_C = 2.79 \times 10^{16}\text{ atoms C}$. Thus, the atomic fraction of dopant material in this case is:

$$f_{Ti} = \frac{N_{Ti}}{N_C + N_{Ti}} = \frac{5.67 \times 10^{14}\text{ atoms Ti}}{5.67 \times 10^{14}\text{ atoms Ti} + 2.79 \times 10^{16}\text{ atoms C}} \approx 2\% \text{ Ti} \quad (6.3)$$

This analysis is performed for the cases of two and four dopant strips for titanium, and for one, two, and four dopant strips of copper. The results are shown in Table 6.3. The density of copper used was 8.93 g/cm^3

Chapter 7

Conclusions

A study of the plasma created in unmagnetized laser ablation plumes was undertaken to determine the properties of the plasma. Mass loss measurements show that the ionization fraction is approximately 5 percent. This indicates that the neutral component of the plume is the dominant factor in determining the sp^3 fraction of diamond-like carbon films. An energy balance indicates that the flow speed of the neutral particles must be less than that of the ionized species. The presence of sheath formation will not greatly accelerate ions. Langmuir probe techniques are determined to not need corrections for collisions within the sheath.

Current models of diamond-like carbon film formation were investigated and found to be lacking in a full description of the physics involved. The currently accepted model, subplantation, posits that stress leads to formation of sp^3 bonding. However, it is the formation of sp^3 bonding that leads to the increase in local compressive stress. The growth of diamond-like carbon films is mediated by electronic excitation of the incident carbon atoms. Electron excitation occurs either through collisions with electrons or photons, or through recombination of ions at the surface. Incident carbon atoms will only travel a few angstroms. When they slow to bond, their electronic excitation energy may drive transitions between sp^2 and sp^3 coordination. If the electronic excitation energy is sufficiently elevated, then multiple carbon atoms may experience this transition. As particle kinetic energy is increased beyond a critical energy, displacement of atoms leads to the transformation of sp^3 sites to sp^2 sites. Also, as particle kinetic energy increases, the range increases and thus the number of collisions increases. This acts to reduce the electronic excitation energy of the incident atom, and therefore reduces its likelihood to form an sp^3 coordinated carbon atom.

An investigation in the the effect of an external magnetic field on laser ablation plasma plumes was conducted. A magnetic field with a peak magnitude of 0.4 T was created with two NdFeB magnets perpendicular to the flow direction. Corrections to the quadruple Langmuir probe equations, specifically electron temperature and floating potential, were derived from collisionless electron collection theory in the presence of a magnetic field. This is valid for the plasmas encountered in the experiment, as the electron-ion collision and electron-neutral collision frequencies were much less than the electron cyclotron frequency. The effect of

the correction is a reduction in the electron temperature calculated using the field-free equations. Ion signal corrections are unnecessary as the ion cyclotron radius is much greater than the probe diameter.

Plume flow speeds were estimated from electron temperature data. Flow speed was uniformly reduced from the field-free case. The effect of probe offset was important at the 1 *cm* Langmuir probe position. Displacement of the magnetic field was determined using \dot{B} probes. Only a small displacement in the external magnetic field was noted. The weak displacement of the magnetic field by the plasma is due to the small kinetic β of these plasmas. The field energy density is much greater than the flow energy density. Field line displacement increased with increasing laser energy density, as a result of the increased flow speed of the plasma. The effect of probe offset at 1 *cm* was seen in the magnetic field data, confirming the results from the flow speed data.

Electron temperatures were increased by a factor of 3 to 4 over field-free values. Increases in electron temperature due to field line diffusion are impossible given the small magnetic deflection. Compression of the electron fluid does not present sufficient energy for plume heating either. However, slowing of the ionic component, as found in the flow speed data, presents a source of energy for plume heating. However, it is necessary to have a collision frequency larger in magnitude than the Spitzer resistivity in order to have the electron-ion temperature equilibration time of the correct time scale.

Ion dynamics showed behavior not seen in the field-free case. A large oscillation near the ion-cyclotron frequency was present in signals from Langmuir probe positions of 2 *cm*, 3 *cm*, and 4 *cm*. Alfvén waves were eliminated as a possibility due to their lack of presence in the \dot{B} probe signals and the fact that Alfvén waves are low-frequency waves. Ion drift waves are eliminated as they are not unstable, and thus cannot grow to the large magnitudes found in this experiment. It is concluded that the observed phenomenon is an ion-cyclotron wave propagating perpendicular to the flow and to the magnetic field. The instability satisfies a transverse electrostatic ion cyclotron instability, although growth rates were not calculated. The Rayleigh-Taylor instability is eliminated as a possible instability mechanism due to unfavorable field geometries and insufficiently rapid growth times.

Growth of a diamond-like carbon film illustrates the importance of neutral particles in DLC deposition. The ionic component was slowed due to interactions with the magnetic field. However, the neutral component is unaffected, and the sp^3 fraction of the film was larger than expected from ion kinetic energy alone.

A series of diamond-like carbon films were deposited with titanium, copper, and silver to investigate the changes in film structure and properties with dopant concentration. The measurement of stress reduction by visible Raman spectroscopy was found to be poor. Titanium and copper were found to reduce the hardness of diamond-like carbon. Electron energy loss spectroscopy performed on the doped specimens showed that the sp^3 fraction in doped samples was less than that in undoped samples at the same laser conditions. Bond delocalization effects are assumed to enhance the $1s \rightarrow \pi^*$ feature of the carbon K-edge. Estimation of the dopant concentration and sp^3 fraction in segregated, nanocrystalline form via EELS is likely inaccurate due to the small sample size of the TEM beam. Doping of diamond-like carbon with different elements is found

to create nanoparticles with the DLC matrix. Copper, titanium, and silver nanoparticles were formed using pulsed laser deposition. Z-contrast images on silver doped diamond-like carbon show the formation of self assembled nanoparticles. Their growth is consistent with a stress induced diffusion process.

Chapter 8

Future Work

8.1 Undoped Diamond-like Carbon Films

To verify the predictions made in the chapter describing the formation of diamond-like carbon films, I propose several experiments. First, the current set of experiments involving the variation of sp^3 fraction with laser energy density should be extended to higher energy densities, and thus, larger kinetic energies. Unfortunately, the laser used was not capable of creating ions up to several keV . Second, the formation of diamond-like carbon films by neutral carbon atom beams should be investigated. If possible, beams of ground state, and then excited, neutral carbon atoms of different kinetic energies should be used to deposit carbon films. This would prove a definitive test of my postulate that sp^3 bonding is a result of electronic excitation, and that variations in sp^3 fraction with kinetic energy are a result of the changes in energy coupling as kinetic energy is changed.

8.2 Doped Diamond-like Carbon Films

Further research can be performed on the structure and properties of doped diamondlike carbon films. An in-depth study of the structure would involve the analysis of the segregation of dopants within the diamond-like carbon film. Earlier in the dissertation, it was shown that both carbide and non-carbide forming dopants will form nanocrystals within diamond-like carbon. Cross section HRTEM, Z-contrast imaging, and diffraction are needed to understand how these nanoparticles grow and assemble themselves. Point-by-point electron energy loss spectroscopy will determine the sp^3 fraction in regions only populated by diamond-like carbon. This analysis will also yield information on how the dopants segregate themselves. It may be possible to engineer the size and location of the nanoparticles by changing the stresses within the film. This can be accomplished by using different sp^3 fractions, as this is related to stress in as-deposited diamond-like carbon films.

An analysis of the properties of doped diamond-like carbon films will be complementary to the research

on the structure of doped diamond-like carbon films. Studies of optical, electronic, and magnetic properties will determine how electrons behave within diamond-like carbon. Doped, high sp^3 fraction diamond-like carbon films may yield semi-transparent conductors. Magnetic materials may be created with appropriate dopants. The mechanical properties of DLC films doped with different elements can be studied for their usefulness in medical applications where high wear resistant, inert coatings are necessary.

8.3 Optical Spectroscopy

A detailed series of experiments could be undertaken to confirm the Langmuir probe results discussed in this paper. Optical spectroscopy could be performed in both the unmangetized and magnetized plumes. A gated optical multichannel analyzer would yield temporally dependent information on the neutrals and ions within the plume. An important avenue of investigation would be the applicablity of certian equilibrium models to the laser ablation plasma. It is not currently clear whether or not the assumption of local thermodynamic equilibrium or coronal equilibrium are valid for the purposes of estimating an electron temperature. Spatially resolved data may be acheived by using an appropriately collimnated fiber. This can be used to estimate flow speeds for certian species. More advanced optical spectroscopy technques would include the used of gated, intensified CCDs to make images of the plasma. This could be coupled with laser induced fluoroscopy to create a map of species within the plume.

8.4 Self Assembly of Nanostructured Magnetic Materials

The presence of a magnetic field may lead to the creation of novel nanostructures. The diffusion along the surface of the film during deposition is affected by the surface forces. Addition of an intense magnetic field will create a dipole force on individual atoms which may affect their surface migration. It may also be possible to create nanostructures for magnetic materials with domains of each of the nanoparticles aligned.

8.5 Different Magnetic Field Studies

The use of different field geometries may permit different plume behavior to occur. The development of different instabilities and turbulence in different field geometries and their effect on transport could be studied in detail. The effects of gradients in the magnetic field and field curvature were not discussed in this dissertation. The effect of field gradient and curvature drifts on electrons and ions may become significant in certian geometries. It would also be interesting to investigate whether or not waves at the ion cyclotron frequency are seen from the laser ablation of different materials and of multicomponent targets. A full three-dimensional, time-dependant model of plume expansion could be performed computationally. This would require significant computational effort.

Bibliography

- [1] Y. Lifshitz. *Diamond and Related Materials*, 8:1659–1676, 1999.
- [2] A.C. Ferrari and J. Robertson. *Physical Review B*, 61:14095, 2000.
- [3] M. Chhowalla, A.C. Ferrari, J. Robertson, and G.A.J. Amaratunga. *Applied Physics Letters*, 76:1419, 2000.
- [4] Q. Wei and J. Narayan. *International Materials Reviews*, 45:133, 2000.
- [5] A.A. Voevodin, S.J.P. Laube, S.D. Walck, J.S. Solomon, M.S. Donley, and J.S. Zabinkski. *Journal of Applied Physics*, 78:4123, 1995.
- [6] Q. Wei, A.K. Sharma, J. Sankar, and J. Narayan. *Composites Part B*, 30:675, 1999.
- [7] Q. Wei, R.J. Narayan, J. Narayan, J. Sankar, and A.K. Sharma. *Materials Science and Engineering B*, 53:262, 1998.
- [8] Q. Wei, J. Sankar, A.K. Sharma, S. Oktyabrsky, J. Narayan, and R.J. Narayan. *Journal of Materials Research*, 15:633, 2000.
- [9] J. Robertson. *Semiconductor Science and Technology*, 18:S12–S19, 2003.
- [10] J. Robertson. *Thin Solid Films*, 296:61–65, 1997.
- [11] J. Robertson and E.P. O’Reilly. *Physical Review B*, 35:2946, 1987.
- [12] R.J. Narayan, Q. Wei, A.K. Sharma, J.J. Cuomo, and J. Narayan. *Mater. Res. Soc. Proc.*, 526:355–360, 1998.
- [13] K. Lmimouni, C. Legrand, C. Dufour, and A. Chapoton. *Applied Physics Letters*, 78:2437, 2001.
- [14] M. Schlatter. *Diamond and Related Materials*, 11:1781, 2002.
- [15] M. Bonelli, A.C. Ferrari, A. Fioravanti, A. Li Bassi, A. Miotello, and P.M. Ossi. *The European Physical Journal B*, 25:269, 2001.

- [16] A.C. Ferrari, B. Kleinsorge, N.A. Morrison, A. Hart, V. Stolojan, and J. Robertson. *Journal of Applied Physics*, 85:7191, 1999.
- [17] S. Waidmann, M. Knupfer, J. Fink, B. Kleinsorge, and J. Robertson. *Journal of Applied Physics*, 89:3783, 2001.
- [18] N.A. Marks, D.R. McKenzie, P.A. Pailthorpe, M. Bernasconi, and M. Parrinello. *Physical Review B*, 54:9703, 1996.
- [19] D.G. McCulloch, E.G. Gerstner, D.R. McKenzie, S. Prawer, and R. Kalish. *Physical Review B*, 52:850, 1995.
- [20] K.W.R Gilkes, S. Prawer, K.W. Nugent, J. Robertson, H.S. Sands, Y. Lifshitz, and X. Shi. *Journal of Applied Physics*, 87:7283, 2000.
- [21] S. Aisenberg and R. Chabot. *Journal of Applied Physics*, 42:2953, 1971.
- [22] Y. Lifshitz, T.h. Kohler, Th. Frauenheim, I. Guzmán, A. Hoffman, R.Q. Zhang, X.T. Zhou, and S.T. Lee. *Science*, 297:1531, 2002.
- [23] Y. Umehara, S. Murai, Y. Koide, and M. Murakami. *Diamond and Related Materials*, 11:1429, 2002.
- [24] J. Haverkamp, R.M. Mayo, M.A. Bourham, J. Narayan, G. Duscher, and C. Jin. *Journal of Applied Physics*, 93:3627, 2003.
- [25] Ya. B. Zel'dovich and Yu. P. Razier. *Physics of Shock Waves and High Temperature Hydrodynamic Phenomena*. Dover, New York, 2002.
- [26] R.K. Singh and J. Narayan. *Physical Review B*, 41:8843, 1990.
- [27] K.L. Saenger. *Journal of Applied Physics*, 70:5629, 1991.
- [28] J.N. Leboeuf, K.R. Chen, J.M. Donato, D.B. Geohegan, C.L. Liu, A.A. Puretzky, and R.F. Wood. *Physics of Plasmas*, 3:2203, 1995.
- [29] J.N. Leboeuf, K.R. Chen, J.M. Donato, D.B. Geohegan, C.L. Liu, A.A. Puretzky, and R.F. Wood. *Applied Surface Science*, 96-98:14, 1996.
- [30] F. Garrelie, J. Aubreton, and A. Catherinot. *Journal of Applied Physics*, 83:5075, 1998.
- [31] T.E. Itina, J. Hermann, P. Delaporte, and M. Sentis. *Physical Review E*, 66:066406-1, 2002.
- [32] R.M. Mayo, J.W. Newman, A. Sharma, Y. Yamagata, and J. Narayan. *Journal of Applied Physics*, 86:2865, 1999.
- [33] V.F. Kovalev and V. Yu. Bychenkov. *Physical Review Letters*, 90:185004, 2003.

- [34] T. Nedelea and H.M. Urbassek. *Physics of Plasmas*, 9:3209, 2002.
- [35] P. Mora. *Physical Review Letters*, 90:185002, 2003.
- [36] D.S. Dorozhkina and V.E. Semenov. *Physical Review Letters*, 81:2691, 1998.
- [37] R. Diamant, E. Jimenez, E Haro-Poniatowski, L. Ponce, M. Fernandez-Guasti, and J.C. Alonso. *Diamond and Related Materials*, 8:1277–1284, 1999.
- [38] A. Thum-Jaeger, B.K. Sinha, and K.R. Rohr. *Physical Review E*, 63:016405–1, 2000.
- [39] H. Qingrun and J. Gao. *Journal of Physics: Condensed Matter*, 9:10333, 1997.
- [40] A. Neogi and R.K. Thareja. *Journal of Applied Physics*, 85:1131, 1999.
- [41] L. Dirnberger, P.E. Dyer, S.R. Farrar, and P. H. Key. *Applied Physics A*, 59:311–316, 1994.
- [42] T.A. Peyser, C.K. Manka, B.H. Ripin, and G. Ganguli. *Physics of Fluids B*, 4:2448, 1992.
- [43] B.H. Ripin, E.A. McLean, C.K. Manka, C. Pawley, J.A. Stamper, T.A. Peyser, A.N. Mostovych, J. Grun, A.B. Hassam, and J. Huba. *Physical Review Letters*, 1987:2299, 1987.
- [44] G. Dimonte and L.G. Wiley. *Physical Review Letters*, 67:1991, 1991.
- [45] A.N. Mostovych, B.H. Ripin, and J.A. Stamper. *Physical Review Letters*, 62:2837, 1989.
- [46] D.W. Koopman. *Physics of Fluids*, 19:670, 1976.
- [47] R.J. Goldston and P.H. Rutherford. *Introduction to Plasma Physics*. Institute of Physics, London, 1997.
- [48] A. Neogi and R.K. Thareja. *Applied Physics B*, 72:231, 2001.
- [49] S.S. Harilal, M.S. Tillack, B. O’Shay, C.V. Bindhu, and F. Najmabadi. *Physical Review E*, 69:026413, 2004.
- [50] A. Neogi and R.K. Thareja. *Physics of Plasmas*, 6:365, 1999.
- [51] A. Neogi, V. Narayanan, and R.K. Thareja. *Physics Letters A*, 258:135, 1999.
- [52] J. Diaz, S. Ferrer, and F. Comin. *Journal of Applied Physics*, 84:572, 1998.
- [53] H. Minami, D. Manage, Y.Y. Tsui, R. Fedosejevs, M. Malac, and R. Egerton. *Applied Physics A*, 73:531–534, 2001.
- [54] R.F. Egerton. *Electron Energy Loss Spectroscopy in the Electron Microscope*. Plenum Press, New York, 1st edition, 1986.

- [55] J. Narayan and J. Fletcher. *Mater. Res. Soc. Symp. Proc.*, 2:191, 1981.
- [56] A.C. Ferrari, A. Libassi, B.K. Tanner, V. Stolojan, J. Yuan, L.M. Brown, S.E. Rodil, B. Kleinsorge, and J. Robertson. *Physical Review B*, 62:11089, 2000.
- [57] J. Kulik, Y. Lifshitz, G.D. Lempert, J.W. Rabalais, and D. Marton. *Journal of Applied Physics*, 76:5063, 1994.
- [58] S.D. Berger, D.R. McKenzie, and P.J. Martin. *Philosophical Magazine Letters*, 57:285, 1988.
- [59] Jr. E. Bright Wilson, J.C. Decius, and Paul C. Cross. *Molecular Vibrations: The Theory of Infrared and Raman Vibrational Spectra*.
- [60] G. Glockler. *Reviews of Modern Physics*, 15:1943, 1943.
- [61] J.D. Hunn, S.P. Withrow, C.W. White, and R.M. Hembree Jr. *Physical Review B*, 52:8106, 1995.
- [62] S. Praver, K. Nugent, Y. Lifshitz, G.D. Lempert, E. Grossman, J. Kulik, I. Avigal, and R. Kalish. *Diamond and Related Materials*, 5:433, 1996.
- [63] K.W.R. Gilkes, H.S. Sands, D.N. Batchelder, J. Robertson, and W.I. Milne. *Applied Physics Letters*, 70:1980, 1997.
- [64] S. Bhargava, H.D. Bist, A.V. Narlikar, S.B. Samanta, J. Narayan, and H.B. Tripathi. *Journal of Applied Physics*, 79:1917, 1996.
- [65] S.B. Segall and D.W. Koopman. *Physics of Fluids*, 16:1149, 1973.
- [66] I.H. Hutchinson. *Principles of Plasma Diagnostics*. Cambridge University Press, New York, 1987.
- [67] R.M. Mayo, J.W. Newman, A. Sharma, Y. Yamagata, and J. Narayan. *Journal of Applied Physics*, 88:6868, 2000.
- [68] F.F. Chen. Electric probes. In R.A. Huddleston and S.L. Leonard, editors, *Pure and Applied Physics: Plasma Diagnostic Techniques*, volume 21, page 113. Academic Press, 1965.
- [69] J.G. Laframboise and J. Rubenstein. *The Physics of Fluids*, 19:1900, 1976.
- [70] J. Rubenstein and J.G. Laframboise. *Physics of Fluids*, 21:1655, 1978.
- [71] W. Botticher. Measurement of magnetic fields in plasma. In W. Botticher, editor, *Plasma Diagnostics*, volume 1, page 617. North Holland, 68.
- [72] E.G. Gamaly, A.V. Rode, B. Luther-Davies, and V.T. Tikhonchuk. *Physics of Plasmas*, 9:949, 2002.
- [73] M.M. Murnane, H.C. Kapteyn, and R.W. Falcone. *Physical Review Letters*, 62:155, 1989.

- [74] Y. Yamagata, A. Sharma, J. Narayan, R.M. Mayo, J.W Newman, and K. Ebihara. *Journal of Applied Physics*, 88:6861, 2000.
- [75] F. Claeysens, M.N.R Ashfold, E. Sofoulakis, C.G. Ristoscu, D. Anglos, and C. Fotakis. *Journal of Applied Physics*, 91:6162, 2002.
- [76] J. Haverkamp, R.M. Mayo, J. Narayan, and C. Jin. *Mat. Res. Soc. Symp. Proc.*, 697:165–169, 2001.
- [77] S.S Harilal, C.V. Bindhu, R.C. Issac, V.P.N. Nampoori, and C.P.G. Vallabhan. *Journal of Applied Physics*, 82:2140, 1997.
- [78] Jason Haverkamp. Master’s Thesis. Analysis of Carbon Plasma Plumes for High sp^3 Content DLC Films Created by Pulsed Laser Deposition., 2001.
- [79] F.F. Chen. *Introduction to Plasma Physics and Controlled Fusion, 2nd Ed.* Plenum Press, New York, 1984.
- [80] R.M. Mayo, J.C. Fernandez, I. Henins, L.S. Kirschenbaum, C.P. Munson, and F.J. Wysocki. *Nuclear Fusion*, 31:2087, 1991.
- [81] Michael Nastasi, James W. Mayer, and James K. Hirvonen. *Ion-solid Interactions Fundamentals and Applications.* Cambridge, New York, 1996.
- [82] Y. Lifshitz, S.R. Kasi, and J.W. Rabalais. *Physical Review Letters*, 62:1290, 1989.
- [83] J.J. Cuomo, D.L. Pappas, J. Bruley, J.P Doyle, and K.L Saenger. *Journal of Applied Physics*, 70:1706, 1991.
- [84] N.A. Marks, N.C. Cooper, D.R. McKenzie, D.G. McCulloch, P. Bath, and S.P. Russo. *Physical Review B*, 85:075411, 2002.
- [85] John Robertson. *Diamond and Related Materials*, 3:361–368, 1994.
- [86] N.C. Cooper, M.S. Fagan, C.M. Goringe, N.A. Marks, and D.R. McKenzie. *Journal of Physics: Condensed Matter*, 14:723–730, 2002.
- [87] N.A. Marks, D.R. McKenzie, P.A. Pailthorpe, M. Bernasconi, and M. Parrinello. *Physical Review Letters*, 76:768, 1996.
- [88] D.G. McCulloch, D.R. McKenzie, and C.M. Goringe. *Physical Review B*, 61:2349, 2000.
- [89] TH. Kohler, Th. Frauenheim, and G. Jungnickel. *Physical Review B*, 52:11387, 1995.
- [90] M.P. Siegal, J.C. Barbour, P.N. Provencio, D.R. Tallant, and T.A. Friendmann. *Applied Physics Letters*, 73:759, 1998.

- [91] N.A. Marks. *Physical Review B*, 56:768, 1997.
- [92] G. Duscher. *Personal Communication*, 2004.
- [93] John Robertson. *Diamond and Related Materials*, 2:984–989, 1993.
- [94] M. Karplus and R.N. Porter. *Atoms and Molecules: An Introduction for Students of Physical Chemistry*. W.A. Benjamin, Inc., New York, 1970.
- [95] R. Chang. *Chemistry, 5th Ed.* McGraw Hill, New York, 1994.
- [96] R.K. Singh, O.W. Holland, and J. Narayan. *Journal of Applied Physics*, 68:233, 1990.
- [97] Homer D. Hagstrum. Low energy de-excitation and neutralization processes near surfaces. In N.H. Tolk, J.C. Tully, W. Heiland, and C.W. White, editors, *Inelastic ion-surface collisions*, volume 1, page 1. Academic Press, 1977.
- [98] J. Narayan, D. Fathy, O.S. Oen, and O.W. Holland. *Journal of Vacuum Science and Technology A.*, 2:1303, 1984.
- [99] T. Ikegami, S. Ishibashi, Y. Yamagata, K. Ebihara, R.K. Thareja, and J. Narayan. *J. Vac. Sci. Tech. A*, 19:1304, 2001.
- [100] Abhilasha, P.S.R. Prasad, and R.K. Thareja. *Physical Review E*, 48:2929, 1993.
- [101] R.M. Mayo, M.A. Bourham, M.E. Glover, R.W. Caress, J.R.D. Earnhart, and D.C. Black. *Plasma Sources Science and Technology*, 4:47–55, 1995.
- [102] K.J. Koivusaari, J. Levoska, and S. Leppavuori. *Journal of Applied Physics*, 85:2915, 1999.
- [103] B.B. Kadomstev. *Plasma Turbulence*. Academic Press, New York, 1965.
- [104] I.B. Bernstein. *Physical Review*, 109:10, 1958.
- [105] L.S. Hall, W. Heckrotte, and T. Kammash. *Physical Review*, 139:A117, 1965.
- [106] E.G. Harris. *Physical Review Letters*, 2:A117, 1959.
- [107] R.A. Dory, G.E. Guest, and E.G. Harris. *Physical Review Letters*, 14:131, 1965.
- [108] A.V. Timofeev and V.I. Pistunovich. Cyclotron instabilities in anisotropic plasmas. In M. A. Leontovich, editor, *Reviews of Plasma Physics*, volume 5, page 401. Consultants Bureau, 1970.
- [109] David B. Williams and C. Barry Carter. *Transmission Electron Microscopy*. Plenum Press, New York, 1996.

- [110] A. Gerhards, C. Ronning, H. Hofsass, M. Seibt, and H. Gibhardt. *Journal of Applied Physics*, 93:1203, 2003.
- [111] V.A. Shchukin and D. Bimberg. *Reviews of Modern Physics*, 71:1125, 1999.
- [112] J. Narayan and B.C. Larson. *Journal of Applied Physics*, 93:278, 2003.
- [113] T.A. Friedmann, J.P. Sullivan, J.A. Knapp, D.R. Tallant, D.M. Follstaedt, D.L. Medlin, and P.B. Mirkarimi. *Applied Physics Letters*, 71:3820, 1997.